INTEGRATED ELECTRONIC-PHOTONIC SYSTEMS: FROM HIGH-RESOLUTION SYNTHESIS TO COMPACT PHASED ARRAYS

Farshid Ashtiani

A DISSERTATION

in

Electrical and Systems Engineering

Presented to the Faculties of the University of Pennsylvania

in

Partial Fulfillment of the Requirements for the

Degree of Doctor of Philosophy

2020

Supervisor of Dissertation

____

Firooz Aflatouni, Skirkanich Assistant Professor of Electrical and Systems Engineering

Graduate Group Chairperson

____

Victor Preciado, Associate Professor of Electrical and Systems Engineering

Dissertation Committee

Jan Van der Spiegel (Chair), Professor of Electrical and Systems Engineering
Nader Engheta, H. Nedwill Ramsey Professor of Electrical and Systems Engineering
Troy Olsson, Assistant Professor of Electrical and Systems Engineering
Bo Zhen, Assistant Professor of Physics and Astronomy

INTEGRATED ELECTRONIC-PHOTONIC SYSTEMS: FROM HIGH-RESOLUTION TO COMPACT PHASED ARRAYS

To my parents.

Acknowledgements

First and foremost, I would like to thank my advisor, Prof. Firooz Aflatouni for his excellent support and guidance during my PhD. This thesis would not have been possible without his patience, dedication, and supervision. I learnt a lot from him during the past few years of my PhD.

I also would like to thank my thesis committee members Prof. Jan Van der Spiegel, Prof. Nader Engheta, Prof. Troy Olsson, and Prof. Bo Zhen. I really appreciate their valuable guidance, insight, and support.

A great amount of my time was spent with the wonderful members of the Electronic-Photonic Microsystems Laboratory whom I would like to thank very much for their help, support, and cooperation. I thank current and former members of our group, Mohamad Hossein Idjadi, Pouria Sanjari, Dr. Zhe Xuan, Dr. Shermin Arab, Han Hao, Kaisarbek Omirzakhov, Vasant Iyer, Ali Pirmoradi, Beril Tayfun, Alexander Geers, Michael Rosa, Aaron Lee, Andrew Botelho, and Adam Engelson. Also, I would like to thank Angelina Risi, Nishant George, and Sethupriya Menon for their help with the nanophotonic imager project.

I would like to thank Maryam Daniali very much for her support, friendship, and encouragements.

Finally, I would like to express my gratitude to my parents, Tahereh and Mohammad Reza, and my brother, Faraz, for their unconditional love and support and for providing me with numerous opportunities to go after my dreams. These words would not have existed without them.

ABSTRACT

INTEGRATED ELECTRONIC-PHOTONIC SYSTEMS: FROM HIGH-RESOLUTION SYNTHESIS TO COMPACT PHASED ARRAYS

Farshid Ashtiani

Firooz Aflatouni

Silicon-based integrated electronics drastically changed many areas from communications to healthcare, mainly due to the high yield and low cost of large-scale production of complex systems with very small footprints. More recently, silicon photonics has also been used to integrate bulky, expensive, and power hungry optical systems. Low propagation loss and high optical confinement of silicon photonic waveguides have enabled many applications from imaging to signal generation. Since both electronic and photonic components can now be co/hybrid integrated, there are a large number of application that are enabled by using integrated electronic-photonic systems. Electronic-assisted photonic systems, benefit from complex control electronics to implement photonic systems with superior performance compared to conventional implementations. Similarly, photonic-assisted electronic systems take advantage from the large bandwidth available at optical frequencies as well as low-loss optical interconnects to enhance the speed and power consumption of electronic systems. In this thesis, three examples of integrated electronic-photonic systems are presented. Starting with synthesis of optical signals, a partially integrated high-resolution optical frequency synthesizer is demonstrated where an integrated electro-optical phase-locked loop is used to phase-

frequency lock a highly tunable laser to a stabilized optical frequency comb. The system is capable of synthesizing optical frequencies around 1550 nm over a range of 5 THz with sub-Hz resolution. Next, we benefit from the large bandwidth and low loss of photonic integrated components to implement a nanophotonic near-field microwave imager. The imager up-converts the received microwave signals reflected from a metallic object to optical frequencies and optically processes the signals to form the corresponding image of the object. The 121-pixel imager achieves 4.8° spatial resolution with orders of magnitude smaller size than the benchtop implementations and a fraction of the power consumption. Finally, solid-state optical beam steering using novel integrated optical phased arrays is presented. We address the challenge of realizing optical phased arrays with very small element spacing by reducing the number of phase shifters required for 2-D beam steering as well as benefiting from a photonic fabrication process with two optical device layers to implement very compact optical elements. Using these novel methods, an optical phased array with 3 μm element spacing and beam steering range of about 23° is implemented.

Table of Contents

Dedication iii

Acknowledgements iv

Abstract vi

List of Tables x

List of Figures xi

List of Acronyms xvii

Chapter 1: Introduction 1
1.1 Optical signal synthesis: a partially integrated approach……….. 2
1.2 Optical signal processing……………………………………... 5
1.3 Optical beam steering…………………………………………… 8
1.4 Thesis outline…………………………………………………… 11

Chapter 2 – Synthesis of optical signals: Towards integrated optical frequency synthesizers 15
2.1 Principle of operation and system architecture…………………. 21
2.1.1 Principle of operation…………………………………. 21
2.1.2 System architecture…………………………………… 23
2.2 Tunable laser characterization………………………………... 25
2.3 Coarse tuning and tooth indexing…………………………….. 30
2.4 Fine tuning using the EOPLL chip and the AAS……………….. 34
2.4.1 EOPLL nonlinear theory if operation…………………. 36
2.4.2 Theory of heterodyne EOPLL………………………… 41
2.4.3 Integrated EOPLL system architecture and characterization…………………………………………….. 44
2.4.4 Aided acquisition system……………………………… 55
2.5 OFS design challenges………………………………………... 57
2.5.1 False locking………………………………………... 57
2.5.2 TL temperature stabilization response………………… 60

2.6 Optical frequency synthesis………………………………………... 62
2.7 Summary and future work………………………………………. 69

Chapter 3 – Optical signal processing: A nanophotonic near-field imager 73
3.1 Optically delayed electrical pulse……………………………….. 78
3.1.1 Comparison of electrical and optical delay lines……… 82
3.2 System architecture……………………………………………… 84
3.2.1 Coherence effect on image SNR……………………… 88
3.3 Nanophotonic chip characterization…………………………….. 92
3.3.1 Optical power distribution using the 1-D array and the optical path loss of the system………………………………... 93
3.3.2 Total optical path loss…………………………………. 94
3.3.3 Data read-out and calibration…………………………. 95
3.3.4 Wired Characterization………………………………... 98
3.3.5 Wireless characterization……………………………… 100
3.4 Imaging demonstration………………………………………….. 102
3.5 Imager noise performance and linearity………………………… 104
3.5.1 Noise figure of the system…………………………….. 104
3.5.2 Dynamic range and sensitivity………………………... 106
3.6 Summary and Future works……………………………………... 107

Chapter 4 – Optical beam steering: Towards half-wavelength element spacing optical phased arrays 111
4.1 Reducing the number of phase shifters…………………………. 118
4.1.1 Theory of operation…………………………………… 118
4.1.2 System architecture……………………………………. 123
4.1.3 Photonic devices………………………………………. 125
4.1.4 The effect of layout mismatches……………………… 129
4.1.5 Characterization and 2-D beam steering results………. 132
4.2 OPA with compact elements……………………………………. 137
4.2.1 System architecture……………………………………. 140
4.2.2 Photonic devices………………………………………. 142
4.2.3 Characterization and 2-D beam steering results (main lobe power, total loss)………………………………………… 146
4.3 Summary and future works……………………………………… 149

Chapter 5 – Conclusion 152
5.1 Summary………………………………………………………… 152
5.2 Future research directions……………………………………….. 155

References 160

List of Tables

2.1 Comparison if the implemented EOPLL with some of the recent works……………………………………………………………….. 67

2.2 Implemented OFS performance summary……………………………. 69

3.1 Implemented nanophotonic near-field imager performance summary.. 108

4.1 8x8 OPA (IME) performance summary………………………………. 136

4.2 8x8 OPA (TowerJazz) performance summary………………………... 148

List of Figures

1.1	Comparison of a typical EFS and an OFS……………………………....	3
1.2	The schematic of a multi-beam imager by sharing the delay elements between the pixels……………………………………………………....	5
1.3	(a) Conceptual block diagram of 1 1-D 8-element phase array. (b) A Compact 4x4 optical phased array for 2-D beam steering using 8 phase shifters and two layers of photonic routing to achieve close to half-wavelength element spacing……………………………………………..	7
2.1	Block diagram of a typical EFS………………………………………....	16
2.2	(a) Replacing the VCO in and EFS with a semiconductor laser to synthesize optical frequencies. (b) The model of a semiconductor laser acting as a CCO. (c) The block diagram of an OFS after eliminating the frequency divider and using an optical reference. (d) Implementation of the phase detector using an optical power combiner following by a PD. (e) Enhancing the tuning range by having multiple references. (f) Using frequency comb as the reference to simultaneously enhance the tuning range and stability……………...	19
2.3	Frequency synthesis using a coarse tuning and a fine tuning phase. (a) The initial frequency of the TL and the target frequency that is 5.7 GHz higher. (b) Coarse tuning after counting for 11 teeth. (c) Fine tuning using a heterodyne EOPLL for 200 MHz. (d) The block diagram of the heterodyne EOPLL…………………………………………………....	22
2.4	(a) Block diagram of the partially integrated OFS. (b) The EOPLL phase locks the TL to tooth right after the target comb tooth. (c) The reference to the EOPLL is the tooth right before the target comb tooth...	25
2.5	(a) Block diagram of the laser driver. (b) Coarse characterization of the widely tunable laser showing the tuning range and super-modes. (c) TL FM response measurement setup and (d) the corresponding magnitude and phase responses with estimated phase cross-over frequency of 4.2	

MHz………………………………………………………………… 27

2.6 (a) Typical spectrum of an OFC where the non-flat noise floor causes teeth power variation. (b) The setup to generate electro-optical OFC and the resulting spectrum…………………………………………….......... 31

2.7 Operation of the indexing system. (a) No signal is detected when the beat-note is outside the passband of the filters. (b) Bottom path detect the beat-note and a large signal appears at L_3. (c) Top path detects the beat-note but no signal appears at L_3. (d) The OFC spectrum and the detected pulses with two pulses per comb tooth………………………… 32

2.8 The EOPLL principle of operation. (a) The semiconductor laser modelled as a current controlled oscillator, (b) an optical phase detector, and (c) the conceptual block diagram of an EOPLL in presence of loop delay……………………………………………………………….. 37

2.9 (a) Conceptual block diagram of a heterodyne electro-optical phase-locked loop. (b) Phase adjustment mechanism in EOPLL……………… 42

2.10 (a) Schematic of the EOPLL chip. (b) The EOPLL chip microphotograph. (c) Characterization results of the implemented on-chip photonic devices. Peak GC efficieny happens at 1560 nm and coupling angle of 17°. The Y-junction has an excess loss of 0.5 dB…… 45

2.11 The block diagram of the EOPLL and frequency acquisition principle of operation. (a) Block diagram of the EOPLL chip. (b) Frequency detection principle of operation in the complex frequency plane is shown. Each diagram shows the frequency spectrum of the corresponding node in Fig. 2.11(a). "I" and "Q" represent cosine and sine functions, respectively……………………………………………… 46

2.12 Electronic circuitry used for different blocks of the EOPLL chip………. 51

2.13 Measured (a) amplitude and (b) phase mismatch at the output of quadrature mixers (nodes (5) and (6) in Fig. 2.11(a)). (c) The measured characteristics of the frequency detection path when the frequency of the heterodyning signal is set to 900 MHz……………………………… 52

2.14 (a) Measurement setup for characterization of the EOPLL chip. (b) Beat-note lock spectrum for different LO frequencies………………….. 53

2.15 (a) Block diagram of the aided acquisition system. (b) Block diagram of the implemented 90° hybrid in AAS system. (c) Lock detector response measured for LO frequency of 375 MHz……………………………... 55

2.16 (a) Block diagram of a heterodyne EOPLL in the phase domain. (b) Conceptual block diagram of a tunable laser as a current-controlled oscillator…………………………………………………………………. 58

2.17 Measured phase section current versus time when a large mirror current change happens showing how AAS counteracts the laser thermal fluctuations………………………………………………………… 62

2.18 (a) Measurement setup used for optical frequency synthesis demonstration and (b) the setup picture and the EOPLL chip microphotograph. (c) Optical frequency spectrum showing the initial location of the TL with respect to the reference comb and (d) the corresponding phase-locked beat-note spectrum. (e) Final location of the TL after coarse and fine tuning phases and (f) the corresponding lock spectrum……………………………………………………….. 63

2.19 (a) Beat-note spectrum before and after phase locking. (b) Measured phase noise of the locked beat-note and the LO heterodyning signal. (c) Lock spectrum for different f_{LO} settings. (d) Allan deviation measurement result…………………………………………………… 66

2.20 (a) Measurement setup for EOPLL acquisition time and (b) the output of the EOPLL chip which is injected to the gain section of the TL…….. 68

2.21 The block diagram of an OFS that integrates all electronic blocks…….. 71

3.1 (a) The 1-D multi-beam antenna array with three simultaneous outputs. (b) 2-D multi-beam array………………………………….................. 74

3.2 (a) Single-mode and multimode silicon waveguides implemented in IME 180 nm silicon-on-insulator (SOI) photonic process and the corresponding mode profile at 1550 nm. (b) Delay cell microphotograph……………………………………………………… 78

3.3 Optically delayed electrical pulse and comparison of optical and electrical delay lines. (a) Optically delayed electrical signal using a MZM. (b) Optically delayed electrical signal using a ring modulator. In both a and b, the modulator is followed by a delay cell to optically delay the electrical signal $V_{RF,in}$. (c) Schematic of a loaded transmission line with LC segments. Each transmission line segment is 250 µm long and the inductor and capacitor values are 400 pH and 130 fF, respectively. (d) Comparison between the simulated per-delay element loss of the implemented optical delay and that of the LC loaded transmission line for the same delay of 9.8 ps……………………….. 79

3.4 (a) The structure of the photonic-assisted one-dimensional UWB antenna array including 1x2 array of UWB antennas. (b) Directional coupler ratios. (c) Schematic of the 1-D array for *SR* and *FOV* calculation…………………………………………………………… 85

3.5 (a) Structure of the 11x11 imager. (b) Waveguide connections illustrating the delay cell, the waveguide crossings, and the directional couplers. (c) Microphotograph of the photodiode. (d) Microphotograph of the ring modulator. (e) Microphotograph of the 11x11 nanophotonic near-field imager integrated in the IME 180 nm silicon-on-insulator process………………………………………………………………….. 87

3.6 Proposed scheme to address the potential phase mismatch between optical waves at the combining point before each pixel………………... 89

3.7 Chirp generation. (a) Block diagram of the laser frequency chirp generation system. (b) Spectrum of the optical signal with zero modulator bias and, (c) with single-sideband operation biasing condition, where the optical carrier and the undesired sideband are significantly suppressed. The frequency spectrum of the laser is down-converted using an auxiliary laser……………………………………... 91

3.8 1-D delay line array. (a) Schematic of the delay line array with 11 outputs with the required coupling ratios that are chosen based on simulation results. (b) The microphotograph of the 1-D delay line array. (c) The measured optical power at the 11 outputs……………………… 94

3.9 Simplified block diagram illustrating the total optical loss from input grating coupler to each photodiode…………………………………….. 95

3.10 Data read-out circuitry. (a) Matrix of photodiodes as imager pixels. (b) Differential energy detection circuit……………………………………. 96

3.11 (a) Wired measurement setup for characterization of the imager chip. (b) The 4-channel digitally controlled electrical variable delay line. (c) Wired measurement results showing a bright pixel at different locations for different electrical delay settings emulating different angles of incidence………………………………………………….................. 99

3.12 (a) Wireless measurement setup. (b) Wireless measurement results for five different angles of incidence, where a pixel for each case is illuminated…………………………………………………………… 101

3.13 (a) Near-field imaging results. (a) Imaging measurement setup. (b) Three target objects and their near-field images formed using the implemented nanophotonic imager are shown…………………………. 103

3.14 Schematic of the RF front-end of the UWB imager……………………. 105

3.15 Scaling the number of pixels by tiling………………………………… 109

4.1 Simplified block diagram of a 1-D phased array consisting of 8 antennas………………………………………………………………… 112

4.2 (a) Beam width comparison for different number of array elements. (b) Beam steering by changing the relative phases for different element spacings……………………………………………………………. 115

4.3 Conceptual schematic of the proposed NxN OPA, where optical signals traveling in the row and column waveguides have (a) different phases and amplitudes and (b) different phases but the same amplitude………. 119

4.4 (a) The far-field interference pattern of an 8x8 OPA with 64 per-element phase control (top row) and that of an 8x8 OPA with identical element structure and spacing but implemented based on the proposed architecture (bottom row). The diagonal beam-steering (with same relative phase between the elements in rows and columns) is performed. (b) The peak intensity of the main lobe in the far-field pattern for the conventional and proposed 8x8 OPAs………………….. 121

4.5 (a) The structure of the implemented 8x8 OPA with 16 phase shifters placed outside of the array aperture. (b) The structures of the grating couplers (as OPA elements) and directional couplers with varying lengths. (c) The microphotograph of the implemented 8x8 OPA chip fabricated in the IME 180 nm SOI process………………………….. 124

4.6 The structure and microphotograph of the thermal phase shifter………. 126

4.7 The structure and simulated far-field beam pattern of the designed grating coupler……………………………………………………. 126

4.8 (a) Different levels of Si etch. (b) The structure of the directional coupler with partially etched coupling region. (c) Finite-Difference Time-Domain (FDTD) simulation results for the directional couplers with varying length and different silicon etch levels within the coupling region………………………………………………………………. 127

4.9 The structure of the designed compact waveguide crossing……………. 128

4.10 The structures of the nanophotonic waveguides, the waveguide crossing, directional couplers with varying length, the Y-junction, and the grating coupler serving as the OPA element……………………….. 129

4.11 The effect of phase mismatch…………………………………………... 130

4.12 (a) Measurement setup used to characterize the OPA chip. (b) Measured far-field interference pattern showing four grating lobes…… 133

4.13 Demonstration of the 2-D far-field beam-steering. The reference spot is at the center and the pictures around it show the movement of the beam……………………………………………………………….. 134

4.14 (a) Two consecutive resolvable spots while diagonal beam-steering is performed. (b) The beam profiles………………………………………. 135

4.15 Conceptual schematic of a 4x4 OPA that uses two photonic routing layers to reduce the elements spacing within the aperture…………….... 138

4.16 Waveguide gratings as the elements of an OPA………………………... 139

4.17 (a) The schematic of the implemented OPA chip in TowerJazz process that used two levels of photonic routing. (b) The zoomed-in view of the

OPA aperture. (c) The chip microphotograph………………………….. 141
4.18 Simulated beam steering results of the proposed two layer OPA………. 142
4.19 (a) The structure of the thermal phase shifter and (b) its microphotograph. (c) The structure of the photonic via and……………. 143
4.20 (a) The structure and dimensions of a waveguide grating. (b) The waveguide gratings designed for the 8x8 OPA with 3 mm element spacing and (c) the corresponding grating lengths and widths…………. 144
4.21 The measurement setup for OPA characterization that includes a tunable laser source, two digitally controlled phase shifter drivers, and an IR camera………………………………………………………………. 146
4.22 2-D beam steering results using the OPA with 3 μm element spacing…. 148
4.23 Scaling the number of elements by using waveguide gratings and directional couplers with varying length together……………………… 150
5.1 The conceptual block diagram of a fully integrated OFS chip excluding the TL and the reference comb…………………………………………. 156
5.2 Proposed method of scaling the number of pixel of the nanophotonic imager…………………………………………………………………… 157
5.3 Schematic of the proposed OPA row/column with 64 elements……….. 159

List of Acronyms

1-D: On dimensional

2-D: Two dimensional

AAS: Aided acquisition system

AF: Array factor

BPF: Band-pass filter

BW: Bandwidth

CCO: Current-controlled oscillator

CM: Common mode

CMOS: Complementary metal-oxide semiconductor

DBR: Distributed Bragg reflector

DF: Differential

DFB: Distributed feedback

EDFA: Erbium-doped fiber amplifier

EFS: Electrical frequency synthesizer

EOPLL: Electro-optical phase-locked loop

FDTD: Finite difference time domain

FM: Frequency modulation

FOV: Field of view

FSR: Free spectral range

GC: Grating coupler

IIP3: Third-order input intercept point

IM: Intensity modulator

IR: Infrared

LiDAR: Light detection and ranging

LO: Local oscillator

LPF: Low-pass filter

MZM: Mach Zhender modulator

NF: Noise figure

OFC: Optical frequency comb

OFS: Optical frequency synthesizer

OPA: Optical phased array

PC: Polarization controller

PCB: Printed circuit board

PD: Photodiode

PL-FOM: Phase locking figure of merit

PLL: phase-locked loop

PM: Phase modulator

RF: Radio frequency

SFDR : Spurious free dynamic range

Si: Silicon

SiN: Silicon nitride

SNR: Signal-to-noise ratio

SOI: Silicon-on-insulator

SR: Spatial resolution

SSB: Single sideband

TIA: Trans-impedance amplifier

TL: Tunable laser

TTD: True-time delay

UWB: Ultra-wideband

VCO: Voltage-controlled oscillator

VNA: Vector network oscillator

CHAPTER 1

Introduction: Integrated electronic-photonic systems

Integrated electronic systems implemented on silicon platforms have been extensively used in various areas of science and engineering from communications to medicine. Mature fabrication processes with very high yield, large-scale production at a low per-device cost, and integration of fairly complex systems on very small footprints are among the main reasons for the increasing demand for electronic chips. Based on these unique features, micro/nano electronic technology has been used to enhance the performance of different systems in other fields of research such as bio-sensing, imaging, and optics to name a few.

Since early 2000, silicon photonics has become increasingly popular as it enables integration of large bench-top optical systems that reduces the overall size, cost, and power consumption by orders of magnitude. Low propagation loss and high optical confinement provided by silicon-on-insulator (SOI) platforms enable implementation of many active and passive photonic components such as waveguides, detectors and modulators on electronic compatible platforms [1,2]. This paves the way towards co-integration of electronic and photonic components on the same platform enabling the integration of a wider range of previously known bench-top systems, as well as a vast variety of novel applications in engineering, science, and medicine.

System comprised of both electronic and photonic components and blocks can be categorized into two main types. Electronic-assisted photonic systems, which benefit from the fact that complex electronic circuits can be used to control and enhance the performance of the photonic systems [3-5]. Similarly, photonic-assisted electronic systems utilize the unique features of photonic components such as low waveguide propagation loss to implement systems with performances that are very challenging to be achieved in electronics-only implementations [6-8].

In this thesis, benefiting from the co-design of electronic and photonic systems, three different examples of integrated electronic photonic systems are presented. These applications include optical frequency synthesis, optical processing of microwave signals, and solid-state optical beam steering.

1.1 Optical frequency synthesis: a partially integrated approach

Similar to electrical frequency synthesizers (EFS) that have been widely used in almost all RF and microwave systems, optical frequency synthesizers (OFS) have many applications in communications, sensing and imaging, radar and ranging, and spectroscopy, to name a few. OFSs have been studied for many years and in fact, early works date back to 1980s. However, OFSs are not as commonly and widely used as EFSs. Integration of EFSs on small chips is the main driving force behind this widespread use. In contrast, implementation of OFSs have been mainly limited to bench-top systems that are large, expensive, and consume a large amount of power. Therefore, integration of these systems is a critical step towards their large scale deployment.

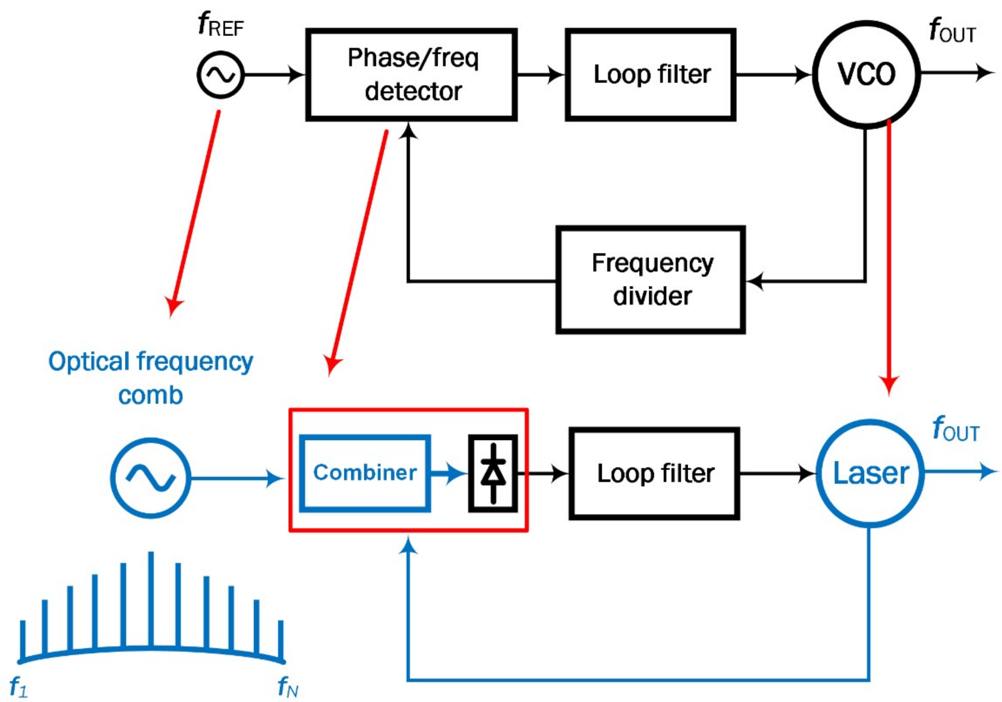

Figure 1.1 – Comparison of a typical EFS and an OFS.

Figure 1.1 shows the simplified block diagram of an EFS, where a voltage-controlled oscillator (VCO) is phase locked to a stable low-noise reference and by adjusting the frequency division ratio, an arbitrary electrical frequency can be generated. Since the implementation of a frequency divider that can divide optical frequencies to electrical ones is very challenging, some other method should be used to implement an OFS.

With the advent of optical frequency combs (OFC), a common approach is to use an OFC as the reference of the OFS and lock a tunable laser (acting as the current-controlled oscillator or CCO) to any of the comb teeth. The OFC is stabilized using extremely stable microwave oscillators and covers a wide range of frequencies. Therefore, it is a good candidate to be used in an OFS. Figure 1.1 also shows a typical OFC-based synthesizer where the electrical reference is replaced with an OFC, the phase/frequency detection is done by using an optical power combiner followed by a photodiode, the VCO is replaced with a tunable laser (TL) and the frequency divider is eliminated.

Moreover, as discussed in details in Chapter 2, a heterodyne electro-optical phase-locked loop (EOPLL) can be used in order to phase-frequency lock the TL and fine-tune its frequency with respect to the reference.

It is highly desired to integrate the whole OFS system shown in Fig. 1.1 on a chip. The integration involves multiple different blocks. First, the OFC should be integrated which is a challenging task but with recent advances, many on-chip frequency combs have been reported. Of course, it also requires an involved process of comb stabilization which is beyond the scope of this thesis. In the rest of the system, the EOPLL is the core block that is responsible for phase locking of the TL to the reference OFC. Demonstration of an OFS with integrated EOPLL is one of the main steps towards full integration. Finally, the rest of the electronic blocks will be integrated with the OFC and EOPLL chips. The focus of this thesis is in Chapter 2 on a partially integrated OFS that uses an EOPLL chip for stable phase-frequency locking to demonstrate high resolution synthesis over a wide range of optical frequencies. Chapter 2 of this thesis contains detailed information about the design and implementation of the proposed OFS.

1.2 Optical signal processing

Over the past decades, advancements in semiconductor fabrication processes have enabled powerful digital and analog circuits for a vast variety of application from personal computers to smartphones and communication systems. Latest technology nodes provide nanoscale feature sizes that reduce the parasitic elements in a circuit and enable implementation of high frequency and large bandwidth systems. However, different factors such as large electrical loss of electrical waveguides at microwave frequencies and electromagnetic interference make the design of high frequency systems rather challenging.

Integrated photonic platforms offer very large bandwidth, low propagation loss, and immunity to electromagnetic interferences. These features address the challenges with electrical counterparts and enable efficient signal processing in the optical domain. Therefore, optical processors have increasingly gaining attention for different applications from communications to imaging.

In a typical microwave imaging system, an array of antennas is used to receive from signal from different directions. The signal coming from an object is received by multiple antenna and after processing, the corresponding image can be formed. One common way of processing and delaying the received signals is by using true-time delay elements. Since the signals coming from different directions arrive at different times, they constructively interfere after passing through delays that are properly set, resulting in a large signal that can be detected and used to find the direction of incidence. Such systems have been mostly implemented using bench-top setups that are bulky, power hungry, and expensive. Moreover, since the processing of the signals happens in electrical domain, these systems are susceptible to electromagnetic interferences.

One way to address these challenges is to use antenna arrays with integrated electronics [9]. Figure 1.2 shows this concept in which signals coming from different angles are received by four antennas. After going through a network of delay elements, these four signals constructively interfere at the corresponding pixel. This architecture benefits from sharing the delay elements for different pixels to reduce the total number of pixels [9]. For instance, the signal coming from direction 2 (red) is first received by A_2, then by A_1 and A_3, and finally by A_4. Therefore, these signals constructively interfere at the pixel closer to A_4.

In the electrical approach, the delay elements are typically implemented using transmission lines that are loaded by inductors and capacitors. This approach enables smaller, lower power, and less expensive systems compared to the bench-top ones. However, there are still challenges that limit the scaling to imagers with a large number of pixels. Large propagation loss of the electrical transmission lines, especially compared to that of optical counterparts, necessitates the use of repeating amplifiers to compensate for the variation of electrical power across the delay network that in turn, increases the power consumption of the system. In addition, the large number of inductors required for the delay elements, consumes a large silicon area, making the chips more expensive. Since the processing still happens in electrical domain, electromagnetic interferences as well as cross-talk between the inductors, can significantly degrade the performance of the systems.

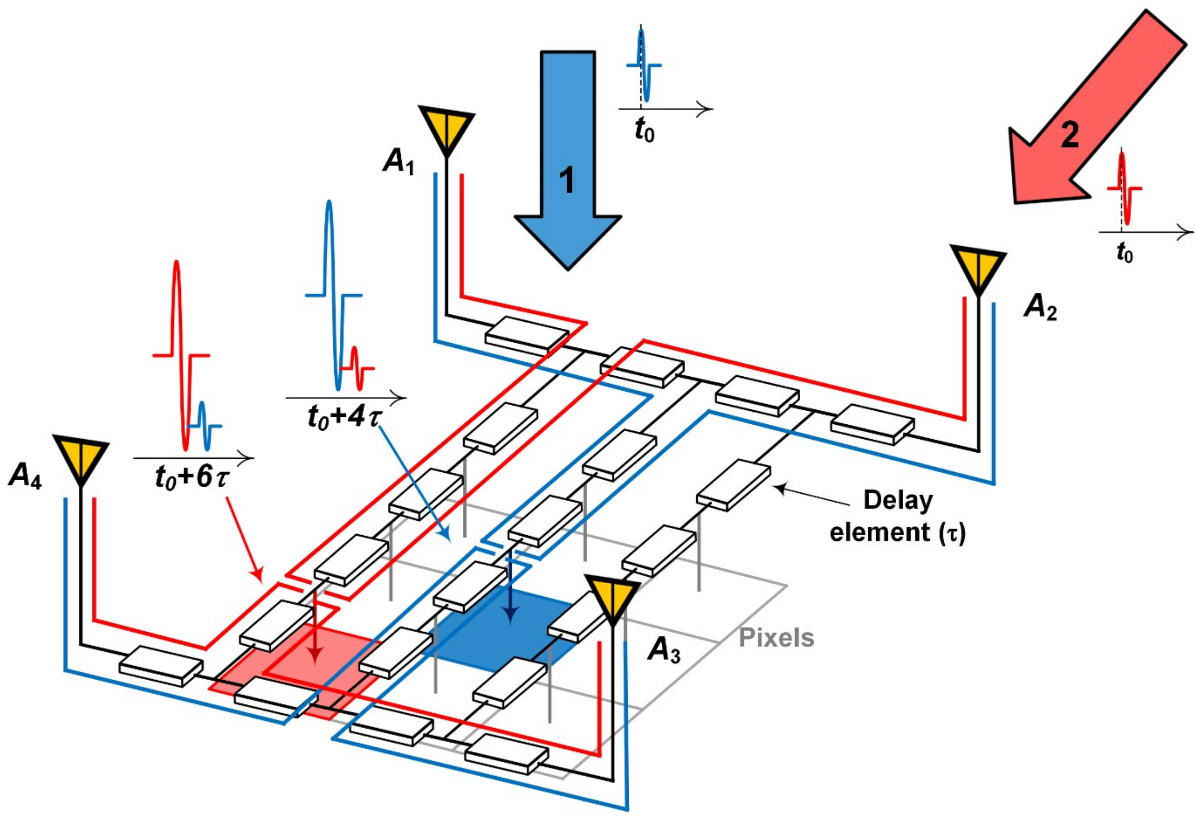

Figure 1.2 – The schematic of a multi-beam imager by sharing the delay elements between the pixels.

Optical signal processing can be used to address these challenges by using nanophotonic silicon waveguides instead of the electrical transmission lines that significantly reduces the loss and enables more compact delay elements due to the higher index of refraction of silicon and therefore lower group velocity. In this thesis, the first nanophotonic microwave near-field imager is presented that receives the microwave ultra-wideband signals, up-converts them to the optical domain using modulators, processes the signals using on-chip nanophotonic delay elements, and forms the image by converting the processed signals back to the electrical currents using photodiodes. The 121-element imager, which is integrated on a silicon chip, is capable of simultaneous processing of ultra-wideband microwave signals and achieves 4.8° spatial resolution for near-field imaging with orders of magnitude smaller size than the benchtop implementations and a fraction of the power consumption. The details of the design and implementation of the imager chip as well as the imaging demonstration results are presented in Chapter 3 of this thesis.

1.3 Optical beam steering

Initially intended for use in radar systems to steer the radio waves across the sky to detect planes, phased arrays have been used for different applications for many years. From radar and object tracking to communication systems, phased arrays consist of a 1-D or 2-D array of transmitting or receiving antennas (elements) that, depending on their relative phase, are capable to transmit to or receive from a specific spatial direction. Typically, phase shifters are used to set the relative phase between the elements. Figure 1.3(a) shows the conceptual block diagram of a 1-D transmitting phased array with 8 elements. By properly setting the relative phases, the systems can transmit in a certain spatial direction by forming a far-field interference pattern that results in a narrow beam, while in other directions no or very small signal is transmitted.

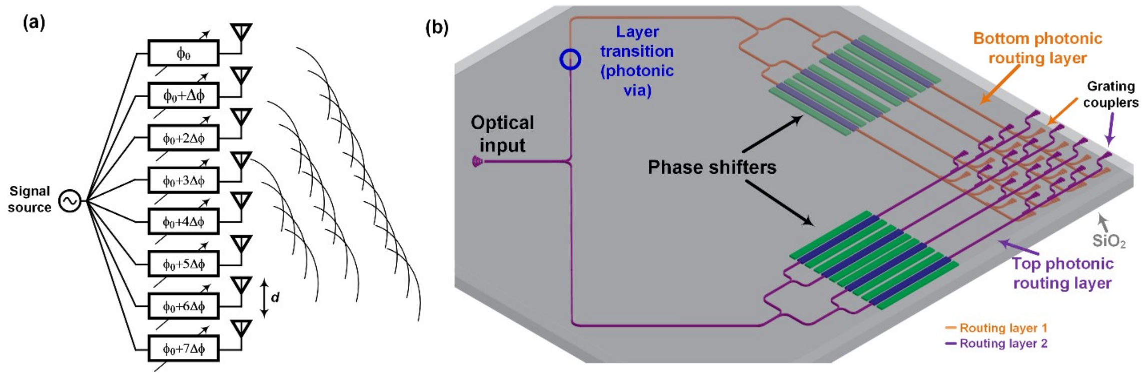

Figure 1.3 – (a) Conceptual block diagram of a 1-D 8-element phase array. (b) A Compact 4x4 optical phased array for 2-D beam steering using 8 phase shifters and two layers of photonic routing to achieve close to half-wavelength element spacing.

Two parameters are very important in the design and performance of the phased array: element size, element spacing, and the total number of elements. Depending on the frequency (wavelength) of operation, the size of the elements vary. For instance, in microwave domain the size of the elements is in the order of a few millimeters to a few centimeters while in the optical domain, they are three or four orders of magnitude smaller. Moreover, in an ideal case, the spacing between the elements should be half of the wavelength of operation to achieve a wide beam steering range as well as large side-lobe suppression ratio. Finally, the number of elements sets the far-field beam width and to achieve a narrow beam to have a high spatial resolution, one should increase the number of the elements within the phase array aperture.

In the microwave domain, because of the wavelength values, it is a straightforward task to implement a phase array with large number of elements and half-wavelength element spacing to achieve a high quality beam. However, such a task is very challenging in the optical domain as the wavelength value necessitates sub-micron element spacing to achieve large beam steering range and side-lobe suppression ratio. This is due to the difficulty of designing very compact optical antennas and placing them at half-wavelength spacing since typically the elements are a few micron on each side. In addition, photonic and electronic routings to distribute light and control the optical phase of the elements, limit the element spacing even more. Therefore, to implement optical phased arrays (OPA) with performances similar to those of the microwave phased arrays, one should implement compact optical antennas and employ creative ways of light distribution and controlling the relative phase between the elements.

In this thesis, novel OPA architectures are presented in which the routing complexities are addressed by reducing the number of phase shifters in a 2-D system, and compact OPA aperture is achieve by benefiting from a photonic fabrication process with two layers of photonic routing. Figure 3.1(b) shows the conceptual schematic of the proposed solutions. In this 4x4 OPA, 8 phase shifters are used to control the relative phases between the elements instead of the conventional use of 16 phase shifters. This significantly reduces the routing complexity and power consumption especially in OPAs with large number of elements. In addition, by implementing two sets of elements and combining their signals vertically, very compact aperture can be achieved. Two 8x8 OPA chips are designed and implemented as proofs of concept and 2-D beam steering is demonstrated. The details of the proposed approaches are presented in chapter 4 of this thesis.

1.4 Thesis outline

The topics that were discussed in sections 1.1 to 1.3, are presented in details in the rest of this thesis. A partially integrated optical frequency synthesizer is presented in chapter 2. First, the importance and applications of an OFS is discussed and is compared with the typical implementation of an EFS. The step by step principle of operation of the proposed OFS based on an optical frequency comb is explained in which a coarse tuning phase and fine tuning phase are used to phase lock a widely tunable laser to the teeth of the OFC. Because of using an integrated heterodyne EOPLL, high resolution synthesis can be performed. Since the performance of the TL is critical in the process of frequency synthesis, the full characterization of the TL in terms of wavelength tuning is presented. Moreover, the FM response of the TL as the main limiting factor of the phase locking loop bandwidth is discussed in details. As the beginning phase of the synthesis process, the coarse tuning and tooth indexing systems are explained and the corresponding characterization results are shown. After the coarse tuning phase, the EOPLL chip is engaged to perform phase-frequency locking. To study the effect of integrating photonic and electronic devices on the same chip to realize the EOPLL on the loop stability, the theoretical analysis of nonlinear operation of the EOPLL is investigated in details. In addition, the theory of operation of the heterodyne EOPLL is presented. These theoretical studies are followed by detailed characterization results of the EOPLL as well as the novel frequency detection scheme. An aided acquisition system is added to the OFS system to enhance the acquisition range of the EOPLL and overcome some of the challenges such as false locking and temperature stabilization. Finally, the full system is used to demonstrate optical frequency synthesis using an electro-optic frequency comb as the reference to the OFS.

In chapter 3, the first nanophotonic near-field microwave imager is presented. First, the motivation behind the work including the applications of near-field imagers and the shortcomings of the bench-top and fully electrical implementations is presented. The idea of multi-beam antenna arrays and their application in designing an imager is discussed. The main concept behind the proposed nanophotonic imager is the fact that one can optically delay an electrical signal. The theory of this concept is studied to show how modulating light with an electrical signal and delaying it, delays the electrical signal by the same amount. This results in more compact optical delay elements compared to the electrical counterparts that together with the lower loss of the optical delay elements, are the main reasons of the advantage of the proposed system over the conventional methods. The system architecture is explained thoroughly. One challenge in this system is that the coherence of the input light can cause variations in the intensity of pixels. A solution based on frequency chirping the input laser is proposed and the corresponding theoretical study are presented. The imager chip is characterized in terms of optical signal distribution and single pulse source measurements to ensure that the chip can distinguish between the signals coming from different angles. Finally, using metallic target objects, near-field imaging is demonstrated, where the target objects are illuminated by a train of UWB microwave pulses and the reflected signals are optically processed by the chip to form an image. A way of scaling up the number of pixels of the imager is proposed as the potential continuation of this work.

Chapter 4 presents a novel OPA architecture that has been proposed as a way towards ultra-compact phase arrays. The basics of phased arrays is explained and the effect of increasing the number of elements as well as reducing the spacing between them are studied through simulations. Since the wavelength of optical signals is much smaller than that of microwave signals, achieving half-wavelength element spacing in OPAs is an open problem. The proposed solution consists of two main steps towards the implementation of ultra-compact OPAs. First, we reduce the number of phase shifters in an N×N OPA by a factor of N/2 for 2-D beam steering using a novel architecture. This architecture significantly reduced the photonic and electrical routings as well as the power consumption that enable more closely-spaced OPA elements. The theory of operation of this scheme is studied showing that in fact by properly setting the phase of row and column signals of the OPA, one can set the relative phase between the elements in order to perform single-beam steering. The theoretical study is followed by simulation results for further investigation. An 8×8 OPA chip with 11 μm element spacing using the proposed architecture is fabricated in a 180 nm SOI process as a proof of concept. The details of the design of the system including the photonic components and the effect of layout mismatches are discussed. Then, the demonstration results of 2-D beam steering using the chip are presented. After showing that an OPA with reduced number of phase shifters can be used for 2-D beam steering, the element spacing within the aperture is further reduced by benefitting from a photonic fabrication process that provides two layers of photonic routing in silicon and silicon nitride. In this process, beam steering in each of the X and Y directions can be done by having two apertures: one in Si layer and one in SiN. These layers are placed in near-field of each other that can be leveraged to combine the beams vertically. Therefore, by eliminating many photonic components that were previously used to combine the row and column signals, the elements can be placed much closer to each other. Moreover, waveguide gratings are used to have smaller elements. A new 8x8 OPA chip with 3 μm element spacing is fabricated in a 180 nm SOI process as a proof of concept that features both reduction of phase shifters and two-layer photonic routing. The details of the design of the elements are presented as well as other photonic devices. Finally, 2-D beam steering results using the new chip is demonstrated and the results are presented.

Finally, chapter 5 presents a summary of my PhD works and discusses the potential future research directions that can be considered as the continuation of these works.

CHAPTER 2

Synthesis of optical signals: Towards integrated optical frequency synthesizers

Today, integrated electronic frequency synthesizers (EFS) play a key role in many applications ranging from communication to detection and sensing [10-12]. In any of these systems, there is a need for generating an arbitrary and configurable radio/microwave frequency. For instance, such a signal can serve as the carrier signal in a communication system or as the pilot signal in a radar system. Figure 2.1 shows the conceptual block diagram of a typical EFS. In this figure, frequency synthesis is performed by phase-locking a voltage-controlled oscillator (VCO) to a lower frequency reference oscillator with significantly lower phase noise and higher stability. A phase/frequency detector measures the error signal between the output frequency (f_{OUT})

and the reference frequency (f_{REF}). The error signal, after proper processing, is fed back to the VCO to achieve the desired output frequency. In this case, the phase locking is accomplished using integrated frequency dividers that divide down the VCO frequency by a generally reconfigurable factor, allowing direct comparison with the lower frequency reference oscillator. By adjusting the division ratio, different frequencies can be synthesized using a single reference frequency. Such a system has been implemented using both bench-top and integrated systems. The integrated EFSs are especially beneficial since they can be deployed in large-scale in various systems at a significantly lower cost, lower power consumption, and small physical size compared to the bench-top counterparts. In fact such systems have enabled many low-cost handheld communication and sensing devices such cellphones and handheld radar units.

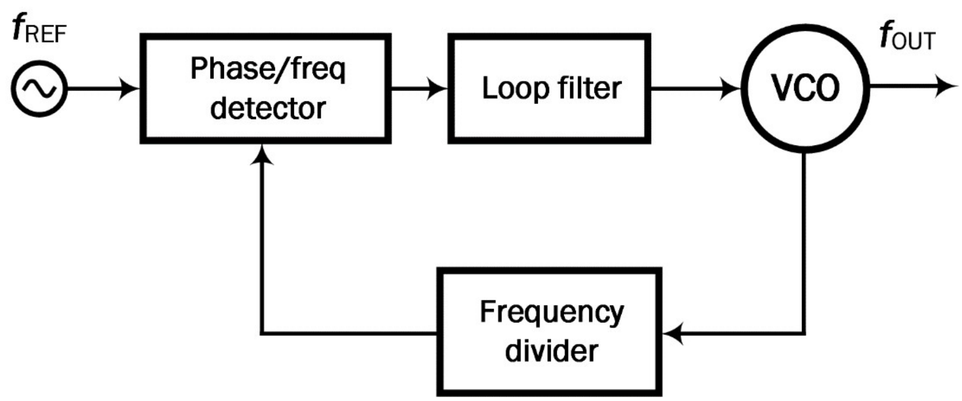

Figure 2.1 – Block diagram of a typical EFS

In the optical domain, a tunable, stable, and low-noise optical frequency is essential for many different communication and sensing systems. However, achieving all three criteria at the same time in a single laser is very challenging. For instance, highly tunable, relatively low-noise lasers are available that have poor frequency stability characteristics [13] and there are highly stable and low-noise lasers that are tunable for only a fraction of nanometers [14]. Therefore, a system like an EFS is required to realize the above criteria at same time and optical frequency synthesizers (OFS) are the most common solution. Largely tunable OFSs also have many applications including optical communication [15], frequency metrology [16], and spectroscopy [17]. Ideally, optical synthesis should be performed by phase-locking a laser to a stable low phase noise electrical oscillator as shown in Fig. 2.2(a). The frequency of a semiconductor laser can be tuned by changing its gain section bias current and therefore it can be modelled as a current controlled oscillator (CCO) [18]. This is illustrated in Fig. 2.2(b). In this case, a change of $i_c(t)$ in the laser bias current results in a change of $K_{laser}\int i_c(t)dt$ in the instantaneous phase of the laser electric field, where K_{laser} is the laser current to frequency conversion gain. However, realization of an optical frequency divider that is capable of performing frequency division from optical frequencies to radio frequencies is very challenging. This is mainly because it requires several different material systems and efficient non-linear frequency conversion at different frequencies. The alternative solution is to replace the electrical reference signal with an optical one, *i.e.* a laser, and use an electro-optical phase-locked loop (EOPLL). Figure 2.2(c) shows the conceptual diagram of an OFS where the frequency divider is eliminated and the output tunable laser (TL) is locked directly to the reference laser. In this architecture, the phase detector can be implemented by beating the two lasers and using a photodiode (PD) to generate a current that is proportional to the phase difference between the lasers [19]. This is shown in Fig. 2.2(d), where the electric fields of two lasers, $E_1 = \sqrt{P_1}e^{j\Phi_1}$ and $E_2 = \sqrt{P_2}e^{j\Phi_2}$ are combined and photo-detected. The photo-current is written as $i(t) = R\left[P_1 + P_2 + 2\sqrt{P_1 P_2}\cos\left(\Phi_1 - \Phi_2\right)\right]$, where R, P_1, P_2, Φ_1 and Φ_2 are the photodiode responsivity, the optical power of the first and second lasers, and the instantaneous phase of the first and second lasers, respectively.

There are two main issues with the architecture shown in Fig. 2.2(c): limited tuning range as well as reference stability. The tuning range is limited by the loop bandwidth (typically a few MHz) and the reference laser needs to be highly stable. As shown in Fig. 2.2(e) the limited tuning range can be addressed by using multiple references at different frequencies. The TL can be locked to any of the references and hence, the tuning range can be extended. However, this solution is not practically desirable since it requires multiple stable lasers as the set of references.

Recent advancements in demonstration of integrated optical frequency combs [20-21] enable implementation of a highly stable frequency comb serving as the reference signal for an OFS. Therefore, for wide range optical frequency synthesis, a highly stable optical frequency comb (OFC) is often used as the reference frequency and the frequency synthesis is performed by phase-locking a widely tunable laser to different reference comb teeth [15-17] as shown in Fig 2.2(f).

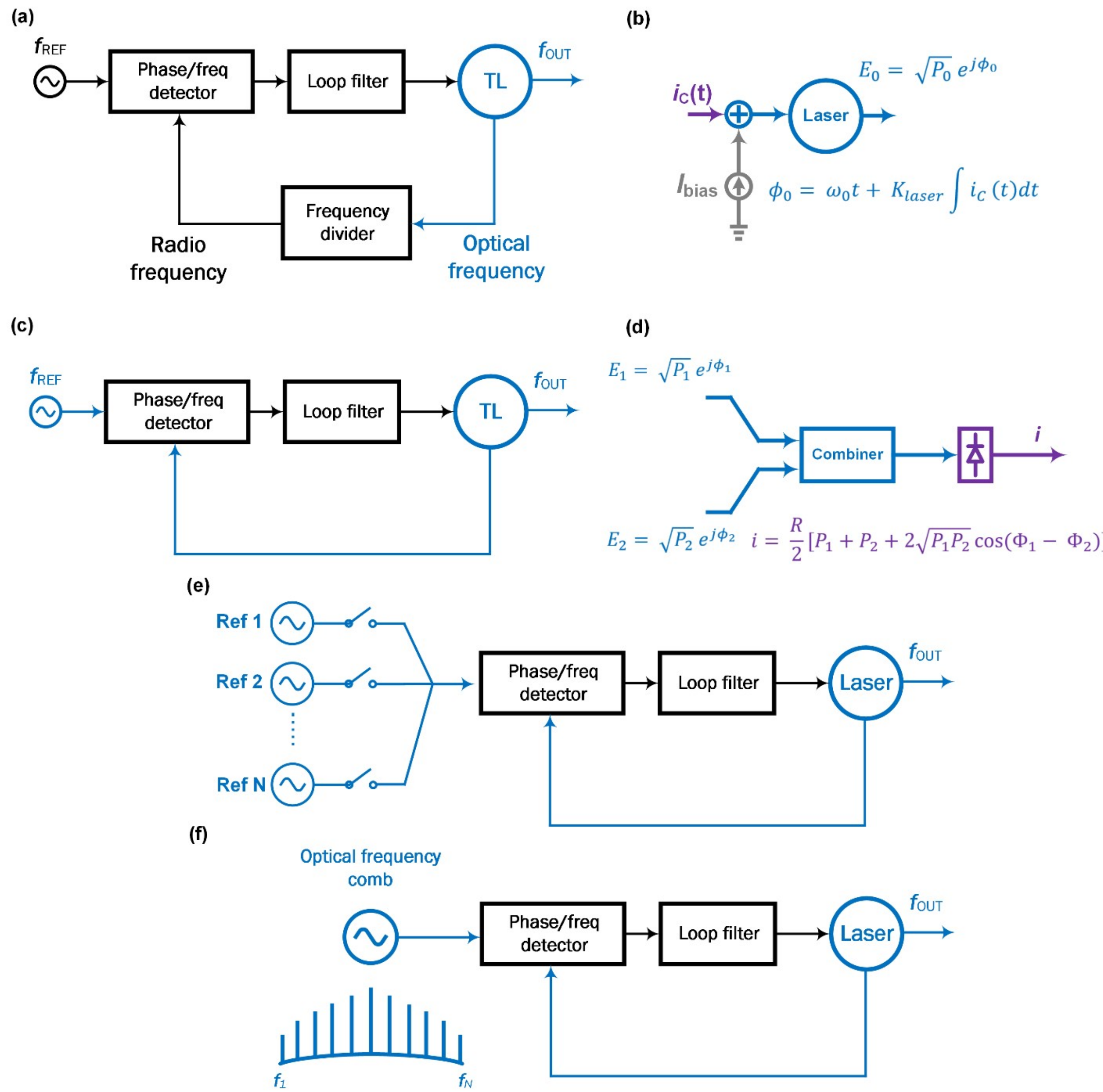

Figure 2.2 – (a) Replacing the VCO in and EFS with a semiconductor laser to synthesize optical frequencies. (b) The model of a semiconductor laser acting as a CCO. (c) The block diagram of an OFS after eliminating the frequency divider and using an optical reference. (d) Implementation of the phase detector using an optical power combiner following by a PD. (e) Enhancing the tuning range by having multiple references. (f) Using frequency comb as the reference to simultaneously enhance the tuning range and stability.

The OFC can be extended across a large range of frequencies that addresses the limited tuning range issue. Moreover, the teeth of an OFC are typically stabilized referenced to a stable RF/microwave source [23]. Therefore, both issues concerned with the architecture in Fig. 2.2(c) could be addressed by using an OFC as the reference (Fig. 2.2(f)).

To date, although many complex integrated electronic-photonic systems have been demonstrated [24-26], optical frequency synthesizers have been mostly demonstrated using bench-top implementations. In these implementations, very stable references can be used which results in high quality of phase locking and the synthesis performance. Despite excellent performance, such systems typically suffer from large physical size, high power consumption, and high cost which make their large scale deployment, especially in mobile and low-power applications, rather challenging. Therefore, there is a large need for fully integrated OFSs.

This chapter presents a partially integrated OFS in which an integrated EOPLL is used as the core block. The rest of this chapter is organized as follows. In section 2.1, the top-level system architecture as well as the two-phase synthesis process (i.e. coarse and fine tuning phases) are discussed. Section 2.2 presents the details of characterization of the tunable laser. Coarse tuning an indexing systems are discussed in Section 2.3. The fine tuning phase is performed using an integrated EOPLL chip and the design and characterization results are discussed in Section 2.4. Section 2.5 contains some of the challenges in design and implementation of the partially integrated OFS. Finally, the frequency synthesis demonstration results are presented in Section 2.6. Section 2.7 summarizes the chapter and provides some potential future works.

2.1 Principle of operation and system architecture

The proposed partially integrated OFS uses an OFC as the reference signal to which a widely tunable distributed Bragg reflector (DBR) laser is phase locked using an integrated heterodyne EOPLL chip. This section present the principle of the operation of the OFS that uses a two-phase process in order to synthesize a desired optical frequency.

2.1.1 Principle of operation

As mentioned before, the proposed OFS works based on a two-phase process; a coarse tuning phase and a fine tuning phase. Figure 2.3 illustrates these phase. Assuming that an OFC with 500 MHz teeth spacing or free spectral range (FSR) is used as the reference signal, the initial position of the TL with respect to the comb is shown in Fig 2.3(a). Consider the case that the TL is supposed to be tuned to a frequency which is 5.7 GHz larger than its initial frequency to synthesize a new frequency. Considering the 500 MHz tooth spacing, the target 5.7 GHz can be decomposed into two parts. In a coarse tuning phase, the TL is tuned while a counter keeps track of the passing teeth. The TL is tuned for 5.5 GHz which corresponds to passing 11 comb teeth. After counting 11 teeth while the TL is being tuned, its new location is marked in Fig 2.3(b).

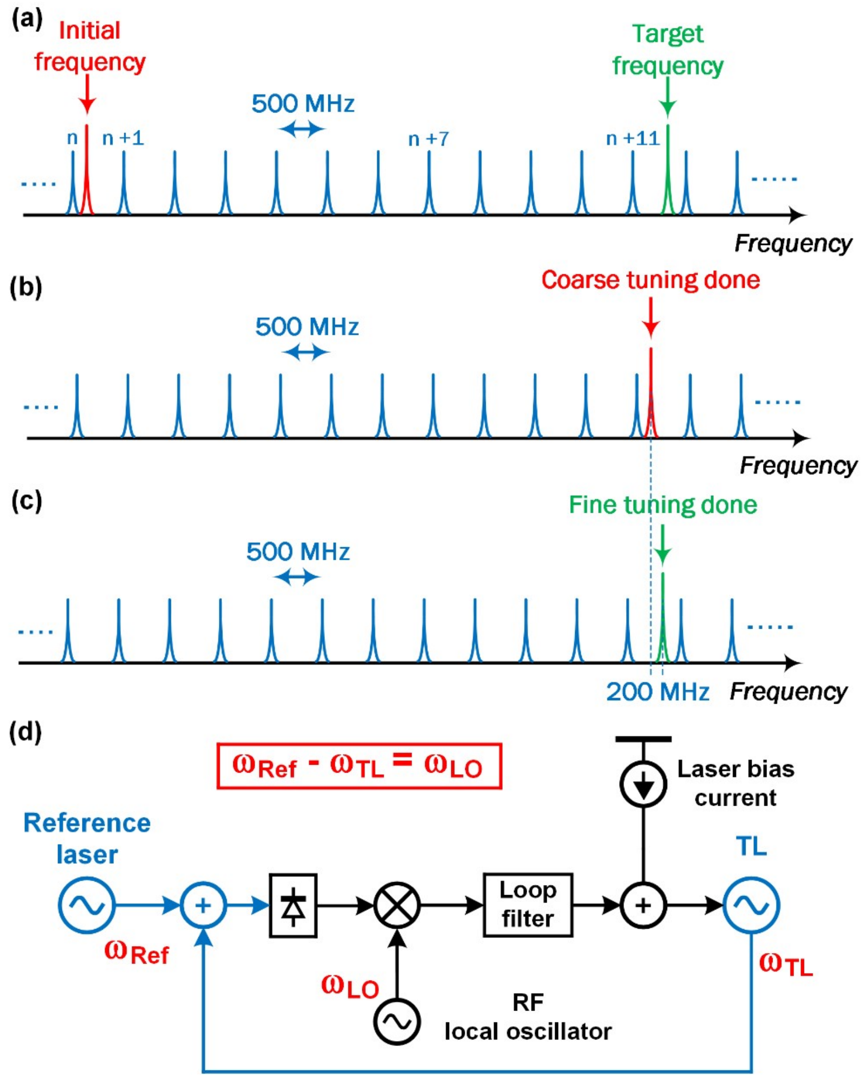

Figure 2.3 – Frequency synthesis using a coarse tuning and a fine tuning phase. (a) The initial frequency of the TL and the target frequency that is 5.7 GHz higher. (b) Coarse tuning after counting for 11 teeth. (c) Fine tuning using a heterodyne EOPLL for 200 MHz. (d) The block diagram of the heterodyne EOPLL.

Then, as shown in Fig. 2.3(c), the TL can tuned for the remaining 200 MHz in a fine tuning phase using a heterodyne EOPLL. The simplified bock diagram of a heterodyne EOPLL is shown in Fig. 2.3(d) [27]. The principle of operation of the EOPLL will discussed in more details in section 2.4. Here, the reference laser and the TL are combined and photo-detected which, as shown in Fig. 2.2(d), act as the phase detector. The resulting signal (beat note) at frequency $\omega_{\mathrm{Ref}} - \omega_{\mathrm{TL}}$ is then mixed with a RF local oscillator signal at frequency ω_{LO}, creating an error signal that is fed back to the TL after filtering. Under the lock condition, the signal injected to the TL is DC which necessitates that $\omega_{\mathrm{Ref}} - \omega_{\mathrm{TL}} = \omega_{\mathrm{LO}}$. Therefore, by adjusting the LO frequency, the frequency of the TL can be tuned with respect to the reference frequency. Since this can be done with very high resolution (sub-Hz), it is used for fine tuning the TL with respect to the reference. A similar process can be utilized to synthesize any other frequency within the range of the OFC.

2.1.2 System architecture

The block diagram of the proposed optical synthesizer is shown in Fig. 2.3(a). The synthesizer consists of a reference OFC, a widely tunable laser (TL), the integrated EOPLL for fine tuning, the aided acquisition system (AAS) that enhances the acquisition range of the phase locking system, the indexing system that monitors the number of passing teeth, and the laser control and driver unit for coarse and fine tuning. A stable, low-noise frequency comb is generated using phase-only modulation of a continuous-wave laser [28] and is used as the reference for the synthesizer. The OFC contains many teeth with tooth spacing of 500 MHz. The TL is custom fabricated DBR laser made by Inifinera Corporation. The simplified structure of the laser is shown in the inset of Fig 2.4(a). The TL consists of four main sections: back mirror, gain section, thermal phase section, and front mirror. By controlling the operating point of these sections, it is possible to coarse and fine tune the laser. Mirrors and the phase section are used for coarse tuning and the gain section is used for fine tuning and phase locking the TL to the reference. More details about the laser and its characterization process is presented in Section 2.2.

In order to perform frequency synthesis, the TL should be first coarse-tuned to the vicinity of the target frequency. In the coarse tuning phase, the microcontroller performs continuous laser tuning by sending proper signals to the laser driver, which injects corresponding currents to the mirrors and phase sections of the TL. As the TL is tuned, the indexing system, which monitors the beat-note between the TL and the comb teeth, detects and counts the number of passing comb teeth. When the TL reaches the target comb tooth, the microcontroller stops the coarse tuning and holds constant the mirrors and phase section currents generated by the laser driver. At this point, the aided acquisition system and the EOPLL are engaged. The aided acquisition system is used to enhance the acquisition range of the EOPLL to cover the tooth-spacing of the reference comb.

The EOPLL performs phase-frequency locking of the TL to the comb tooth right next to the target tooth (acquired in the coarse tuning phase). In the case shown in Fig. 2.4(b), once the TL reaches the target comb tooth after counting a certain number of teeth, the EOPLL phase-locks the TL to the tooth right after the target comb tooth. This is due to the fact that in a heterodyne EOPLL, under the lock condition, the frequency of the TL and the reference optical frequency are offset by the frequency of the heterodyning local

RF oscillator [29]. For tooth-spacing of 500 MHz, this local oscillator is tuned from 250 MHz to 500 MHz to span the tooth-spacing. Similarly, if the desired frequency is on the left side of the target comb tooth (Fig. 2.4(c)), the tooth right before the target tooth is selected as the reference to the heterodyne EOPLL. Note that because of the heterodyne design of the EOPLL, the TL, when in between two teeth, is always phase locked to the further tooth (i.e. at a frequency distance of 250 MHZ to 500 MHz).

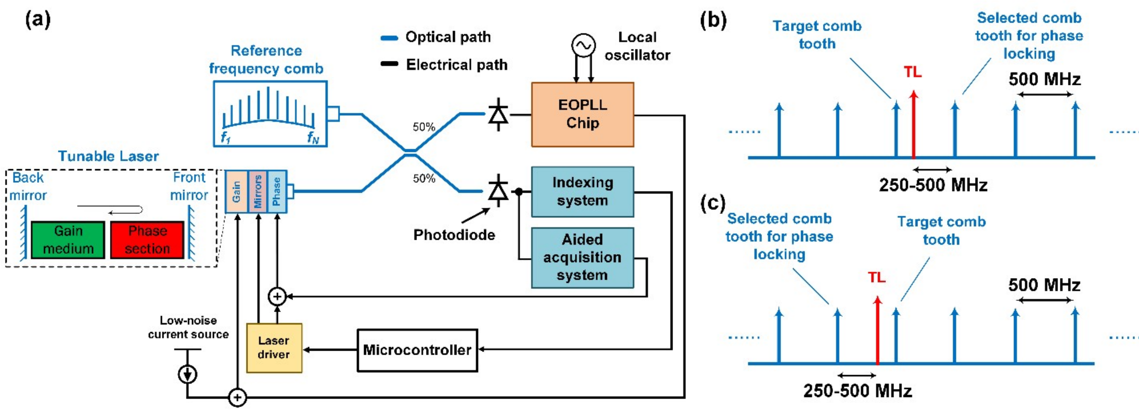

Figure 2.4 – (a) Block diagram of the partially integrated OFS. (b) The EOPLL phase locks the TL to tooth right after the target comb tooth. (c) The reference to the EOPLL is the tooth right before the target comb tooth.

2.2 Tunable laser characterization

Before performing frequency synthesis, it is required to characterize the TL to find its output wavelength or frequency as a function of different section settings. Inside the cavity of a typical laser, light is reflected back and forth between two mirrors and an active medium, the gain section, which is placed between the mirrors, provides gain to sustain the oscillation. The lasing frequency is inversely proportional to the total time it takes for the light to travel between the mirrors and depends on the cavity length and the effective index of refraction of the laser cavity. Therefore, to adjust the lasing frequency to a desired value, these properties should altered correspondingly.

Here, a widely tunable DBR laser, custom fabricated by Infinera Corporation, is used for optical frequency synthesis. The TL is comprised of four sections: gain, phase, front mirror, and back mirror as depicted in Fig. 2.5(a). The gain section is biased using a low-noise dc current source and is also connected to the output of the EOPLL chip to perform phase locking. The gain section of the Infinera laser has a gain of 1.5 GHz/mA at a dc current of 80 mA. The phase section can be modelled as a resistor and used to thermally fine tune the laser wavelength over a small range (<0.5nm) and has a resistance of 30 Ω. The Bragg reflectors (mirrors) can be tuned by adjusting their refractive index through the carrier injection effect. To change the refractive index of the mirrors, electrical current should be injected to them appropriately. The TL can be monotonically and continuously tuned by simultaneous tuning of front and back mirrors in the same direction. In the rest of this section, this is called common-mode tuning.

The range in which the change in emission wavelength of the TL is continuous and monotonic is limited to a few nanometers and is referred to as a “super-mode”. When front and back mirrors are tuned in the opposite directions (differential tuning), the laser cavity condition may change such that an abrupt and relatively large shift occurs in the laser’s emission wavelength resulting in a mode hop [30] where the emission is set to a different super-mode.

With the combination of the common-mode and the differential tuning of the Bragg mirrors, the TL can be tuned continuously over a large wavelength range. Note that within a super-mode, the monotonic change in wavelength is primarily continuous but may incur small frequency jumps. These small jumps may be tuned across by adjusting the current of the thermally tuned phase section.

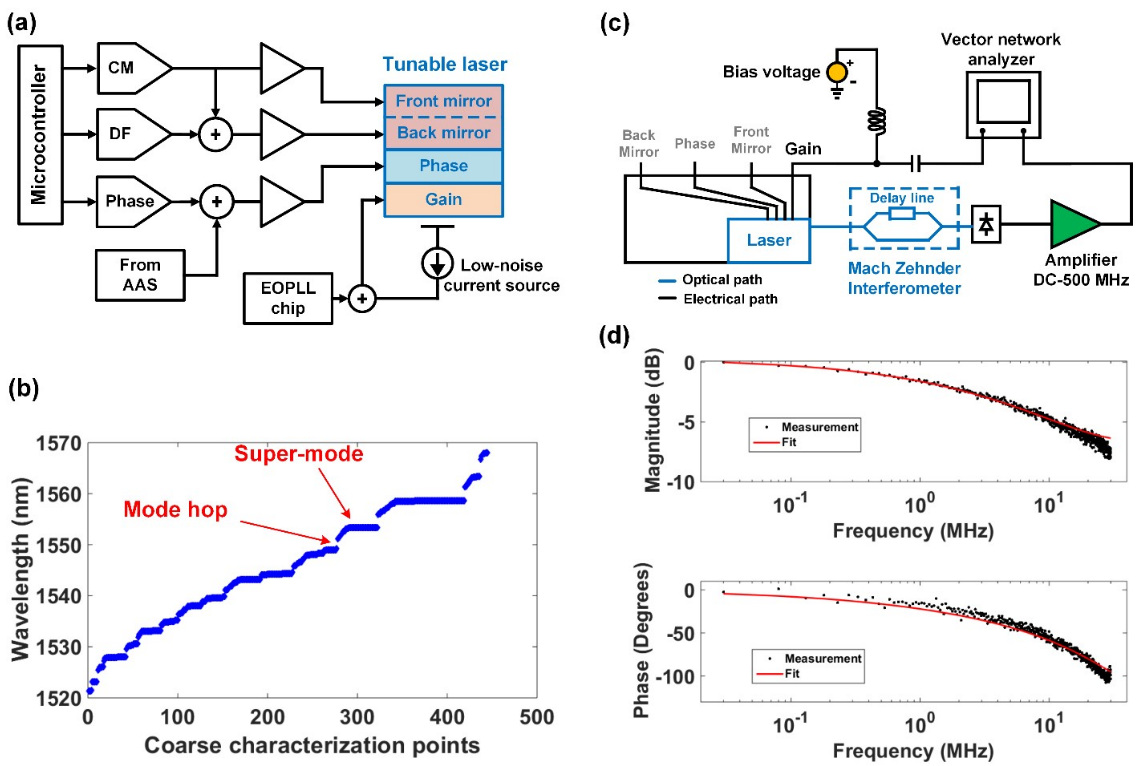

Figure 2.5 – (a) Block diagram of the laser driver. (b) Coarse characterization of the widely tunable laser showing the tuning range and super-modes. (c) TL FM response measurement setup and (d) the corresponding magnitude and phase responses with estimated phase cross-over frequency of 4.2 MHz.

Coarse tuning can thus be accomplished by changing the currents of the Bragg mirrors and/or phase section. Continuous tuning and sequential counting of comb teeth are essential for correct frequency synthesis; thus, during the coarse tuning, the TL must not experience any frequency jumps or mode hops as this will result in losing track of the current location of the TL with respect to the reference comb.

To identify the super-modes and study the tuning behavior of the TL for different phase and mirror current configurations, the TL was characterized. Fig. 2.5(a) shows the top level schematic of the circuit used to control and drive the TL. To tune the TL across a large wavelength range, first, the differential input (DF) is used to select a super-mode by changing the offset current between the cavity mirrors. Then, the common-mode (CM) input is adjusted to change the currents of both mirrors by the same amount to continuously tune the laser across the selected super-mode.

As part of the coarse characterization of the TL, using the common-mode and differential mode described above, the currents of the mirrors are swept in a nested loop and the emission wavelength of the TL is measured and recorded. Fig. 2.5(b) shows the super-modes and emission wavelengths of the TL sorted in ascending order. The horizontal axis shows the number of sweep points. Each sweep (characterization) point corresponds to a different combination of mirror currents.

The result of the TL coarse characterization can be used to form a look-up table that contains data points required to continuously sweep the TL across a desired wavelength range. The look-up table is stored in the memory of the microcontroller. Digital to analog converters set the CM, DF and phase values based on this look-up table and op-amp based drivers are used to drive the various sections of the TL.

Another important characteristic of the TL that should be studied, is the frequency modulation (FM) response of the laser. The tunable DBR laser used in this work does not have a separate wideband section for frequency tuning. Therefore, the gain section is used to perform phase locking. In this case, the resulting phase inversion in the laser FM response limits the loop bandwidth [31]. This is especially important since it limits the bandwidth within which the phase noise (linewidth) of the TL can reduced. Phase reversal is due to the fact that when the gain section of the TL is modulated with an electrical signal. At low modulation frequencies the corresponding change in the frequency of the TL is out of phase with the modulation signal. In other words, as the modulating signal (current) becomes larger, the laser goes towards lower frequencies (thermal red shift). At high modulation frequencies, it is in-phase with input signal (electronic blue shift). These two opposing mechanisms cause a phase reversal in the laser FM response, resulting in a large phase change in the loop response, which limits its operation bandwidth (this is discussed in Section 2.4). As shown in [31], the FM response of a semiconductor laser can be modeled as

$$F_{SCL}(f) = \frac{1}{b}\left(\frac{b - \sqrt{\frac{jf}{f_c}}}{1 + \sqrt{\frac{jf}{f_c}}} \right), \tag{2.1}$$

where f is the modulation frequency, and b and f_c are fitting parameters. Figure 2.5(c) shows the measurement setup for FM response characterization. Here, the gain section of the laser is being driven by port 1 of a vector network analyzer (VNA) and the output of the TL is connected to a frequency discriminator, comprised of a Mach-Zehnder interferometer followed by a photodiode. The output of the photodiode is amplified and connected to port 2 of the VNA. The resulting magnitude and phase responses are shown in Fig. 2.5(d). The magnitude and phase responses of (1) for $b = 2.9$ and $f_c = 4.2$ MHz are also shown in Fig. 2.5(d). As mentioned before, f_c (known as phase cross-over frequency), limits the effective loop bandwidth of the EOPLL. In this case, the bandwidth over which the loop is capable of performing phase noise reduction cannot be much larger than 4.2 MHz.

2.3 Coarse tuning and tooth indexing

As mentioned in Section 2.1.1, in order to perform optical frequency synthesis, during the coarse tuning phase, the TL is tuned to the vicinity of the desired comb tooth. In this case, it is necessary to tune the TL continuously (Section 2.2), and to keep track of the frequency of the TL with respect to the comb teeth at all times. Therefore, an indexing system is designed to count the number of passing comb teeth as the TL is being tuned.

Before discussing the design of the indexing system, the generation and the spectrum of the OFC should be considered. An OFC can be generated using different methods. In order to ultimately implement a fully integrated OFS, one needs to integrate the OFC, too. One way to do so is to use a mode-lock laser whose output consists of a train of very short pulses in time domain which corresponds to equidistant tones in frequency domain. In this method, by passing the output of a mode-locked laser through nonlinear a material, a wide octave-spanning optical spectrum, a.k.a. supercontinuum, is generated.

Then, in a second harmonic generation process, an OFC with twice the frequency of the original one is generated. Finally, using a carrier envelope offset locking method, the last and first comb lines of the first and second OFC are locked to each other, resulting a very stable reference comb. Also, the OFC repetition rate is locked to a clean microwave source [22,23]. In general, the reference OFC spectrum and its noise floor are not flat, *i.e.* the noise floor and the comb teeth power vary across the comb frequency range.

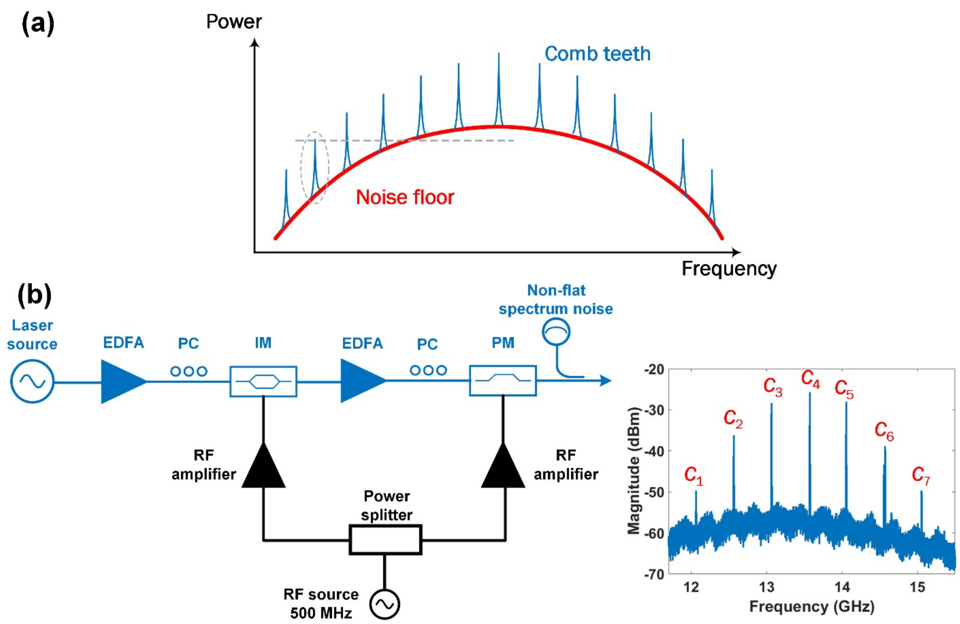

Figure 2.6 – (a) Typical spectrum of an OFC where the non-flat noise floor causes teeth power variation. (b) The setup to generate electro-optical OFC and the resulting spectrum.

This is illustrated in Fig 2.6(a). This in important characteristic that should be considered in designing an indexing system and will be discussed more. Here, in order to demonstrate optical synthesis using the proposed system, an electro-optic frequency comb is implemented. In this method, electro-optical modulation of light is used in order to introduce side-tones and generate comb teeth. As shown in Fig. 2.6(b), the output light of the laser source is first amplified using an erbium-doped fiber amplifier (EDFA) to achieve enough optical power for modulation. After passing through a polarization controller (PC), the light is modulated using an optical intensity modulator (IM).

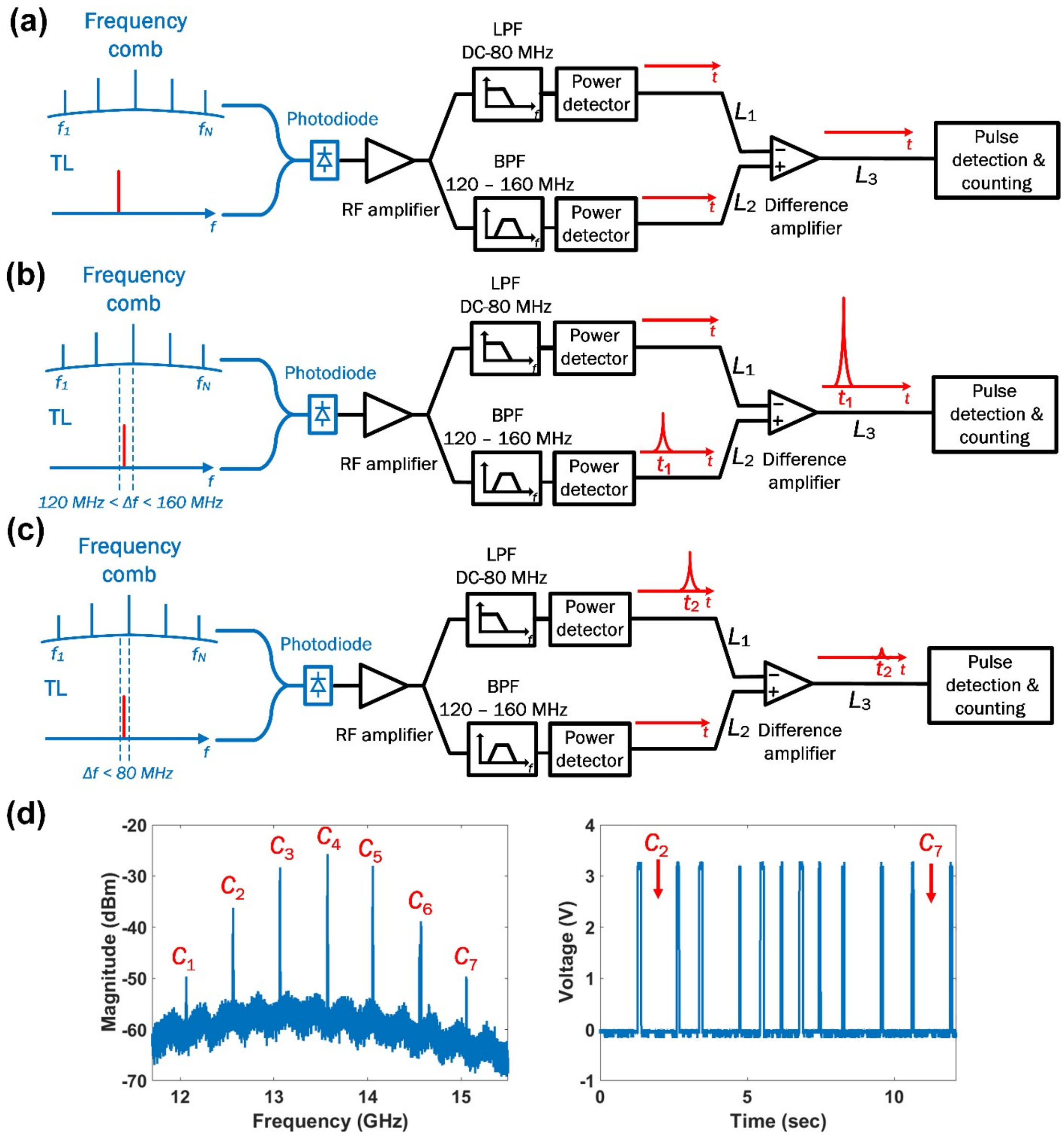

Figure 2.7 – Operation of the indexing system. (a) No signal is detected when the beat-note is outside the passband of the filters. (b) Bottom path detect the beat-note and a large signal appears at L_3. (c) Top path detects the beat-note but no signal appears at L_3. (d) The OFC spectrum and the detected pulses with two pulses per comb tooth.

To increase the number of teeth, a second stage of modulation is implemented using an optical phase modulator (PM). Finally, a wideband laser source whose spectrum is non-flat within the bandwidth of interest is added to the generated comb to imitate the spectrum of a typical integrated OFC. The resulting spectrum of the OFC is shown in Fig. 2.6(b) after frequency down-conversion. This OFC contains 7 teeth and is used for indexing system characterization.

The block diagram of the indexing system is shown in Fig. 2.7(a), where, the beat-note signal is detected by combining the TL output and the reference comb followed by photo-detection. As discussed before, the reference comb frequency spectrum and its noise floor are not flat. This may result in rather large beat-note SNR variations which makes it challenging to detect and count the comb teeth. In particular, often the local SNR may be large enough for detection, however, the noise floor around some comb teeth may be larger than the power of some other comb lines elsewhere within the comb spectrum. In this case, a single power threshold level would not work to detect all comb teeth. In the proposed architecture of Fig. 2.7(a), the beat-note power is compared with the local noise level using two parallel paths. In the top path, a power detector measures the power of the signal after a low-pass filter (LPF) with a corner frequency of 80 MHz. In the bottom path, the LPF is replaced by a band-pass filter (BPF) whose passband covers 120 MHz to 160 MHz and does not overlap with that of the LPF. Therefore, when the top path detects the power of the signal (Fig. 2.7(b)), the bottom path measures the local noise level. The same situation happens when the beat-note is within the passband of the BPF in the bottom path while the top path measures the local noise floor (Fig. 2.7(c)). The signal at the output of the bottom path is then subtracted from the output of the top path in a difference amplifier. In this case, transitions in the signal at the output of the difference amplifier (in form of a pulse train) correspond to passing comb teeth and can be used for tooth-indexing and counting

In Fig. 2.7, as the beat-note moves, two signals, L_1 and L_2, are generated in the top and bottom paths, respectively. When L_1 (L_2) is high at time t_1 (t_2), the signal power is measured in the top (bottom) path and the noise level is measured in the bottom (top) path. When L_2 is higher than L_1, a signal is generated at the output of the difference amplifier (L_3). Therefore, two pulses per comb tooth are generated at node L_3, one when the TL is on the left side of a specific comb tooth and one when it is on the right side. This is shown in Fig. 2.7(d) where each comb tooth falls between two pulses as the TL passes through the comb teeth.

While the TL is being continuously tuned, the microcontroller counts the number of pulses (corresponding to the number of passing teeth) and locates the TL frequency with respect to the reference comb teeth. After counting a desired number of comb teeth, the TL arrives in the vicinity of the target comb tooth and the microcontroller stops the coarse tuning. At this point, the EOPLL is engaged to perform phase locking followed by fine tuning, the process that is explained in details in the next section. Note that the proposed architecture of the indexing system is capable of detecting the beat-note with more than 25 dB SNR variations which is essential for the frequency synthesis process.

2.4 Fine tuning using the EOPLL chip and the AAS

EOPLL is the core of an optical synthesizer as it phase locks the TL to the reference and allows for fine tuning the frequency of TL with respect to the reference. EOPLLs have been studied and demonstrated using both bench-top [32-35] and partially integrated implementations [4,29]. Large phase locking bandwidth has been achieved for an EOPLL with electronic and photonic circuits implemented on two separate III-V platforms [36,37]. Integrated EOPLLs are especially important in implementation of integrated OFSs to ensure a stable phase-lock to the reference which is a function of total loop delay. In bench-top and partially integrated EOPLLs, large delays exist because of off-chip electrical and optical long routings. Therefore, it is very beneficial to have a fully integrated EOPLL in an OFS. The main challenge is the co-integration of electronic and photonic components on the same chip to minimize the loop delay.

Standard complementary metal oxide semiconductor (CMOS) Silicon on insulator (SOI) processes offer high degree of optical confinement, high fabrication yield, low-cost, scalability to large-volume production, and co-integration with sophisticated electronic circuits [26,38,39] and therefore are suitable candidates for EOPLL system integration at infrared regime.

In this section the demonstration of an EOPLL integrated on the GLOBALFOUNDRIES GF7RFSOI, a standard 180 nm CMOS-SOI process is presented. Different photonic devices were designed on GF7RFSOI process (without post-processing) that were co-integrated with standard electronic devices to realize a novel reconfigurable phase-frequency locking architecture suitable for phase locking many different types of tunable lasers in the 1510 nm - 1590 nm wavelength range. Furthermore, co-integration of electronic and photonic devices on the same chip reduces the on-chip loop delay which significantly improves the EOPLL stability compared to bench-top and partially integrated implementations. By using the proposed architecture, the EOPLL acquisition and tracking ranges are significantly improved and the tunable laser can be continuously tuned while maintaining phase lock which is a key feature for reliable optical synthesis.

2.4.1 EOPLL nonlinear theory if operation

The frequency of a semiconductor laser can be tuned by changing its gain section bias current and therefore it can be modelled as a current controlled oscillator (CCO) [18]. This was illustrated in Fig. 2.2 and is repeated in Fig. 2.8(a). As discussed earlier, a change of i_c(t) in the laser bias current results in a change of $K_{laser}\int i_c(t)dt$ in the instantaneous phase of the laser electric field, where K_{laser} is the laser current to frequency conversion gain. Also, the photo-current is written as $i(t) = R\left[P_1 + P_2 + 2\sqrt{P_1P_2}\cos\left(\Phi_1 - \Phi_2\right)\right]$, where R, P_1, P_2, Φ_1 and Φ_2 are the photodiode responsivity, the optical power of the first and second lasers, and the instantaneous phase of the first and second lasers, respectively. Using this optical phase detector a semiconductor laser can be phase locked to a reference laser. The conceptual block diagram of an electro-optical phase locked loop (EOPLL) in the phase domain is depicted in Fig. 2.8(c) where $\Phi_i = \omega_i t$, Φ_o and $\Phi_e = \Phi_i - \Phi_o$ are the input phase, the output phase, and the phase error, respectively. Also, $f_{PD}(.)$, $f_{Loop}(t)$, and t_d are the non-linear impulse response of the phase detector, the loop filter impulse response, and the loop propagation delay, respectively. In addition, ω_i and ω_o are the reference laser frequency and the free-running frequency of the TL, respectively.

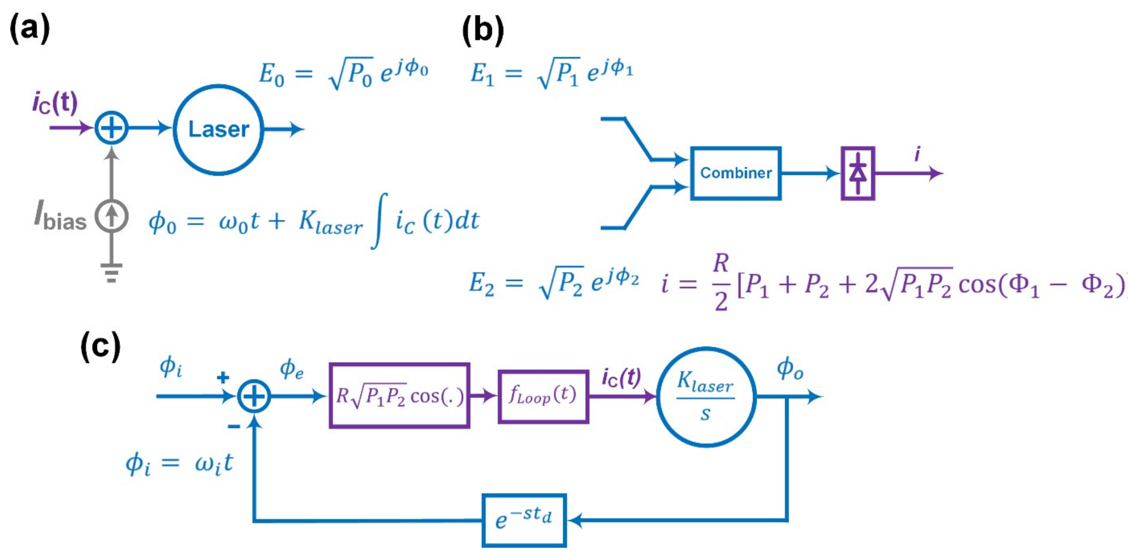

Figure 2.8 – The EOPLL principle of operation. (a) The semiconductor laser modelled as a current controlled oscillator, (b) an optical phase detector, and (c) the conceptual block diagram of an EOPLL in presence of loop delay.

The non-linear delay differential equation associated with the EOPLL in Fig. 2.8(c) is written as

$$\frac{d\Phi_e(t)}{dt} + K\cos\left(\Phi_e(t)\right) * f_{Loop}(t) * \delta(t - t_d) = \Delta\omega. \tag{2.2}$$

where $\Delta\omega = \omega_i - \omega_o$ and $K = 2\sqrt{P_1 P_2} K_{laser}$ are the difference between the reference laser frequency and the TL free-running frequency and the loop gain, respectively. Also, "*" denotes convolution. For the first order loop, no loop filter is placed in the PLL, that is, $f_{Loop}(t)$ is replaced by $\delta(t)$ where $\delta(.)$ is the Dirac delta function. In this case Eq. (2.2) is modified to

$$\frac{d\Phi_e(t)}{dt} + K\cos\left(\Phi_e(t-t_d)\right) = \Delta\omega. \tag{2.3}$$

To study the effect of the loop delay on the loop stability, perturbation theory can be used [40]. Consider the case that the phase error, Φ_e is perturbed around its steady state. In this case, the phase error can be written as $\Phi_e = \Phi_{e,ss} + \delta\Phi_e$ where $\Phi_{e,ss}$ is the steady state phase error and $\delta\Phi_e$ is the perturbation. Equation (2.3) is then modified to:

$$\frac{d\delta\Phi_e(t)}{dt} + K\cos\left(\Phi_{e,ss} + \delta\Phi_e(t-t_d)\right) = \Delta\omega. \tag{2.4}$$

Since the perturbation is by definition small, the cosine term in Eq. (2.4) can be simplified as

$$\begin{aligned}
&\cos\left(\Phi_{e,ss} + \delta\Phi_e(t-t_d)\right) = \\
&\cos\left(\Phi_{e,ss}\right)\cos\left(\delta\Phi_e(t-t_d)\right) - \sin\left(\Phi_{e,ss}\right)\sin\left(\delta\Phi_e(t-t_d)\right) \\
&\approx \cos\left(\Phi_{e,ss}\right) - \delta\Phi_e(t-t_d)\sin\left(\Phi_{e,ss}\right).
\end{aligned} \tag{2.5}$$

Also, under steady state condition, $\frac{d\Phi_{e,ss}(t)}{dt} = 0$ and Eq. (2.4) results in

$$\sin(\Phi_{e,ss}) = \pm\sqrt{1-(\frac{\Delta\omega}{K})^2}. \quad (2.6)$$

Using Eqs. (2.5) and (2.6), Eq. (2.4) is modified to

$$\frac{d\delta\Phi_e(t)}{dt} + K\left(\frac{\Delta\omega}{K} \mp \delta\Phi_e(t-t_d)\sqrt{1-\left(\frac{\Delta\omega}{K}\right)^2}\right) = \Delta\omega. \quad (2.7)$$

The characteristic equation for Eq. (2.7) is written as $s = \pm\sqrt{K^2 - \Delta\omega^2}(e^{-st_d})$. Multiplying both sides of this equation by $t_d e^{st_d}$ results in

$$st_d e^{st_d} = \pm t_d\sqrt{K^2 - \Delta\omega^2}. \quad (2.8)$$

The solution to Eq. (2.8) can be written in terms of complex Lambert function [41] as

$$st_d = W\left(\pm t_d\sqrt{K^2 - \Delta\omega^2}\right). \quad (2.9)$$

where $W(.)$ represents the complex Lambert function that satisfies $W(z)e^{W(z)} = z$. The EOPLL described by Eq. (2.3) is stable if the real part of the solution to the characteristic equation is negative which requires $W\left(\pm t_d\sqrt{K^2 - \Delta\omega^2}\right) < 0$. For the complex Lambert function, $W(z)$, the real part of W is non-positive only if $-\pi/2 \le z \le 0$ [27], resulting in stability condition as

$$0 \le K \le \frac{\pi}{2t_d}\sqrt{1+\left(\frac{2t_d\Delta\omega}{\pi}\right)^2}. \quad (2.10)$$

Equation (2.10) shows that the maximum stable loop gain is inversely proportional to the loop delay. Since the tracking and acquisition ranges of a PLL are directly proportional to the loop gain [40], the loop delay limits the tracking and acquisition ranges.

Most practical phase locked loops can be modelled as a second order loop [40] where $f_{Loop}(t)$ represents a non-zero pole in the loop transfer function. In this case, the non-linear delay differential equation of the EOPLL, Eq. (2.2), is written as

$$a\frac{d^2\Phi_e(t)}{dt^2}+\frac{d\Phi_e(t)}{dt}+K\cos\left(\Phi_e(t-t_d)\right)=\Delta\omega. \tag{2.11}$$

where $f_{Loop}(t)=e^{-at}u(t)$, corresponding to a pole at $\omega_p=-1/a$, is considered and $u(t)$ represents the step function. Perturbing the phase error around the steady state point results in the characteristic equation for Eq. (2.11) as

$$\frac{d^2\delta\Phi_e(t)}{dt^2}+\frac{1}{a}\frac{d\delta\Phi_e(t)}{dt}\pm\frac{K}{a}\sqrt{1-\left(\frac{\Delta\omega}{K}\right)^2}\,\delta\Phi_e(t-t_d)=0. \tag{2.12}$$

Equation (2.12) is a linear delay differential equation known as the Lienard equation [42]. The Lienard delay differential equation $d^2x/dt^2+A\left(dx/dt\right)+Bx(t-t_d)=0$ represents a stable system if for $A,B>0$, $Bx^2(Bt_d-A)<0$ is satisfied [27,42]. Therefore, the second order EOPLL is stable if

$$K<\frac{1}{t_d}\sqrt{1+\left(\Delta\omega t_d\right)^2}. \tag{2.13}$$

Equation (2.13) shows that similar to the first order EOPLL, the maximum stable loop gain of a second order EOPLL is inversely proportional to the loop delay and hence is significantly improved with system integration.

2.4.2 Theory of heterodyne EOPLL

The EOPLL shown in Fig. 2.8(c) is a homodyne phase locked loop. In this case, under the lock condition, the electronic signal within the loop would be at DC. Therefore, the homodyne EOPLL suffers from the effect of the flicker noise of the electronic components. In addition, all electronic components must be able to operate at DC. Moreover, it is essential that the EOPLL can be used for fine tuning the TL frequency. An alternative to the homodyne EOPLL is the heterodyne configuration, which can address the aforementioned challenges. The block diagram of a heterodyne EOPLL is depicted in Fig. 2.9(a). This is a more complete version of the block diagram shown in Fig. 2.3(d). Assuming the electric field of the tunable and reference lasers to be $E_{TL} = \sqrt{P_{TL}} e^{j(\omega_{TL} t + \phi_{TL})}$ and $E_{Ref} = \sqrt{P_{Ref}} e^{j(\omega_{Ref} t + \phi_{Ref})}$, the photocurrent corresponding to the beat-note of the two lasers is written as

$$i_{PD}(t) = R\left(P_{TL} + P_{Ref}\right) + 2R\sqrt{P_{TL} P_{Ref}} \cos\left(\left(\omega_{TL} - \omega_{Ref}\right) t + \phi_{TL} - \phi_{Ref}\right), \qquad (2.14)$$

where $i_{PD}, P_{TL}, P_{Ref}, \omega_{TL}, \omega_{Ref}, \phi_{TL}, \phi_{Ref}$, and R are the photocurrent, the TL power, the reference laser power, the TL frequency, the reference laser frequency, the phase of the TL, the phase of reference laser, and the photodiode responsivity, respectively.

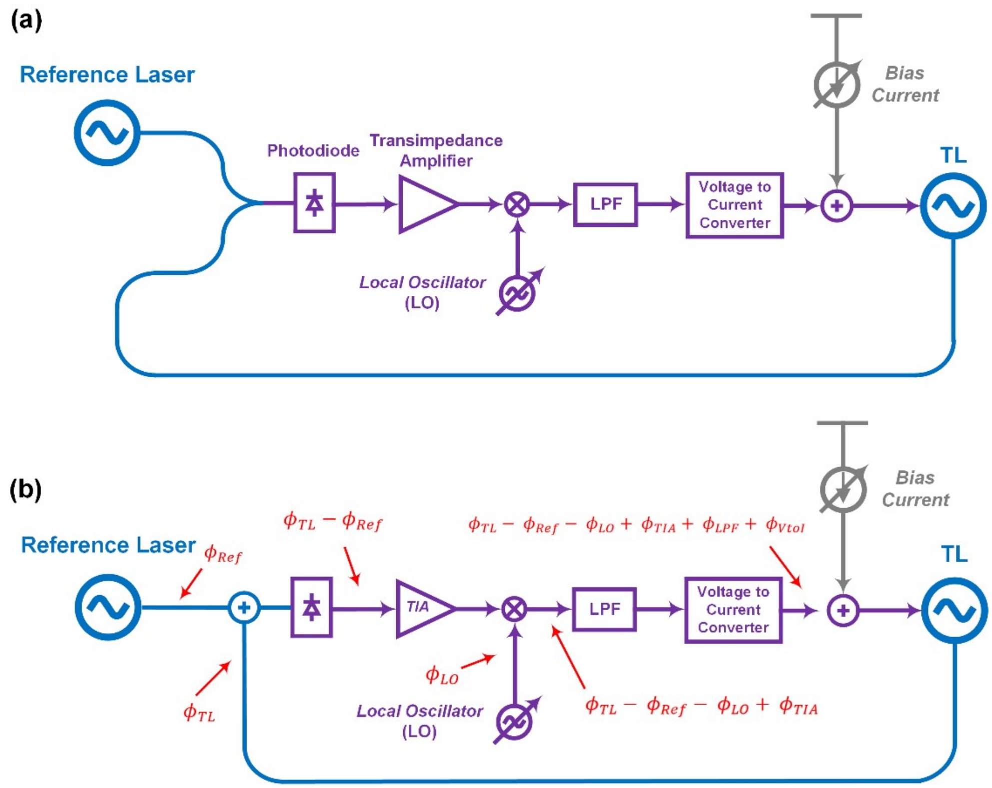

Figure 2.9 – (a) Conceptual block diagram of a heterodyne electro-optical phase-locked loop. (b) Phase adjustment mechanism in EOPLL.

The photocurrent is amplified and converted to a voltage using a band-pass trans-impedance amplifier (TIA). The TIA output voltage is written as

$$v_{TIA}(t) = 2K_{TIA}R\sqrt{P_{TL}P_{Ref}}\cos\left(\left(\omega_{TL} - \omega_{Ref}\right)t + \phi_{TL} - \phi_{Ref} + \phi_{TIA}\right), \tag{2.15}$$

where K_{TIA} and ϕ_{TIA} are the TIA gain and phase responses, respectively. The TIA output voltage is mixed with the heterodyning LO signal, low-pass filtered, and converted to a control current using a voltage-to-current converter (VtoI). The VtoI output, the control current, can be written as

$$i_c(t) = K\cos\Big(\big(\omega_{TL} - \omega_{Ref} - \omega_{LO}\big)t + \phi_{TL} - \phi_{Ref} - \phi_{LO} + \phi_{TIA} + \phi_{LPF} + \phi_{VtoI}\Big), \qquad (2.16)$$

where $K = K_{VtoI}K_{LPF}K_{Mixer}K_{TIA}R\sqrt{P_{TL}P_{Ref}}$, K_{VtoI}, K_{LPF}, K_{Mixer}, ϕ_{LO}, ϕ_{LPF} and ϕ_{VtoI} are electronic gain, the VtoI gain, the low-pass-filter amplitude response, the mixer conversion gain, the phase of the heterodyning signal, the low-pass-filter (LPF) phase response, and the VtoI converter phase response, respectively (Fig. 2.9(b)). The control current is injected to the TL to close the loop. Under the lock condition, the control current is at DC. Therefore, $\omega_{TL} - \omega_{Ref} = \omega_{LO}$, which indicates the frequency difference between the reference and the TL, can be adjusted by tuning the heterodyning signal. This is a key feature in operation of an optical synthesizer since for a stable frequency comb as the reference, the TL can be tuned with a fine resolution by tuning the synthesized heterodyning source. Also, under the lock condition, the phase of the control current is constant which considering that the phase responses of the TIA, LPF, and VtoI are constant results in

$$\phi_{TL} - \phi_{Ref} - \phi_{LO} = const. \qquad (2.17)$$

Equation (2.17) shows that the relative phase between the reference laser and the TL can be accurately adjusted by changing the phase of the heterodyning source in the electrical domain.

2.4.3 Integrated EOPLL system architecture and characterization

Figure 2.10(a) shows the schematic of the integrated EOPLL. Both reference laser and TL are coupled into the chip using grating couplers (GC), guided using nanophotonic waveguides, and combined using a Y-junction. The Y-junction output is then backside coupled to a vertical InGaAs photodiode using a grating coupler. The output of the photodiode is wire-bonded to the input of the electronic circuit for further processing.

The output of the chip is fed back to the laser to close the loop. In this case, on-chip optical and electrical interconnects reduce the total loop delay. The analysis presented in Section 2.4.1 shows that the maximum stable loop gain is inversely proportional to the loop delay. Therefore, compared to bench-top implementations, integrated implementations can significantly improve the EOPLL stability.

Figure 2.10(b) shows the microphotograph of the electronic-photonic chip integrated on GF7RFSOI process with the photodiode mounted on top. The photonic test structures used for device characterization are depicted in Fig. 2.10(c).

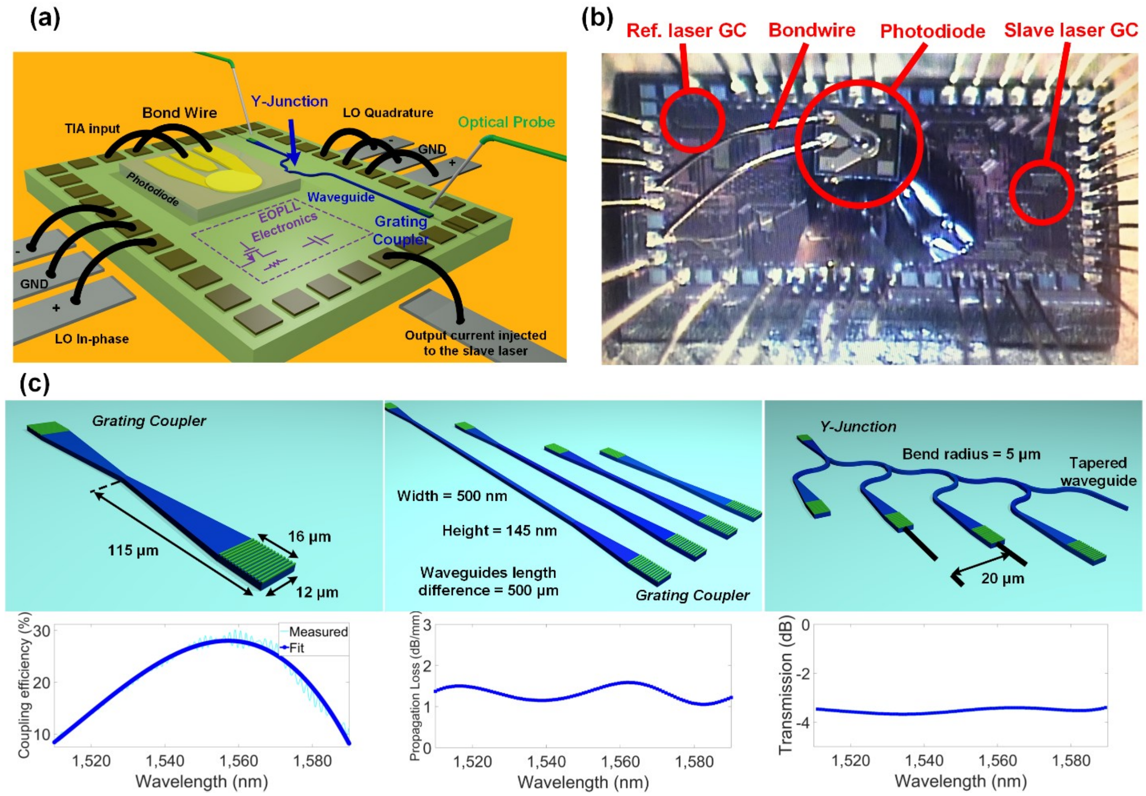

Figure 2.10 – (a) Schematic of the EOPLL chip. (b) The EOPLL chip microphotograph. (c) Characterization results of the implemented on-chip photonic devices. Peak GC efficieny happens at 1560 nm and coupling angle of 17°. The Y-junction has an excess loss of 0.5 dB.

At 1550 nm, the measured grating coupler efficiency, the nanophotonic average waveguide loss, and the Y-junction excess loss are 27%, 1.3 dB/mm, and 0.5 dB, respectively. Note that while many photonic devices have been successfully implemented on GF7RFSOI process, a wide band photodiode with high responsivity cannot be implemented since no material with efficient absorption coefficient at 1550 nm (*e.g.* Ge) is available in this standard electronic process.

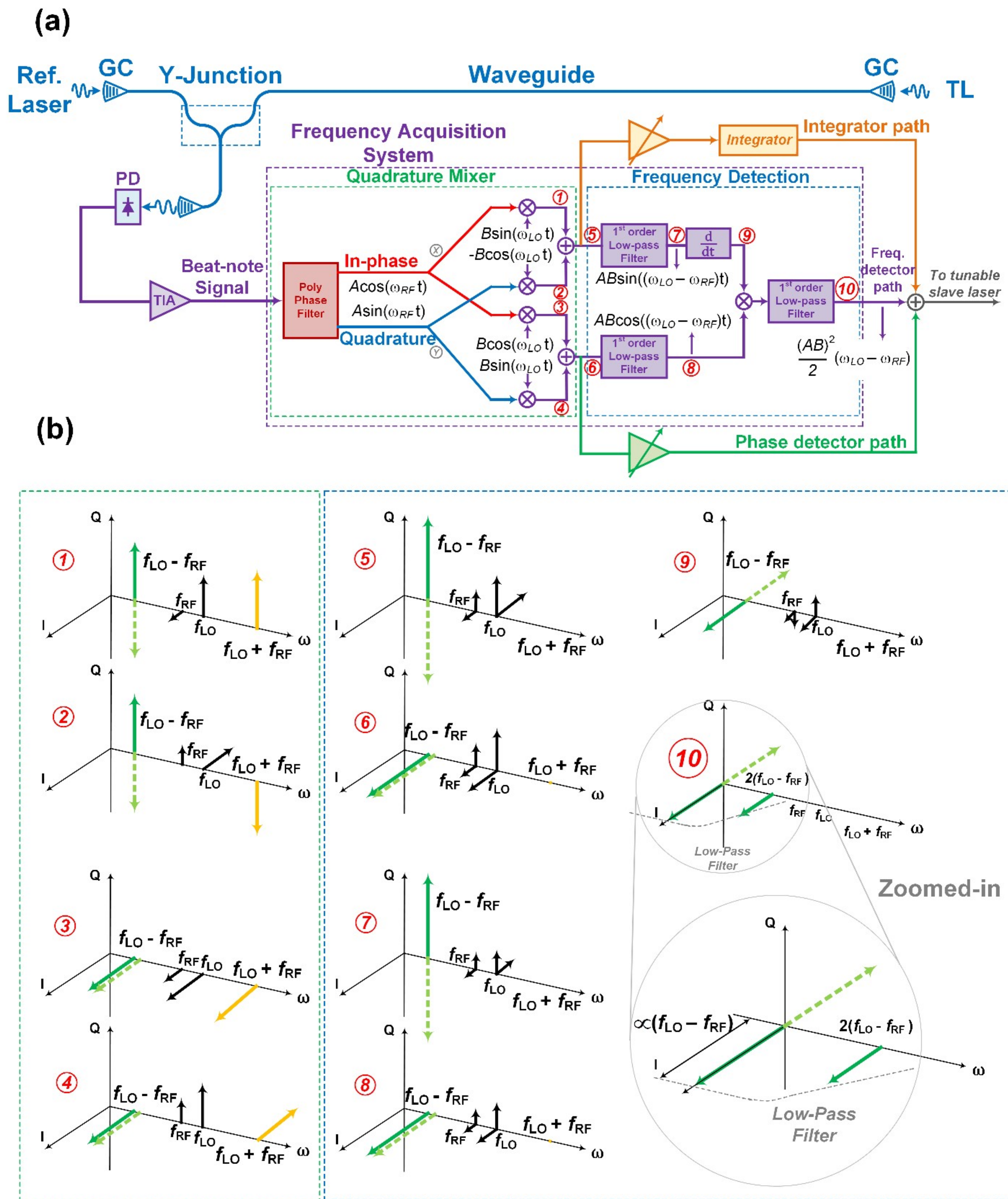

Figure 2.11 – The block diagram of the EOPLL and frequency acquisition principle of operation. (a) Block diagram of the EOPLL chip. (b) Frequency detection principle of operation in the complex frequency plane is shown. Each diagram shows the frequency spectrum of the corresponding node in Fig. 2.11(a). “I” and “Q” represent cosine and sine functions, respectively.

Figure 2.11(a) shows the block diagram of the EOPLL. The two lasers are coupled into the SOI chip, combined using a Y-junction, and photo-detected. The photocurrent, which is the beat note between the reference and the TL, is a sinusoidal signal containing the instantaneous phase difference between the lasers and flows back to the SOI chip using bond wires. This photocurrent is amplified and converted to a voltage using a trans-impedance amplifier (TIA). A poly-phase filter [43] is used to convert the TIA output voltage, the beat-note signal at frequency f_{RF}, to two signals with 90° phase difference (referred to as the quadrature signals). Four active mixers are used to perform quadrature mixing of the poly-phase filter output and the differential quadrature signals generated from the off-chip LO heterodyning signal at frequency f_{LO}. The quadrature mixer output is used in three different paths; the frequency detection path, the phase detection path, and the integration path. Figure 2.11(b) illustrates the frequency detection principle of operation in a complex frequency plane. Note that the imaginary plane is rotated by 90° with respect to the real plane to ease the illustration.

The beat-note signal at the output of the TIA follows Eq. (2.15). A poly-phase filter is placed after the TIA to generate two signals with 90° phase difference as

$$V_x = A\cos\left(\omega_{RF}t + \phi_{RF}\right) \text{ and } V_y = A\sin\left(\omega_{RF}t + \phi_{RF}\right), \tag{2.18}$$

where $A = 2K_{poly}K_{TIA}R\sqrt{P_{TL}P_{Ref}}, \omega_{RF} = \omega_{TL} - \omega_{Ref}, \phi_{RF} = \phi_{TL} - \phi_{Ref} + \phi_{TIA} + \phi_{poly}, K_{poly}$, and ϕ_{poly} are the amplitude of the signal at the poly-phase filter output, the beat-note frequency, the phase of the signal after the poly-phase filter, the poly-phase filter insertion loss, and the poly-phase filter phase response, respectively. The signals at nodes X and Y are mixed with the differential quadrature signals generated from the heterodyning synthesized source. In this case, the signals at nodes 1, 2, 3, and 4 are written as

$$V_1 = \frac{AB}{2}\left[\sin\left((\omega_{LO}+\omega_{RF})t+\phi_{LO}+\phi_{RF}\right)+\sin\left((\omega_{LO}-\omega_{RF})t+\phi_{LO}-\phi_{RF}\right)\right], \tag{2.19}$$

$$V_2 = \frac{AB}{2}\left[-\sin\left((\omega_{LO}+\omega_{RF})t+\phi_{LO}+\phi_{RF}\right)+\sin\left((\omega_{LO}-\omega_{RF})t+\phi_{LO}-\phi_{RF}\right)\right], \tag{2.20}$$

$$V_3 = \frac{AB}{2}\left[\cos\left((\omega_{LO}+\omega_{RF})t+\phi_{LO}+\phi_{RF}\right)+\cos\left((\omega_{LO}-\omega_{RF})t+\phi_{LO}-\phi_{RF}\right)\right], \tag{2.21}$$

$$V_4 = \frac{AB}{2}\left[-\cos\left((\omega_{LO}+\omega_{RF})t+\phi_{LO}+\phi_{RF}\right)+\cos\left((\omega_{LO}-\omega_{RF})t+\phi_{LO}-\phi_{RF}\right)\right], \tag{2.22}$$

where B, ω_{LO}, and ϕ_{LO} are the amplitude, frequency, and phase of the heterodyning signals, respectively. The signals at nodes 1 and 2 are added to reject the upper side-band at $f_{RF} + f_{LO}$. A low-pass filter is used to attenuate the leakage signals at f_{RF} and f_{LO}. In this case, the signal at node 7 is written as

$$V_7 = AB\left[\sin\left((\omega_{LO}-\omega_{RF})t+\phi_{LO}-\phi_{RF}\right)\right], \tag{2.23}$$

Similarly, the signal at node 8 is written as

$$V_8 = AB\left[\cos\left((\omega_{LO}-\omega_{RF})t+\phi_{LO}-\phi_{RF}\right)\right], \tag{2.24}$$

Differentiating the signal at 7 with respect to time results in the signal at node 9 as

$$V_9 = AB(\omega_{LO} - \omega_{RF})\left[\cos\left((\omega_{LO} - \omega_{RF})t + \phi_{LO} - \phi_{RF}\right)\right], \tag{2.25}$$

Multiplying the signals at nodes 8 and 9 followed by low-pass filtering (integration) results in a DC term at node 10 as

$$V_{10} = \frac{(AB)^2}{2}(\omega_{LO} - \omega_{RF}). \tag{2.26}$$

Equation (2.26) shows that the DC voltage at node 10 is linearly proportional to the difference between the beat-note frequency and the LO frequency. The signal at node 10 is applied to the TL gain section to offset frequency lock it to the reference laser. The frequency locking does not interfere with the phase locking process as under the phase lock condition $(\omega_{LO} = \omega_{RF})$, the DC voltage at node 10 is zero.

Note that if the upper sideband at $f_{RF} + f_{LO}$ appears at nodes 6 or 7, it can desensitize the frequency detection resulting in a false DC voltage detected at node 10. Therefore, the upper side-band must be sufficiently attenuated. Using a high order low-pass filter to attenuate the upper side-band can significantly increase the loop delay resulting in instability. As an alternative to the high order low-pass filter, the reported quadrature mixing scheme rejects the upper side-band without introducing excess delay and hence does not affect the loop stability

The phase detection path is used to phase lock the TL to the reference laser. In this case, the signal at node (6) which is proportional to the instantaneous phase difference between the beat-note and the heterodyning LO signal is used for phase locking. Under the lock condition, the phase and frequency difference between the reference and slave lasers are set by the phase and the frequency of the LO heterodyning signal.

The integrator path increases the loop gain at low frequencies and hence increases the tracking range [40]. The signal at node (5) is amplified, integrated, and combined with the outputs of the frequency detection and the phase detection paths and is injected to the laser. The gain and bandwidth of all three paths can be adjusted to enable phase and frequency locking of various TLs with different characteristics.

The electronic circuit schematic of various blocks of the EOPLL is shown in Fig. 2.12. The TIA is designed based on a regulated cascade architecture as the input stage followed by a buffer stage. The output of the buffer (S+ and S-) are connected to a differential amplifier followed by another buffer to further increase the gain, providing 0 to 69 dBΩ gain and 3-dB bandwidth of 4.5 GHz. The quadrature mixers are double balanced Gilbert cells with gain of 16 dB and measured 3-dB bandwidth of 9 GHz. The poly phase filter is a 7-stage RC network with 3-dB bandwidth of 5.5 GHz. The frequency detection amplifier has 42 dB voltage gain and is followed by a 300/600 kHz low-pass filter as an integrator. The phase detection amplifier has measured voltage gain of 20 dB and its bandwidth can be selected in the range of 12~50 MHz which is useful when different lasers with different FM responses are used as slave lasers. The amplifier in the integrator path has measured voltage gain of 19.5 dB and is followed by a 300/600 kHz low-pass filter as an integrator. The entire chip consumes 19 mA from a 1.5 V supply voltage.

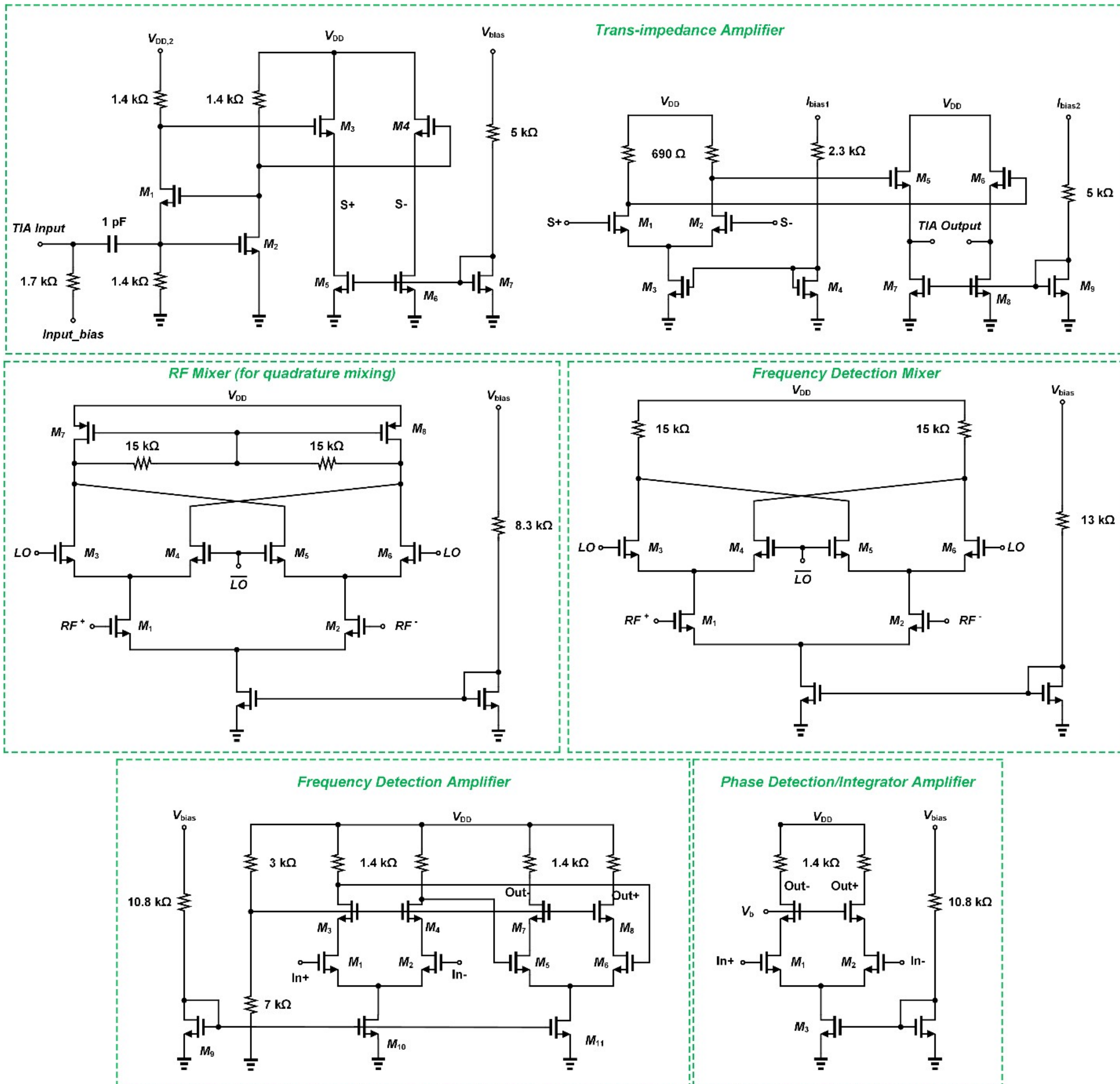

Figure 2.12 – Electronic circuitry used for different blocks of the EOPLL chip.

To characterize the EOPLL performance, first the frequency detection path is characterized. This is important since it defines the acquisition range of the EOPLL which is essential for fine tuning in synthesis process. As explained before, frequency detection relies on quadrature RF and LO signal generation. Hence, amplitude and phase mismatch between these quadrature signals can affect the frequency locking performance. Figures 2.13(a) and 2.13(b) show the measured amplitude and phase mismatch between the signals at nodes (5) and (6) in Fig. 2.11(a), respectively. Figure 2.13(c) shows the measured characteristics of the frequency detection path versus simulation result for the case that the LO frequency is set to 900 MHz. When the beat-note frequency, f_{RF}, is larger (smaller) than the heterodyning frequency, f_{LO}, a positive (negative) voltage is generated at node (10) tuning the slave tunable laser such that f_{RF} moves towards f_{LO} leading to frequency locking. When the beat-note frequency is within the EOPLL phase acquisition range, the phase detection path performs phase locking. At his point, the voltage at node (10) is zero ($f_{RF} \approx f_{LO}$) and the frequency locked loop is disengaged. The figure shows the measured amplitude mismatch of under 2.5% and phase mismatch of under 5° at the output of the quadrature mixer stage.

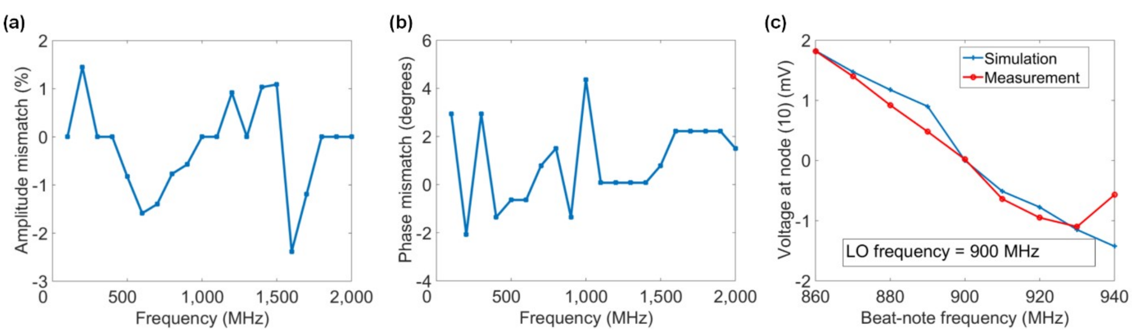

Figure 2.13 – Measured (a) amplitude and (b) phase mismatch at the output of quadrature mixers (nodes (5) and (6) in Fig. 2.11(a)). (c) The measured characteristics of the frequency detection path when the frequency of the heterodyning signal is set to 900 MHz.

The full EOPLL characterization setup is shown in Fig. 2.14(a). The reference laser optical power is set to 5 dBm and is delivered to the chip using an optical fiber.

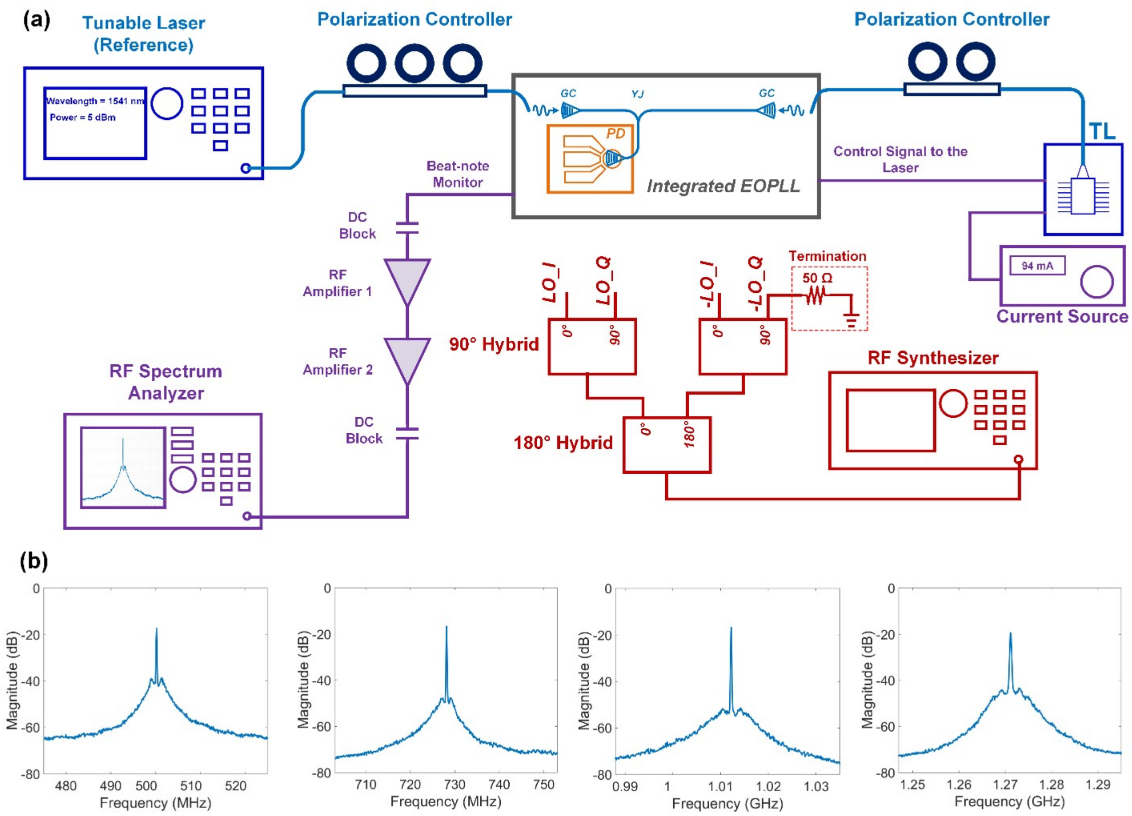

Figure 2.14 – (a) Measurement setup for characterization of the EOPLL chip. (b) Beat-note lock spectrum for different LO frequencies.

Note that the output of a laser chip can also be directly coupled to the EOPLL chip via the grating coupler. A low-noise current source is used to bias an ACATEL 3CN00325CW distributed feedback (DFB) laser as the TL to minimize the effect of the noise of the laser driver on the laser linewidth. The bias current of the slave tunable laser is set to 94 mA which is provided by a Thorlabs LDC201U laser driver. Note that the noise of the laser driver is directly injected to the TL increasing its linewidth and reducing the PL-FOM. In this case, the linewidth of the laser would be closer to the phase reversal frequency in the FM response which lowers the selectivity required for phase locking. The full-width at half-maximum linewidth of the TL when driven by the

Thorlabs LDC201U current source (at 94 mA) is approximately 650 kHz. The phase reversal frequency in the TL FM response occurs at 800 kHz. Therefore, the PL-FOM defined in the main text can be calculated to be 1.23. Based on phase locking performance of several commercially available semiconductor lasers it seems that PL-FOM > 1 results in robust phase locking.

A monitoring pad at the output of the photodiode has been wire-bonded and used to monitor the beat-note lock spectrum on a RF spectrum analyzer. To provide the heterodyning signal to the chip an Anritsu MG3696A frequency synthesizer has been used followed by a 180° hybrid and two 90° hybrids. The delivered RF power of the differential quadrature signals required for on-chip quadrature mixing is about 4 dBm. To monitor the lock spectrum, the beat-note after the photodiode is monitored using HP 8565E spectrum analyzer. The spectrum analyzer span is set to 50 MHz, the resolution and video bandwidths are set to 30 kHz and 10 kHz, respectively.

The total estimated on-chip propagation delay due to optical waveguides is under 30 ps. The estimated propagation delay due to optical and electrical interconnects between the EOPLL chip and the slave laser is under 2 ns. Figures 2.14(b) shows the lock spectrums (the beat-note) for different heterodyning LO frequencies confirming that the reported integrated EOPLL can acquire phase and frequency lock over a large range of heterodyning signal frequency.

2.4.4 Aided acquisition system

In order to further enhance the acquisition range of the EOPLL to be sufficient to cover the reference comb tooth-spacing, an aided acquisition system (AAS) is implemented. The block diagram of the AAS is shown in Fig. 2.15(a). The AAS system architecture is inspired by the frequency acquisition system reported in [29], however, it has been designed for a wideband operation such that the LO heterodyning signal can be tuned over 500 MHz while maintaining phase lock which is crucial for optical synthesis.

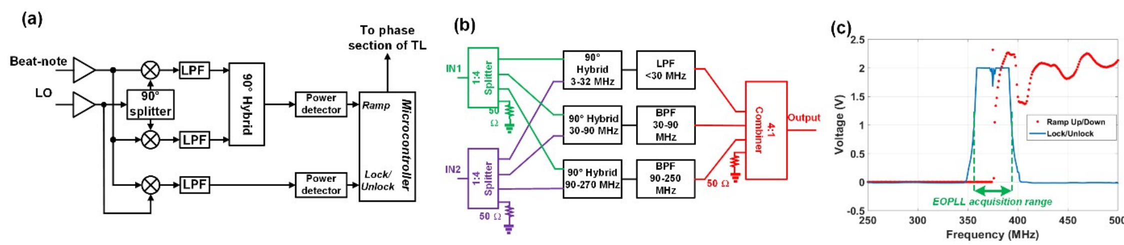

Figure 2.15 – (a) Block diagram of the aided acquisition system. (b) Block diagram of the implemented 90° hybrid in AAS system. (c) Lock detector response measured for LO frequency of 375 MHz.

The AAS consists of two paths: a lock indicator and a ramp generator path. In the ramp generator path, the system first detects the frequencies of the beat-note signal (f_{RF}) and the heterodyning LO signal (f_{LO}). Depending on whether $f_{RF} > f_{LO}$ or $f_{RF} < f_{LO}$, a high or low dc voltage is generated. A microcontroller reads this dc voltage and instructs a digital to analog converter to generate an upward or downward sloping ramp signal. This signal is injected to the phase section of the TL in order to shift the TL wavelength such that the beat-note frequency moves towards the LO frequency. The lock indicator path determines if the beat-note is within the acquisition range of the EOPLL. To do so, the beat-note and the LO signals are mixed. The mixer output, corresponding to the frequency difference between the beat-note and the LO signal, is low pass filtered and power detected. The low-pass filter corner frequency is set to be slightly smaller than the acquisition range of the EOPLL. If the frequency difference is within the bandwidth of the filter, the output of the power detector will be high indicating that the beat-note is close enough to the LO frequency such that the EOPLL can acquire phase lock. In this scenario, the microcontroller monitoring the output of the lock detector disengages the aided acquisition loop to avoid interfering with the EOPLL operation. If the frequency difference is outside the bandwidth of the low-pass filter, the lock detector output is low and the ramp generator is engaged.

A key component of the AAS system is the 90° hybrid in the image reject architecture in Fig. 2.15(a). This hybrid needs to operate from low enough frequencies (overlapping with EOPLL acquisition range), to 250 MHz (determined by the comb spacing). Fig. 2.15(b) shows the schematic of the 90° hybrid. To achieve a large image rejection over the desired wide frequency band, the frequency range of interest is divided into 3 sub-bands. After power splitting, in each sub-band, the quadrature signal is generated using a lower bandwidth hybrid. The outputs of these 3 hybrids are combined after band select filtering to achieve the functionality of the desired wideband 90° hybrid.

In order to characterize the AAS, two RF synthesized sources, one emulating the beat-note and the other one as the LO signal, are used. When the beat-note frequency is changed with respect to the LO frequency, the outputs of the lock indicator and the ramp generator are measured. In Fig. 2.15(c), LO frequency is set to 375 MHz and beat-note frequency is changed from 250 to 500 MHz. As a result, the ramp up/down changes from close to 0 V to more than 1 V depending on the sign of $f_{RF} - f_{LO}$. Furthermore, if f_{RF} is within ±20 MHz of f_{LO}, the lock indicator signal changes from close to 0 V (corresponding to the "Unlocked" state) to about 2 V (corresponding to the "Locked" state). In addition to enhancing the acquisition range of the EOPLL, the AAS resolves the issue of the false locking and compensates for the effect of slow laser temperature stabilization process (both will be discussed in detail in Section 2.5).

2.5 OFS design challenges

2.5.1 False locking

As discussed in Section 2.4, the integrated heterodyne EOPLL, as the core of the optical synthesizer, enables high resolution fine tuning through the adjustment of the frequency (and phase) of the heterodyning local oscillator. While the control of the optical phase and frequency using the RF heterodyning signal is a significant advantage, it poses the challenge of false locking.

Consider the block diagram of a heterodyne EOPLL in phase domain depicted in Fig. 2.16(a), where the frequency of the signals at different nodes are shown. Here, ω_{ref}, ω_{TL}, ω_{LO}, and ϕ_e are the reference laser frequency, the tunable laser frequency, the heterodyning LO frequency, and the phase error signal, respectively.

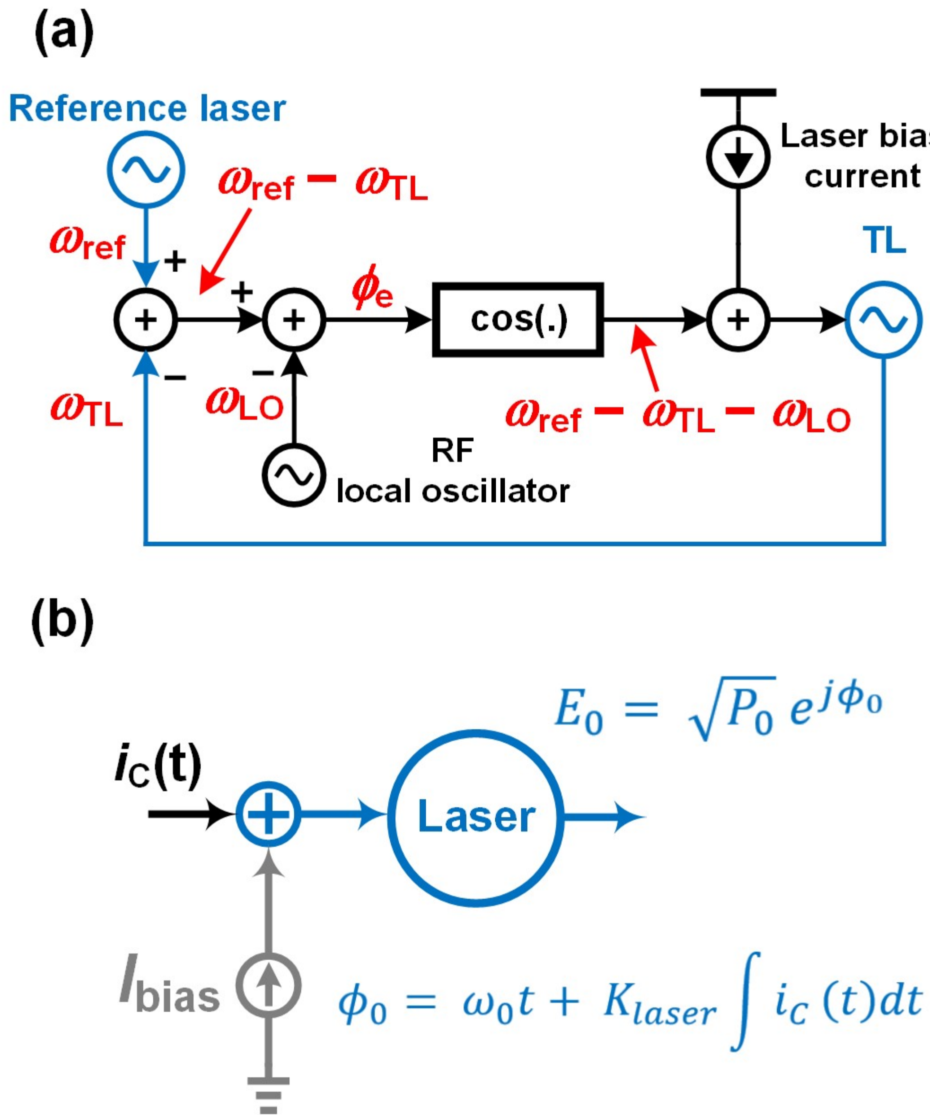

Figure 2.16 – (a) Block diagram of a heterodyne EOPLL in the phase domain. (b) Conceptual block diagram of a tunable laser as a current-controlled oscillator.

As shown in Fig. 2.16(b), the laser can be modeled as a current-controlled oscillator for which the oscillation frequency is determined by the current injected to its gain section. For this case, the non-linear differential equation of the EOPLL can be written as [27,40]

$$\frac{d\phi_e(t)}{dt} + K\cos(\phi_e(t)) = \Delta\omega \pm \omega_{LO} \tag{2.27}$$

where K is the loop gain in rad/sec (representing the product of the phase detector gain, the gain of the electronics, and the gain of the laser), and $\Delta\omega = \omega_{ref} - \omega_{TL}$ is the frequency difference between the two lasers. The ± sign in Eq. (2.27) represents the fact that there are two stable locking points for the system. Under the steady state condition, $\frac{d\phi_e(t)}{dt} = 0$, and since the cosine function is bounded, the lock condition can be determined as

$$\left|\Delta\omega \pm \omega_{LO}\right| < K \tag{2.28}$$

which can be simplified to two conditions

$$\begin{cases} -K - \omega_{LO} < \Delta\omega < K - \omega_{LO} \\ -K + \omega_{LO} < \Delta\omega < K + \omega_{LO} \end{cases} \tag{2.29}$$

Equation (2.29) indicates two possible locking points, that is, the TL may lock to the reference laser, either when the TL is at frequency $\omega_{ref} - \omega_{LO}$ or when it is at $\omega_{ref} + \omega_{LO}$. This phenomenon can confuse the system when acquiring phase lock.

To address this issue the AAS is designed such that only one of the above two scenarios can take place. As discussed in Section 2.4.4, the AAS generates a ramp signal that is injected to the TL to bring the beat-note between the TL and the reference comb tooth within the acquisition range of the EOPLL. In this case, when the beat-note is on the left side of the LO signal (lower frequency) the ramp slope is positive and when it is on its right side (higher frequency) the slope is negative. For example, if the TL frequency is higher than that of the desired comb tooth (such that the beat-note signal is on the left side of the LO signal), the AAS ramps up the TL current, moving it to higher frequencies. As a result, the beat-note frequency increases towards that of the LO until the EOPLL performs phase locking (once the beat-note is within its acquisition range).

On the other hand, if initially the TL frequency is lower than that of the desired comb tooth, the generated ramp signal moves the TL frequency even further from the comb tooth. Therefore, the TL can only lock to a comb tooth with frequency lower than that of the TL. In order to phase lock the TL to a comb tooth at a higher frequency than the TL, the slope of the ramp signal should be reversed. Therefore, by setting the sign of the ramp signal slope, one of the solutions to Eq. (2.28) can be selected which resolves the false locking.

2.5.2 TL temperature stabilization response

As discussed in Section 2.2, the TL can be tuned by adjusting the mirror and/or phase section currents. Increasing (decreasing) the currents results in an increase (decrease) in the laser temperature. This variation in temperature changes the cavity conditions and hence the wavelength of the laser. This thermal wavelength variation not only makes phase locking challenging but also can cause the indexing system to lose the tooth count.

This problem is exacerbated for larger changes in the mirror/phase current. Consider the case that a large frequency change from the current frequency of the TL, f_1, to the target frequency, f_2, is desired. Correspondingly, the mirrors and/or phase section currents should change by a large amount (i.e. tens of mA). For this case, although the coarse tuning phase is performed in a fraction of a second, as explained in Section 2.3, when the frequency of TL reaches f_2 after counting certain number of teeth, its temperature has changed. A temperature controller loop is used to keep the temperature of the TL constant, however, the time required for the loop to acquire thermal equilibrium is usually much longer than the coarse tuning time. During the temperature stabilization process, the frequency of the TL varies, causing TL to move away from the target comb tooth and most likely pass through many comb teeth away from the target tooth. This also does not allow the EOPLL to robustly acquire/maintain phase lock. As mentioned in Section 2.4.4, the AAS is used to address this issue. When the coarse tuning process is done and the TL reaches f_2, the temperature of the TL is slowly changing around its set point. Therefore, the beat-note tends to pass over the LO signal. Here, the lock indicator system detects when the beat-note is moving away from the LO signal and the ramp generator keeps the beat-note within the acquisition range of the EOPLL by adjusting the current of the phase section of TL. Therefore, while the thermal loop is settling down, the TL remains phase-locked to the desired comb tooth. Fig. 2.17 shows the measured phase section current change for the case that a large mirror current change occurs. In this figure, the system is initially in thermal equilibrium and the TL is phase-locked to a comb tooth (at f_1). Then, both front and back mirror currents are changed by about 20 mA in less than a second to coarse tune the frequency of TL to f_2, resulting in a large temperature change. The loop reacquires phase lock the moment the coarse tuning is done. Simultaneously, while the laser's temperature is stabilizing, the phase section current is slowly changing to counteract the effect of temperature stabilization and keep the TL frequency constant.

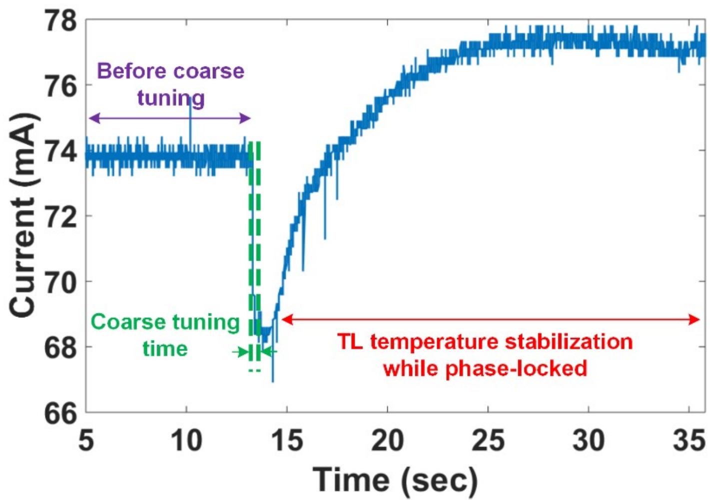

Figure 2.17 – Measured phase section current versus time when a large mirror current change happens showing how AAS counteracts the laser thermal fluctuations.

2.6 Optical frequency synthesis

To demonstrate optical synthesis, a widely tunable laser is required. As explained in section 2.2, a DBR laser custom fabricated by Infinera Corporation is used for this purpose. The measurement setup used to demonstrate optical frequency synthesis is shown in Fig. 2.18(a), where similar to Section 2.3, a method of phase-only modulation of a continuous wave reference laser is used to generate the reference frequency comb [28]. Fig. 8(b) shows the picture of the measurement setup where the main blocks are highlighted as well as the chip microphotograph of the EOPLL. In this setup, the tooth-spacing is set to 500 MHz. The output of the TL is combined with the reference comb and the resulting optical signal is divided into two branches using a 50/50 power splitter. One branch illuminates the photodiode connected to the input of the indexing system and the AAS. The other branch is further divided using a 10/90 optical power splitter where the 10% output is used for monitoring the optical spectrum and the 90% output illuminates the photodiode at the input of the EOPLL chip. The EOPLL chip requires differential quadrature LO heterodyning signals which are generated off-chip using a 180° hybrid and two 90° hybrids.

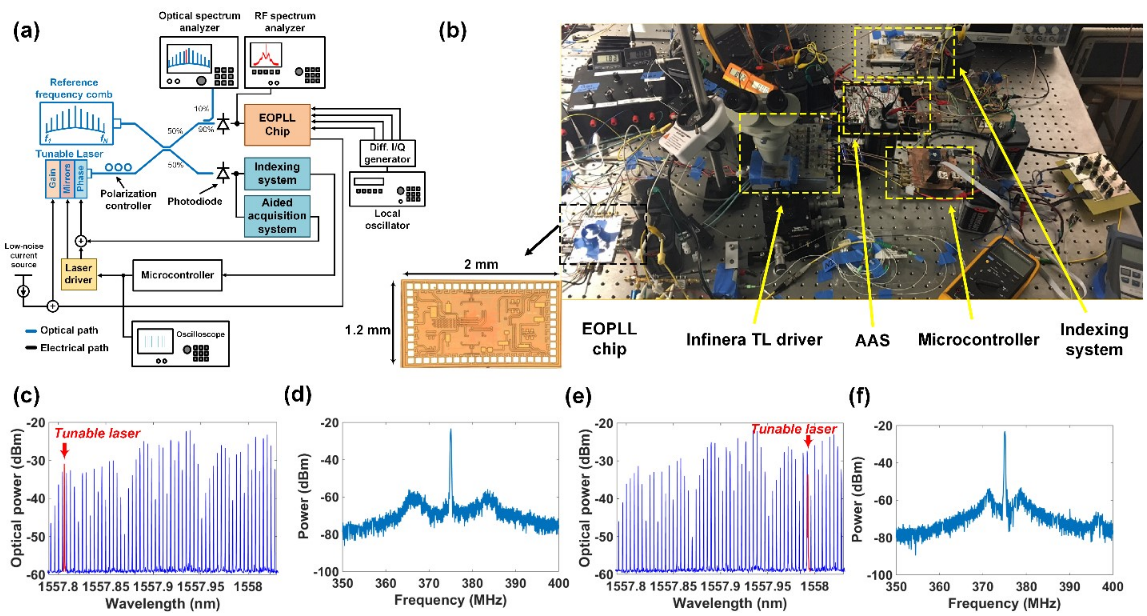

Figure 2.18 – (a) Measurement setup used for optical frequency synthesis demonstration and (b) the setup picture and the EOPLL chip microphotograph. (c) Optical frequency spectrum showing the initial location of the TL with respect to the reference comb and (d) the corresponding phase-locked beat-note spectrum. (e) Final location of the TL after coarse and fine tuning phases and (f) the corresponding lock spectrum.

The output of the indexing system is read by the microcontroller to count the number of teeth and set the laser driver currents to perform continuous TL coarse tuning. The gain section current consists of a dc bias current provided by a Thorlabs LDC201U ultra low noise current source as well as the output signal of the EOPLL chip for phase locking. The phase section current is composed of the current for coarse tuning and the current generated by the AAS to enhance the acquisition range and to keep the TL within the EOPLL acquisition range during temperature stabilization process. The mirror (front and back) currents are injected to the laser in the coarse tuning process. Using this architecture a coarse tuning speed and resolution of 0.5 THz/sec and 20 MHz are achieved, respectively.

At the end of the coarse tuning process, phase locking is done by the EOPLL. At this point, TL is fine-tuned by adjusting the frequency of the LO heterodyning signal. Fig. 2.18(c) to 2.18(f) show the optical synthesis result where the TL is initially at 1557.8063 nm and is phase-locked to a comb tooth with an offset frequency of 375 MHz (Fig. 2.18(c)). For this case, the lock spectrum (i.e. the spectrum of the beat-note under the locked condition) is shown in Fig. 2.18(d). Consider the case that the TL is to be tuned to the target wavelength of 1557.9924 nm. This wavelength is chosen to ease the illustration. First during the coarse tuning, front mirror, back mirror, and phase section currents are varied such that TL continuously is tuned to the vicinity of the target wavelength. While the TL is passing through the comb teeth, the indexing system generates two pulses per comb tooth as explained in Section 2.3. The desired range includes 47 teeth and hence, 94 pulses are generated in total.

When the microcontroller counts the proper number of pulses (in this case 94), it stops the coarse tuning. At this point, the EOPLL chip phase locks the TL to the tooth right next to the target comb tooth. Finally, optical frequency synthesis is completed when LO fine tuning is done. The final location of the TL with respect to the comb and the corresponding lock spectrum are shown in Fig. 2.18(e) and 2.18(f), respectively.

The fine tuning performance of the system is further investigated by conducting additional measurement mainly on the EOPLL chip and the AAS. These measurements include phase locking and phase noise reduction performance, fine tuning range by adjusting the LO heterodyning frequency, long-term stability of system, and fine tuning speed that are presented next.

As mentioned earlier in Section 2.4.2, under the phase lock condition, the frequency difference between the TL and the selected comb tooth is set by the heterodyning LO signal. Also, within the loop bandwidth, the TL phase noise follows that of the reference laser. This is shown in Fig. 2.19(a) where the spectrum of the beat-note before and after phase locking is depicted. From this figure, an effective loop bandwidth of about 5 MHz can be estimated which is primarily limited by the FM response cross-over frequency. The residual phase noise of the locked beat-note for LO heterodyning frequency of 300 MHz is measured which is compared with that of the LO heterodyning signal in Fig. 2.19(b). Fig. 2.19(c) shows the lock spectrum for different LO frequency settings. The implemented EOPLL is capable of phase locking for LO frequencies between 200 MHz and 1.3 GHz. However, given the 500 MHz comb tooth-spacing in this work, LO frequency range of 250 MHz to 500 MHz is considered.

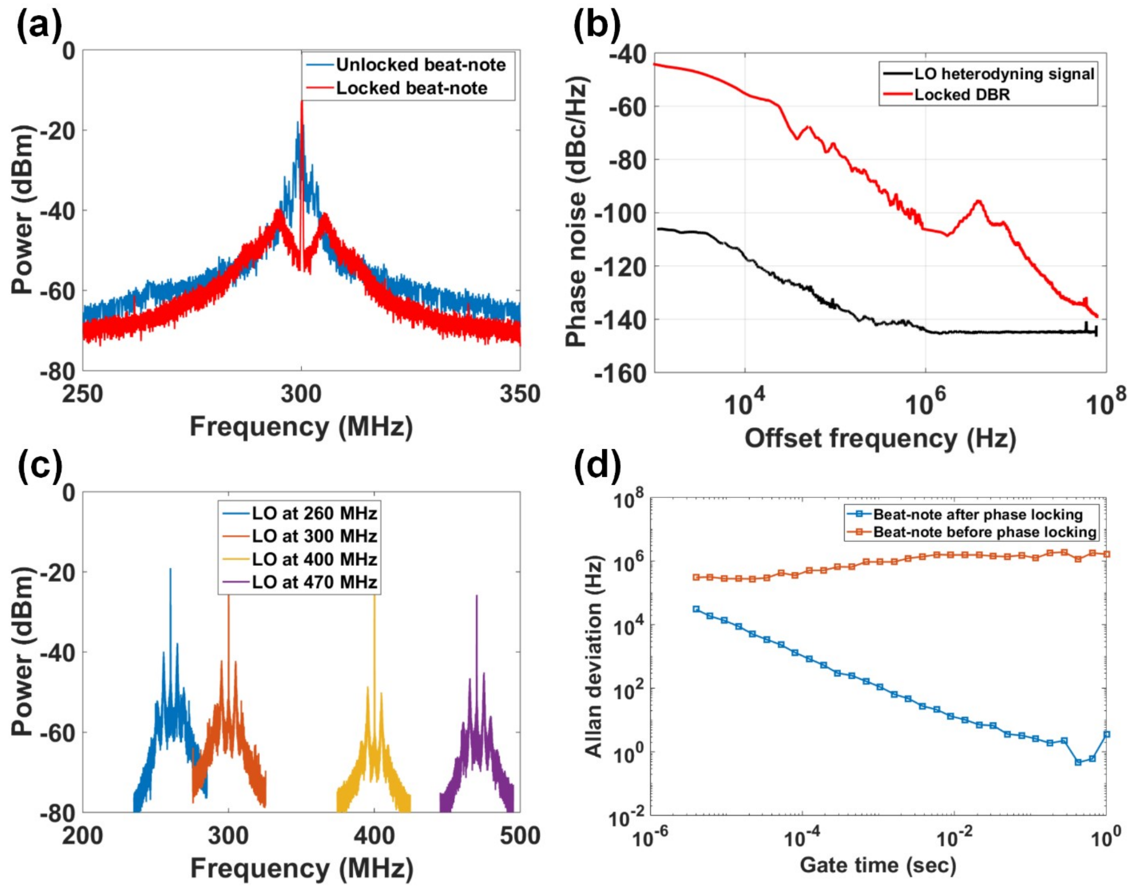

Figure 2.19 – (a) Beat-note spectrum before and after phase locking. (b) Measured phase noise of the locked beat-note and the LO heterodyning signal. (c) Lock spectrum for different f_{LO} settings. (d) Allan deviation measurement result.

Similar to an electrical frequency synthesizer, in an optical synthesizer the stability of the synthesized frequency tone is one of the critical characteristics of the system. To measure the Allan deviation of the synthesized optical signal, the beat-note signal is connected to a Tektronix FCA 3120 frequency counter. The Allan deviation of the free-running and phase-locked beat-notes for gate times between 4 μsec and 1 sec are shown in Fig. 2.19(d), where at a gate time of 1 sec, the stability is enhanced by about 6 orders of magnitude. Table 2.1 compares the performance of the EOPLL within the OFS with those of a few recent works.

Table 2.1 – Comparison if the implemented EOPLL with some of the recent works

	Slave tunable laser (linewidth)	**Reference laser (linewidth)**	**Loop bandwidth**	**Phase noise**	**Power consumption (electronics)**	**Area**	**Process (electronics)**
[44]	SG-DBR with a separate wideband tuning section (10 MHz)	Optical comb	400 MHz	-80 dBc/Hz at 200 Hz	400 mW	4 mm x 8 mm*	InP HBT chip (electronics)
[45]	DBR with a separate wideband tuning sections (1.25 MHz)	(100 kHz)	100 MHz	-100 dBc/Hz at 10 kHz	-	-	PCB implementation
This work	DBR with gain section as the tuning section (<1 MHz)	EO comb (<100 kHz)	5 MHz (limited by FM response)	-105 dBc/Hz at 1 MHz	28.5 mW	1.2 mm x 2 mm	180 nm CMOS SOI

Another important characteristic of a synthesizer is the tuning time, measured in both coarse and fine tuning phases. Measurements show a coarse tuning speed of about 0.5 THz/sec at 20 MHz frequency resolution. Using an electrical synthesizer (serving as the LO heterodyning signal) with small enough tuning time, the fine tuning time of the optical synthesizer would be limited by the acquisition time of the EOPLL. Figure 2.20(a) shows the setup used to measure the acquisition time of the EOPLL, where a voltage controlled oscillator (VCO) is used to provide the LO heterodyning signal to the EOPLL chip. The output signal of the EOPLL chip (which is injected to the gain section of the TL) is monitored on an oscilloscope while the beat-note spectrum is monitored on an electrical spectrum analyzer. To measure the EOPLL acquisition time, the VCO frequency is changed such that the loop loses and re-acquires lock periodically. This is done by applying a square wave signal to the control voltage of the VCO such that its frequency changes by about 50 MHz (which is larger than the acquisition range of the EOPLL). In this case, if the EOPLL is phase-locked when the square wave is at the low state, it will lose lock when the square wave signal quickly goes to high state as the LO heterodyning frequency changes instantly by an amount larger that the EOPLL acquisition range.

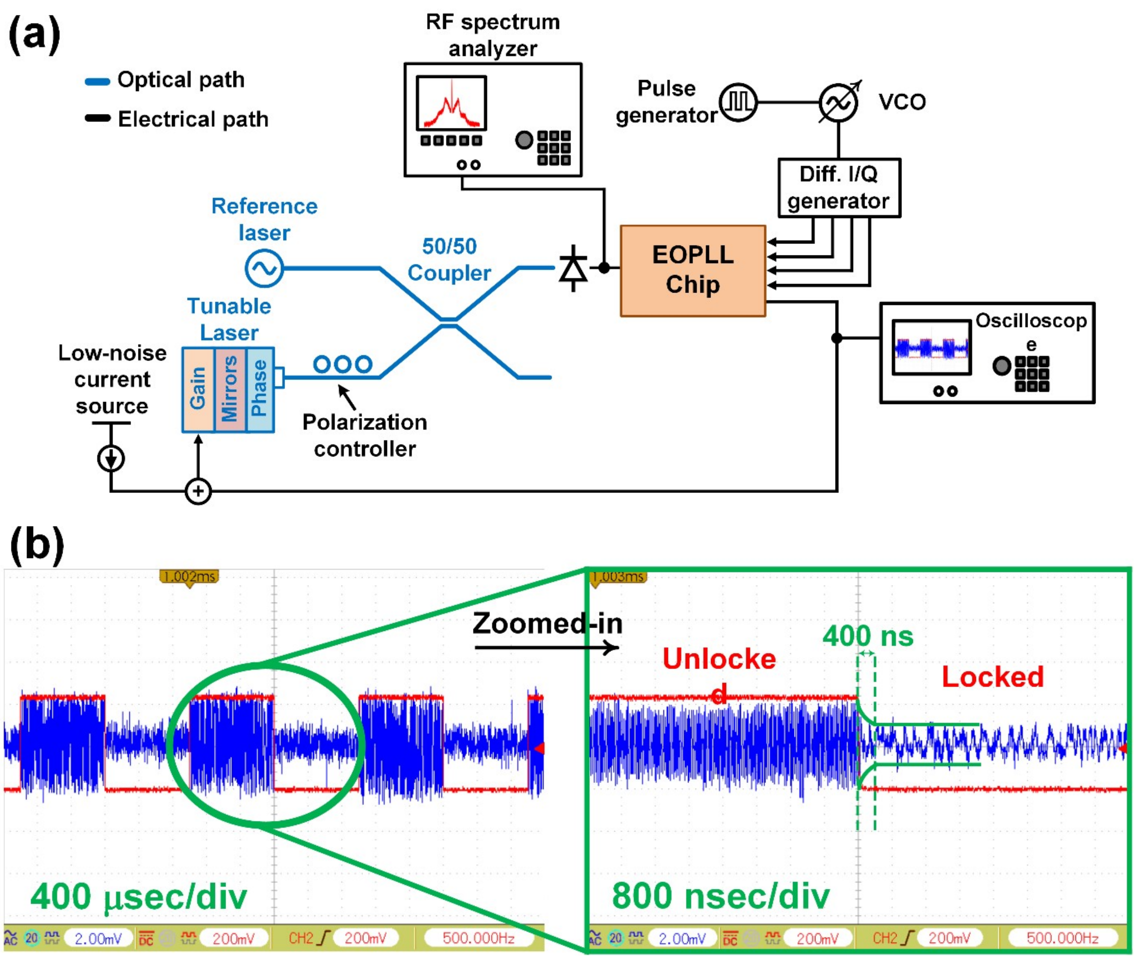

Figure 2.20 – (a) Measurement setup for EOPLL acquisition time and (b) the output of the EOPLL chip which is injected to the gain section of the TL.

Therefore, by applying the square wave signal to the VCO control voltage, the EOPLL will periodically be pushed out-of-lock and re-acquire lock. Note that, the state of the loop (i.e. whether it is phase-locked or not) can be followed by monitoring the beat-note spectrum (on the spectrum analyzer) as well as the EOPLL chip output (on the oscilloscope). In Fig. 2.20(b), the red signal shows the square wave signal applied to the control voltage of the VCO and the blue signal shows the AC component of the EOPLL chip output (injected to the TL gain section). When the EOPLL is phase-locked, the fluctuations of the EOPLL chip output is suppressed. Given that the rise/fall time of the square wave is much smaller than the lock/unlock transition in the EOPLL chip output, the acquisition time of the EOPLL can be approximated to be 400 nsec.

Table 2.2 – Implemented OFS performance summary

Center frequency	**192 THz**
Tuning range	**~ 5 THz**
Coarse tuning speed	**0.5 THz/sec**
Coarse tuning resolution	**20 MHz**
Find tuning range (without AAS)	**250 MHz (40 MHz)**
EOPLL acquisition time fine tuning)	**400 nsec**
Fine tuning resolution	**< 1 Hz**

2.7 Summary and future work

Based on the need for integrated OFS systems for various applications such as optical communications and sensing, I started working on the ways towards implementing a fully integrated OFS. In these applications, a stable, widely tunable and high resolution synthesizer is required. OFC-based synthesizers are one common approach where a widely tunable laser is phase-locked to different teeth of a stable low-noise optical comb as the reference. Therefore, a large frequency range can be covered while the TL is stabilized using a phase-locked loop. Recent advancements in demonstration of integrated optical frequency combs enable implementation of a highly stable frequency comb serving as the reference signal for the EOPLL in an integrated optical synthesizer.

As the first step, an integrated electro-optical phase locked loop (EOPLL) as the core of an optical synthesizer, where photonic and electronic devices are integrated in a standard silicon-on-insulator (SOI) process was implemented. A sophisticated integrated electronic-photonic architecture is proposed enabling reliable, low-cost, and high resolution optical synthesis. The small on-chip optical delay and electronically assisted frequency detection and acquisition provide tunable phase and frequency locking. The integrated EOPLL was fabricated using Global Foundries 7RFSOI process which is a standard CMOS process. The chip consumes 28.5 mW with total chip area of 2.4 mm^2 making it comparable with electrical synthesizers enabling large-scale deployment in applications such as low-cost optical spectroscopy, detection, sensing, and optical communication.

In the next step, the EOPLL chip was used to implement a partially integrated OFS. In the proposed architecture, frequency synthesis is done in two phases. In a coarse tuning phase, a widely tunable distributed Bragg reflector (DBR) laser is continuously tuned by adjusting its mirrors and phase section currents. While the laser is being tuned, an indexing system detects and counts the number of passing comb teeth. Coarse tuning is concluded when the tunable laser reaches the target comb tooth. Following the coarse tuning phase, a heterodyne integrated EOPLL phase locks the tunable laser to the selected comb tooth. An aided acquisition system, improves the acquisition range of the EOPLL to 250 MHz making it compatible with the 500 MHz tooth-spacing of the OFC. Under the phase-locked condition, fine frequency tuning is performed by adjusting the frequency of a RF local oscillator. The proposed synthesizer has the capability of synthesizing optical frequencies over a 5 THz range with a coarse tuning speed of 0.5 THz/sec and coarse and fine tuning resolutions of 20 MHz and less than 1 Hz, respectively. Experimental results of frequency synthesis as well as extensive characterization results of different block of the implemented system are presented.

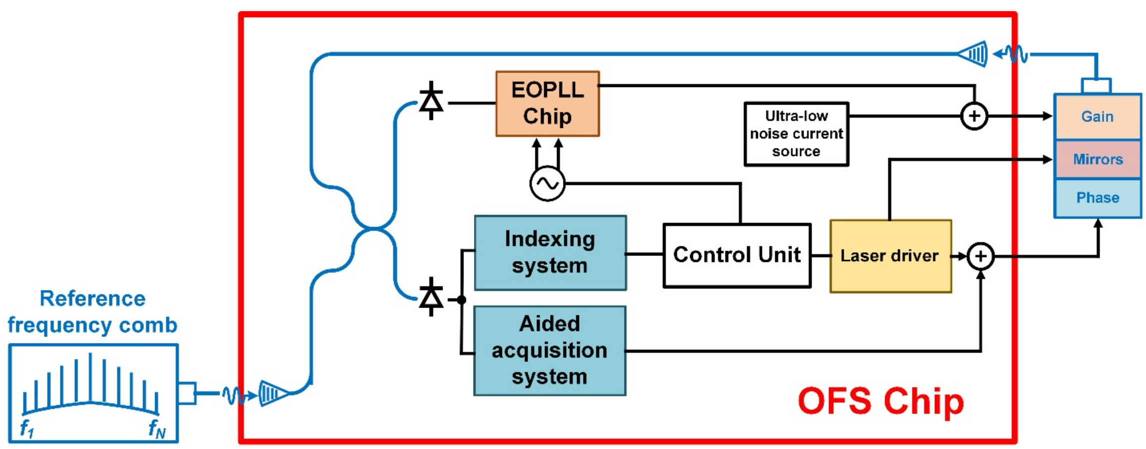

Figure 2.21 – The block diagram of an OFS that integrates all electronic blocks.

As an immediate continuation of this work, all blocks together with the EOPLL chip can be integrated on the same chip which results in a lower power consumption, lower cost, and smaller size of the system. Larger bandwidth electronics can be designed for the

EOPLL and AAS. This relaxes the filter design for the indexing system and allows for larger tooth-spacing for the OFC, which generally can result in larger SNR and higher power per comb tooth. Finally, depending on the available fabrication processes, the proposed system can be co/hybrid integrated with the OFC to realize a fully integrated OFS. Figure 2.21 depicts the top level chip architecture of a fully integrated OFS.

CHAPTER 3

Optical signal processing: A nanophotonic near-field imager

Unlike the radio and microwave frequencies, where lack of enough bandwidth is a serious challenge in many applications, in the optical domain, very large bandwidths are available. This provides a great opportunity of implementing systems in which data processing is performed in the optical domain rather than the conventional electrical signal processing to realize much faster systems. This has resulted in many works in the field of microwave photonics. These works include different applications from signal generation to phased arrays [46-48]. In true-time delay based antenna arrays [48] more compact and more efficient delay elements can be implemented in the optical domain.

Ultra-wideband (UWB) near- and far-field imagers utilize a large bandwidth in the microwave regime enabling implementation of near-field radar [49,50], through-the-wall imaging [51,52], tracking and positioning [53], low power communication for internet-of-things (IoT) [54], and high depth resolution imaging [55]. In medicine, these imagers have been used for cancer cell detection [56,57], brain imaging [58], imaging of heart motions [59,60] and respiration rate monitoring [61], to name a few. UWB describes systems whose instantaneous fractional bandwidth, defined as the ratio of -10 dB bandwidth to the center frequency, exceeds 20% [62]. High depth and azimuth resolution, penetration through optically opaque obstacles, and capability of imaging in different weather conditions have made UWB systems suitable for many applications.

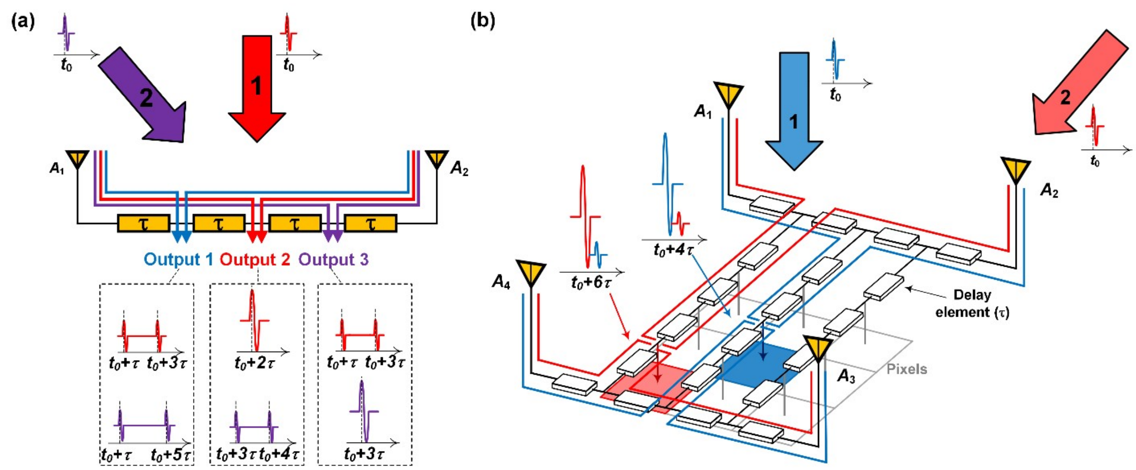

Figure 3.1 – (a) The 1-D multi-beam antenna array with three simultaneous outputs. (b) 2-D multi-beam array.

Conventionally, UWB near-field imagers have been implemented as bench-top systems [49,50], where a train of narrow time domain pulses, often monocycles [63-65], illuminate the target object and the reflected pulses are received using a wideband antenna array and processed to form the image. Despite excellent performance, these bench-top implementations are bulky, expensive, and suffer from high power consumption and are susceptible to electromagnetic interference.

One way to improve the performance of such imagers is to concurrently receive the impinging signals from different directions using multi-beam antenna arrays. Figure 3.1(a) shows the one dimensional (1-D) architecture of a multi-beam antenna array, where fixed delay elements in a delay-sharing architecture are used [63]. Depending on the angle of incidence, two antennas receive the signal with different delays. The received signals are coherently combined at a certain output, where the delay difference is compensated by the delay line network. This architecture uses three simultaneous outputs where antennas A_1 and A_2 receive signals at different times depending on the angle of incidence. For the case of normal incidence (direction 1, red signal), two signals are combined coherently at output 2 after both passing through the same amount of delay of 2τ. For the case that the pulse impinges on the array from direction 2 (purple signal), the pulses received by antennas A_1 and A_2 are delayed by 3τ and τ, respectively, and combined coherently at output 3.

The delay sharing architecture can be extended to a 2-D antenna array as shown in Fig. 1(b). For normal incidence (direction 1), signals received by A_1 to A_4 experience the same delay (4τ) and are coherently combined at the center pixel. For a pulse impinging from direction 2, the pulse received by antennas A_1 and A_3 are delayed by 4τ while the pulse received by antennas A_2 and A_4 are delayed by 6τ and 2τ, respectively. The resulting four aligned pulses are coherently combined at the red pixel.

In the electrical domain, on-chip electrical delay lines are typically implemented either by setting the length of a transmission line [66,67] or periodically loading the transmission line with series inductors and shunt capacitors to change the propagation velocity [68]. In both methods, the loss of the silicon substrate introduces a large propagation loss for the on-chip delay lines [69]. For imagers with large number of delay lines, amplifiers and buffers may be used [66] to compensate for the loss of the delay line at the cost of increased power consumption and noise, reduced bandwidth, and delay non-uniformity. Also, long transmission lines per delay element (due to the high propagation velocity) in the former method, and the large size of the inductors in the latter method result in a large per-delay element area and high vulnerability to electromagnetic interference.

High optical confinement, low propagation loss offered by nanophotonic waveguides, and large bandwidth available around the optical carrier make CMOS compatible silicon photonic platforms good candidates for implementation of integrated microwave photonic systems. The large group index in silicon-on-insulator waveguides, corresponding to a lower wave propagation velocity compared to typical electrical transmission lines, results in larger delay per-length, which together with significantly lower propagation loss and immunity to electromagnetic interference make the optical delay lines a good candidate for implementation of UWB near-field imagers with a large pixel count. This will be discussed in details in Section 3.1.

In this chapter, the first integrated nanophotonic near-field imager is presented where the reflected wideband microwave signals from the target object are received using UWB antennas, up-converted to the optical domain using electro-optic ring modulators, delayed and processed using a network of optical delay lines, and photo-detected using a matrix of 11x11 photodiodes. The photo-currents are further amplified and energy detected to form the near-field image of the target object. The implemented nanophotonic near-field imager utilizes photonic delay lines with about 44 times smaller chip area compared to the equivalent state-of-the-art electrical delay lines [63,66] and achieve more than 16 times lower propagation loss compared to the equivalent delay lines implemented on electronic processes with advanced metal stack. The photonic delay line implementation, processing, distribution, and beamforming enable the scalability of the proposed architecture to an imager with a large number of pixels. Furthermore, unlike electronic implementations, the photonic delay lines and devices are immune to undesired magnetic coupling and electromagnetic interference in the microwave regime. The imager chip, fabricated using IME 180 nm silicon photonic SOI process, is capable of receiving 121 simultaneous beams with a delay resolution of 9.8 ps (with a footprint of 360 μm^2/ps) and is used to form the near-field image of different objects.

The rest of the chapter is organized as follows. In Section 3.1, the concept of optically delaying an electrical signals is studies and the implemented photonic delay element is compared with the electrical counterpart. Section 3.2 presents the architecture of the proposed imager chip and discusses important considerations of the system. Before near-field imaging demonstration, the imager is characterized using wired and wireless setups and the results are presented in Section 3.3. Section 3.4 contains the results of imaging different metallic objects. Some of the specification so of the imager such as dynamic range, linearity, and noise figure are studied in Section 3.5. Finally, Section 3.6 summarizes the chapter and introduces some of possible future research directions.

3.1 Optically delayed electrical pulse

A key concept in the implementation of the proposed nanophotonic near-field imager is that an electrical pulse can be optically delayed, that is, if an optical carrier is modulated with an electrical pulse, optically delayed by τ, and demodulated, the recovered electrical pulse is delayed by τ. Figure 3.2(a) shows the structure of the nanophotonic waveguides used to implement the photonic delay lines (Fig. 3.2(b)). The delay element is constructed of single-mode as well as multi-mode waveguides to achieve small size and low loss simultaneously. In the IME process used in this work, the multi-mode waveguide has a propagation loss of better than 0.3 dB/cm. This number for a single-mode waveguide is about 2 dB/cm. Multi-mode waveguide is used for the long straight waveguides to lower the propagation loss. Other section of the delay element are made of single-mode waveguide to make size smaller since wider waveguide need larger bend radius which results in larger size. The delay cell introduces a delay of 9.8 ps.

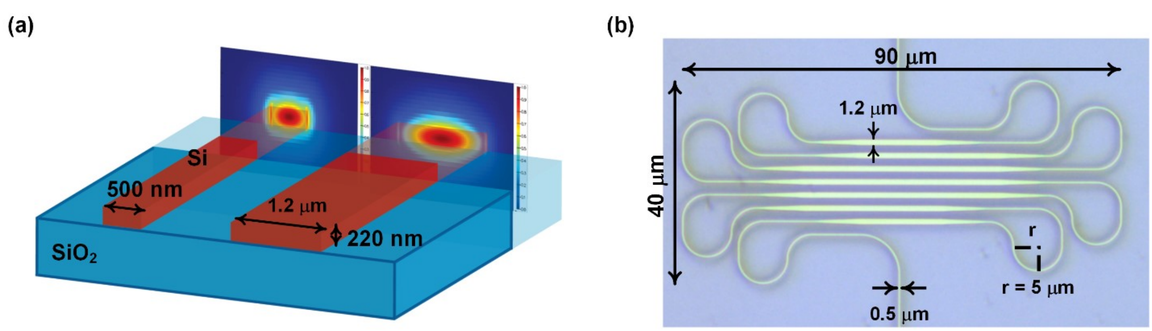

Figure 3.2 – (a) Single-mode and multimode silicon waveguides implemented in IME 180 nm silicon-on-insulator (SOI) photonic process and the corresponding mode profile at 1550 nm. (b) Delay cell microphotograph.

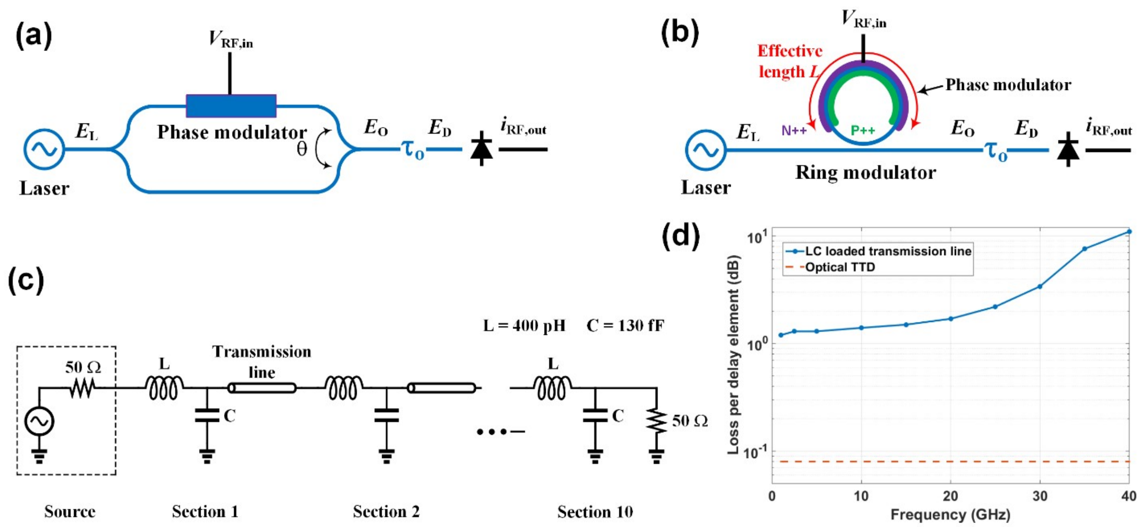

Figure 3.3 – Optically delayed electrical pulse and comparison of optical and electrical delay lines. (a) Optically delayed electrical signal using a MZM. (b) Optically delayed electrical signal using a ring modulator. In both a and b, the modulator is followed by a delay cell to optically delay the electrical signal $V_{\mathrm{RF,in}}$. (c) Schematic of a loaded transmission line with LC segments. Each transmission line segment is 250 μm long and the inductor and capacitor values are 400 pH and 130 fF, respectively. (d) Comparison between the simulated per-delay element loss of the implemented optical delay and that of the LC loaded transmission line for the same delay of 9.8 ps.

As mentioned above, one of the main concepts in the design of the integrated nanophotonic near-field imager is that an electrical pulse can be delayed optically. In this case, an optical signal is first modulated by the input electrical signal, delayed using a true-time-delay (TTD) cell, and photo-detected to recover the delayed version of the input electrical signal. Here we consider this effect for two typical cases, where the electro-optical conversion is performed using either a Mach Zehnder modulator (MZM) or a ring modulator.

Figure 3.3(a) shows the block diagram of the system that optically delays an electrical signal with a MZM as the intensity modulator. Consider the case that the electric field of the optical wave in the form of $E_L = \sqrt{P_0}e^{j(\omega_0 t)}$ is modulated with the input radio frequency (RF) signal $V_{RF} = v_0 \cos(\omega_{RF} t)$ using the MZM. When the phase difference between the two arms of the MZM, θ, is set to 90°, the electric field of the modulated optical signal is written as

$$E_o = \frac{1}{2}e^{j(\omega_0 t)}\left[j\sqrt{P_0} + \sqrt{P_1}e^{j(\frac{\pi}{V_\pi}V_{RF}(t))} \right], \tag{3.1}$$

where $P_0, P_1, \omega_0, v_0, \omega_{RF}$, and V_π are the laser power (before the modulator), the light power after the phase modulator (in the top branch of the MZM), the laser frequency, the RF signal amplitude, the RF signal frequency, and the modulator phase-to-voltage gain, respectively. The modulated signal is delayed using an optical TTD cell with a delay of τ_0. The resulting electric field of the delayed optical signal is written as

$$E_D = \frac{1}{2}e^{j\left(\omega_0(t-\tau_0)\right)}\left[j\sqrt{P_0} + \sqrt{P_1}e^{j(\frac{\pi}{V_\pi}v_0\cos\left[\omega_{RF}(t-\tau_0)\right])} \right]. \tag{3.2}$$

The delay line output is photo-detected and the photo-current is written as

$$i_{RF,out} = \frac{1}{4}R\left[P_0 + P_1 + 2\sqrt{P_0 P_1}\sin\left(\frac{v_0}{V_\pi}\cos\left[\omega_{RF}\left(t-\tau_0\right)\right] \right) \right], \tag{3.3}$$

where R represents the photodiode responsivity. In this case, using the Jacobi-Anger expansion [70] the fundamental component of the photo-current is written as

$$i_{RF,out} \approx R\sqrt{P_0 P_1} J_1 \frac{v_0}{V_\pi} \cos\left[\omega_{RF}\left(t-\tau_0\right)\right]. \tag{3.4}$$

Equation (3.4) indicating that the electrical signal is delayed by the amount of the delay of the optical TTD element. Note that J_1 denotes the Bessel function of the first kind.

Figure 3.3(b) shows the block diagram of the system that optically delays an electrical signal using a ring modulator. Consider the case that the electric field of the optical wave in the form of $E_L = \sqrt{P_0} e^{j(\omega_0 t)}$ is modulated with the input RF signal $V_{RF} = v_0 \cos\left(\omega_{RF} t\right)$ using a ring modulator. The applied RF signal perturbs the index of refraction of the ring structure [71], that is

$$n(t) = n + \Delta n \cos\left(\omega_{RF} t\right), \tag{3.5}$$

where n is the constant (un-perturbed) index and $\Delta n = \frac{\lambda_0}{2L}\left(\frac{v_0}{V_\pi}\right)$ is the amplitude of index change due to the applied RF signal, λ_0, L and V_π are the laser wavelength in free-space, the effective length of the phase modulator in the ring, and the phase-to-voltage gain, respectively. In this case, the instantaneous output power of the ring modulator can be approximated as [71]

$$P_o = P_1 + H_n\left(\omega_{RF}\right) \Delta n \cos\left(\omega_{RF} t + \phi\right), \tag{3.6}$$

where P_1 is the constant part of the output optical power, ϕ is the phase of the small-signal instantaneous output power, and $H_n\left(\omega_{RF}\right) = \frac{\Delta n}{\Delta p}$ is the linearized transfer function as the ratio of the output power perturbation to the small-signal index perturbation, which can be written as [71]

$$H_n\left(\omega_{RF}\right)=P_{in}\left[\frac{\omega_r}{n}\times\frac{2\delta}{\delta^2+\dfrac{1}{4\tau^2}}\times\frac{k_e^2}{T}\times\frac{j\omega_{RF}+\dfrac{1}{2\tau}}{\left(j\omega_{RF}\right)^2+j\dfrac{\omega_{RF}}{\tau}+\dfrac{1}{4\tau^2}+\delta^2}\right], \tag{3.7}$$

where $\omega_r,\tau,\delta=\omega_0-\omega_r,\omega_0,k_e,$ and T are the resonance frequency of the ring, the photon lifetime, the difference between the input laser frequency and the ring resonance frequency, the frequency of the input laser, the coupling coefficient of the ring modulator, and the round trip time of the ring, respectively. Equation (3.7) indicates that in presence of an input optical wave and a known modulating RF signal, $H_n\left(\omega_{RF}\right)$ is a constant and therefore, based on Eq. (3.6), the time varying part of the output power is only proportional to $\cos\left(\omega_{RF}t\right)$. The modulator output is delayed using an optical TTD cell with delay of τ_0 and photo-detected using a photodiode with responsivity of *R*. In this case, the AC component of the photo-current is written as

$$i_{RF,out}=RH_n\left(\omega_{RF}\right)\frac{\lambda_0}{2L}\left(\frac{1}{V_\pi}\right)v_0\cos\left(\omega_{RF}\left(t-\tau_0\right)+\phi\right). \tag{3.8}$$

indicating that the electrical signal is delayed by the amount of the delay of the optical TTD element.

3.1.1 Comparison of electrical and optical delay lines

Conventionally, the all-electrical on-chip delay lines are implemented either by setting the length of a transmission line [67] or periodically loading a transmission line with series inductors and shunt capacitors (LC segments) to change the propagation velocity [68]. In both methods, the loss of the silicon substrate introduces a large propagation loss for the on-chip delay lines [69]. For imagers with small number of delay lines, repeating amplifiers (or line amplifiers) may be used [63] to compensate for the loss of the delay line at the cost of high power consumption, excess noise, and reduced bandwidth, and delay non-uniformity. In addition, the long transmission line per delay element (due to the high propagation velocity) in the former method, and the large size of the inductors in the latter method result in a large per delay line chip area. The resulting large area and high power consumption of the on-chip electrical delay lines as well as sensitivity to magnetic coupling and vulnerability to electromagnetic interference significantly limit the scalability of on-chip near-field imagers implemented on standard electronic processes. Between the two aforementioned design methods for electrical TTD elements, the second method is often preferred [63] as it provides an overall smaller delay element size. Note that the loss of the LC segments (or transmission lines) increases with frequency while that of the optical TTD remains constant across a large frequency range.

Figure 3.3(c) shows the schematic of an integrated all-electrical delay line implemented using a loaded transmission line with LC segments. Figure 3.3(d) shows the simulated loss per delay cell of the structure in Fig. S1(c), implemented using top two metal layers (4 μm thick aluminum and 0.5 μm thick copper) in a standard 90 nm RF CMOS SOI process with 7 metal layers, which is compared with the loss of the optical

TTD element, implemented on IME silicon-on-insulator process, for the same delay of 9.8 ps. As expected, for the same delay, the loss of the optical delay line is significantly lower than that of the LC loaded transmission line. Furthermore, the loss of the LC loaded transmission line increases with frequency while that of the optical delay line remains unchanged. At 2.5 GHz and 35 GHz, the loss of the optical delay line is 16 times and 100 times lower than that of the electrical delay line, respectively.

3.2 System architecture

This section presents the design of the proposed nanophotonic imager. Figure 3.4(a) shows the structure of the photonic-assisted one-dimensional UWB antenna array as an essential building block of the implemented imager. The impinging wideband microwave signal is received using two antennas, amplified, and used to modulate the input light using ring modulators [72]. The light at the output of each modulator is guided to an array of delay lines. A directional coupler is placed after each delay element to tap-off a part of the light. The coupling length of each directional coupler is adjusted to ensure that all directional couplers have the same output power and the ratios are shown in Fig 3.4(b). An array of Y-junctions is used to combine the outputs of the directional couplers in the top delay line array (processing the light travelling from left to right) with the outputs of the corresponding directional couplers in the bottom delay line array (processing the light travelling from right to left) forming the output waveguide array from out 1 to out 11 in Fig. 3.4(a). Note that two separate delay line arrays are used to isolate the optical path after each ring modulator, avoiding wave interference at undesired nodes. In this case, depending on the angle of incidence of the impinging pulse, the two optical waves, travelling in opposite directions, will be coherently power combined at one of the outputs (out 1 to out 11). The characterization and optical power distribution uniformity of the photonic-assisted 1-D UWB delay line array is discussed in more details in Section 3.3.1.

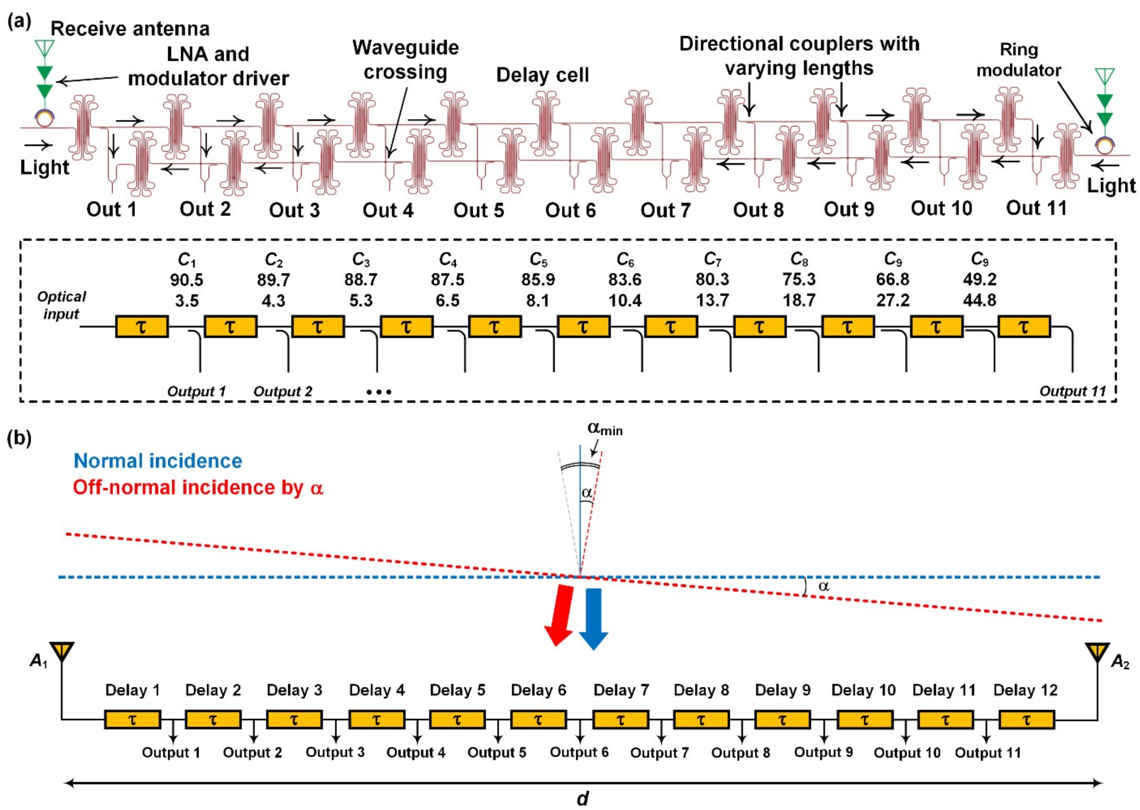

Figure 3.4 – (a) The structure of the photonic-assisted one-dimensional UWB antenna array including 1x2 array of UWB antennas. (b) Directional coupler ratios. (c) Schematic of the 1-D array for *SR* and *FOV* calculation.

The number of delay elements and the amount of delay are important in determining the field of view as well as the spatial resolution of the imager. As shown in Fig. 3.4(c), assuming that the antennas receive the incoming signal at a specific angle, α, the spatial resolution (SR) and the field-of-view (FOV) can be calculated as [55]

$$SR = 2\sin^{-1}\left(\frac{c_0\tau}{d}\right). \tag{3.9}$$

$$FOV = \pm\sin^{-1}\left(\frac{(N-1)c_0\tau}{d}\right). \tag{3.10}$$

where c_0 is the speed of light in free space, τ is the delay of the delay lines, N is the number of delay lines per row/column, and d is the UWB antenna spacing. As explained in more details in Section 3.3, in the implemented 11x11 imager, antenna spacing is about 7 cm, the delay of each delay line is 9.8 ps, and the number of delay lines per each row/column is 12, which results in a spatial resolution of about 4.8° and a field-of-view of about ±27°.

Figure 3.5(a) shows the structure of the implemented nanophotonic near-field imager. A laser emitting 30 mW at 1550 nm is coupled into the chip input waveguide using a grating coupler. The coupled light is then split into four branches and guided to the top and bottom 1-D UWB antenna arrays, which are identical to the structure in Fig. 3.4(a) and serve as the top and bottom distribution networks for eleven delay line columns. Delay line columns are also identical to the delay line array in Fig. 3.4(a) (without the ring modulators) but rotated by 90 degrees. An array of 11x11 photodiodes, the imager pixels, are used to photo-detect the outputs of all columns.

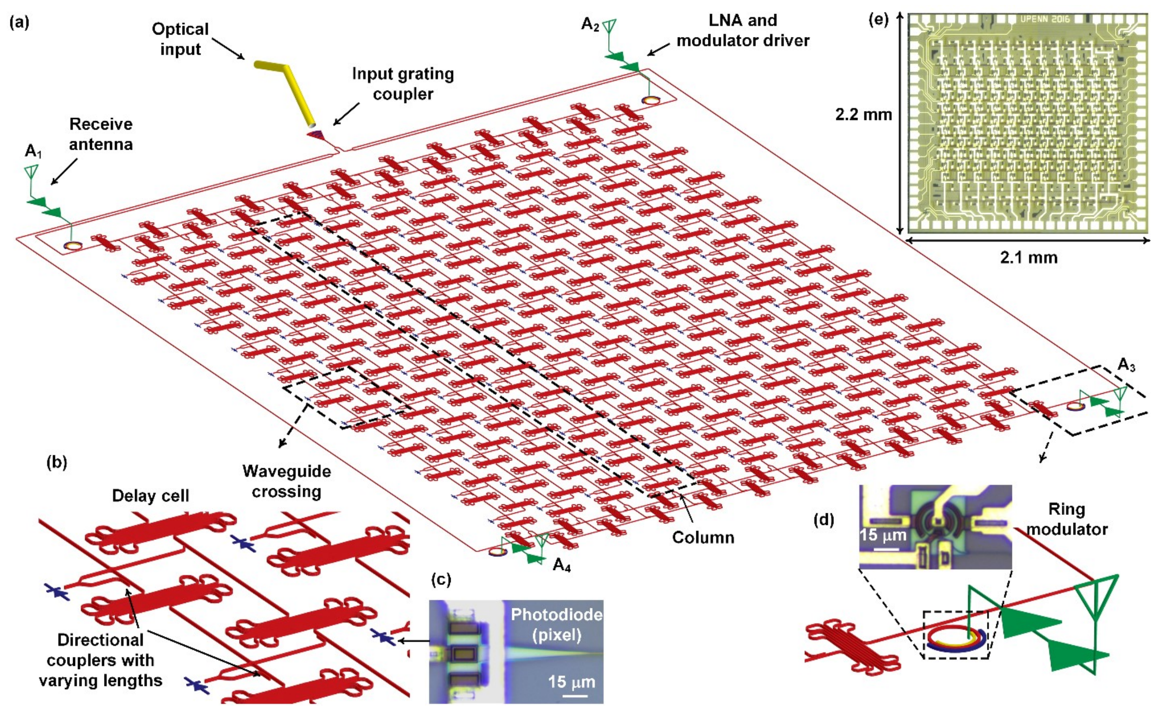

Figure 3.5 – (a) Structure of the 11x11 imager. (b) Waveguide connections illustrating the delay cell, the waveguide crossings, and the directional couplers. (c) Microphotograph of the photodiode. (d) Microphotograph of the ring modulator. (e) Microphotograph of the 11x11 nanophotonic near-field imager integrated in the IME 180 nm silicon-on-insulator process.

The SiGe photodiode have been previously designed and characterized to have a responsivity of 0.75 A/W at 1550 nm and 3dB bandwidth of more than 30 GHz. The impinging signals are received by an array of 2x2 UWB antennas, amplified, up-converted to the optical domain, and travel through the on-chip network of delay lines. The ring modulator has a 3dB bandwidth of more than 30 GHz [72]. Depending on the angle of incidence, four UWB pulses will arrive at the same time at a certain pixel for which the relative delays between the received RF pulses are compensated by on-chip optical delay lines and, ideally, are coherently power-combined before photo-detection. However, since a coherent light source is coupled to the chip, a path mismatch and/or thermal gradient can affect the phase of these four aligned pulses at the combining point preventing a constructive addition. To address this issue, the laser is frequency chirped and is guided to the four ring modulators using on-chip waveguides with different lengths resulting in different optical carrier frequencies at the point of modulation as well as the combining points at the pixels. This is discussed in details in Section 3.2.1. Figure 3.5(b) shows the zoomed-in version of the waveguide connections. Figures 3.5 (c), 3.5 (d) and 3.5(e) show the microphotographs of the SiGe photodiode, ring modulator, and the integrated nanophotonic near-field imager, respectively

3.2.1 Coherence effect on image SNR

In the implemented nanophotonic near-field imager, for a given angle of incidence of the impinging UWB pulse, all four modulated optical waves will arrive at the same time at a certain pixel, where they are combined and photo-detected. Since all four modulated optical waves are originated from the same laser, their constructive addition at the combining point depends on their instantaneous relative phases. Therefore, phase mismatches between these four optical waves, as a result of fabrication process variations, thermal gradient across the chip, or other effects, may affect their constructive addition lowering the detection SNR. Figure 3.6 shows the block diagram of our proposed scheme to address this issue. The laser source is frequency chirped and coupled to the chip. The coupled light is split into four branches and guided to the four ring modulators using waveguides with different lengths (corresponding to four different delays of T_1 to T_4).

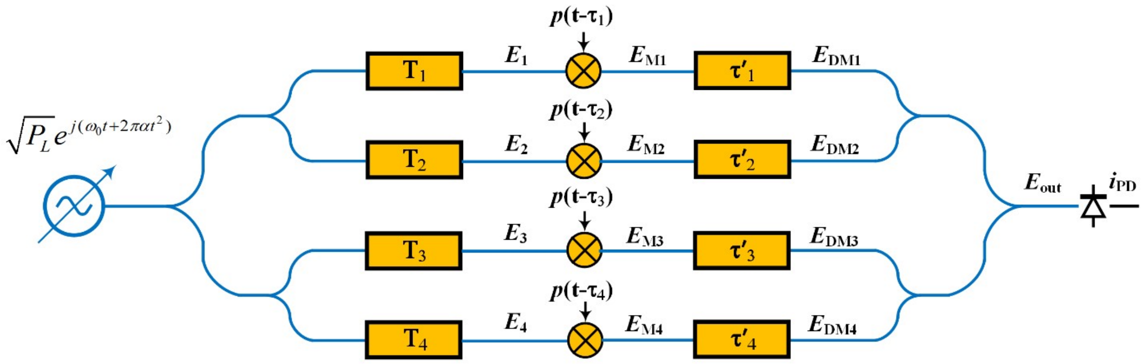

Figure 3.6 – Proposed scheme to address the potential phase mismatch between optical waves at the combining point before each pixel.

Consider the case that the laser output electric field after frequency chirping is written as $E_L(t)=\sqrt{P_L}e^{j(\omega_0 t+2\pi\alpha t^2)}$ where P_L, ω_0, and α are the laser power, the laser frequency, and the laser frequency chirp rate, respectively. The electric field of the light in the ith branch (i =1, 2, 3, 4) after the delay line (right before the ring modulator) is written as $E_i(t)=\sqrt{P_0}e^{j(\omega_i t+\phi_i)}$, where $\omega_i=\omega_i-4\pi\alpha T_i+2\pi\alpha t, \phi_i=2\pi\alpha T_i^2-\omega_o T_i+\psi_i, P_0, T_i$, and ψ_i are the frequency of the optical wave, phase of the optical wave, the power of the optical wave in each branch, the delay of the ith waveguide (before the ith ring modulator), and a constant phase, respectively. The UWB pulse waveform, *p*(t), impinging from a certain direction, arrives at the ith ring modulator (on the ith branch) with the delay τ_i of (which is set by the angle of incidence). The electric field of the modulated light after the ith modulator is written as

$$E_{M,i}(t) = p(t-\tau_i)\sqrt{P_M}\, e^{j(\omega_i t+\phi_i)}, \tag{3.11}$$

where the modulator is approximated as an electro-optic multiplier. The light at the output of the ith modulator is optically delayed by $\tau_i^{'}$ such that output of all four modulators arrive at a certain pixel at the same time, that is, $\tau_i + \tau_i^{'} = \tau_0$ for i =1, 2, 3, 4. In this case, the four modulated optical waves at the combining point are written as

$$E_{DM,i}(t) = p(t-\tau_0)\sqrt{P_{DM}}\, e^{j(\omega_i^{'} t+\phi_i^{'})}, \tag{3.12}$$

where $\omega_i^{'} = \omega_i - 4\pi\alpha\tau_i^{'}, \phi_i^{'} = \phi_i + 2\pi\alpha\left(\tau_i^{'2} + 2\tau_i^{'}T_i\right) - \omega_o\tau_i^{'} + \theta_i, P_{DM}$, and θ_i are the frequency of the optical wave in each branch at the combining point, the phase of the optical wave in each branch at the combining point, the power of the optical wave in all four branches at the combining point, and the optical constant excess phase at the combining point, respectively. The electric field of the optical wave at the combiner output is written as

$$E_{out}(t) = p(t-\tau_0)\sqrt{\frac{P_{DM}}{2}}\sum_{i=1}^{4} e^{j(\omega_i^{'} t+\phi_i^{'})} E_{DM,i}(t), \tag{3.13}$$

The output optical wave is photo-detected and the photo-current is written as

$$i_{PD}(t) = RE_{out}E_{out}^{*} = \frac{RP_{DM}}{2} p^2(t-\tau_0)\left\{4 + 2\sum_{\substack{j=1 \\ j\neq k}}^{4}\sum_{k=1}^{4}\cos\left[\left(\omega_j^{'} - \omega_k^{'}\right)t + \phi_j^{'} - \phi_k^{'}\right]\right\}, \tag{3.14}$$

where R is the responsivity of the photodiode. The photo-current is amplified and converted to a voltage using a trans-impedance amplifier (TIA) resulting in $v_{out}(t) = Gi_{PD}(t)$, where G is the trans-impedance of the TIA. Finally, a power detector integrates v_{out} to find the output power as

$$P_{out} = \left(GRP_{DM}\right)^2 P_{p^2}. \tag{3.15}$$

where P_{p^2} is the power of the pulse squared and all cos(.) terms in Eq. (3.14) are averaged to zero during integration. Equation (3.15) shows that the detected power does not depend on the relative phase between the four modulated optical waves at the combining point. Note that for the pixels that receive only one pulse, Eq. (3.15) is modified to $P_{out} = \frac{1}{4}\left(GRP_{DM}\right)^2 P_{p^2}$,indicating a factor of four contrast, which is the same as the image contrast in [63].

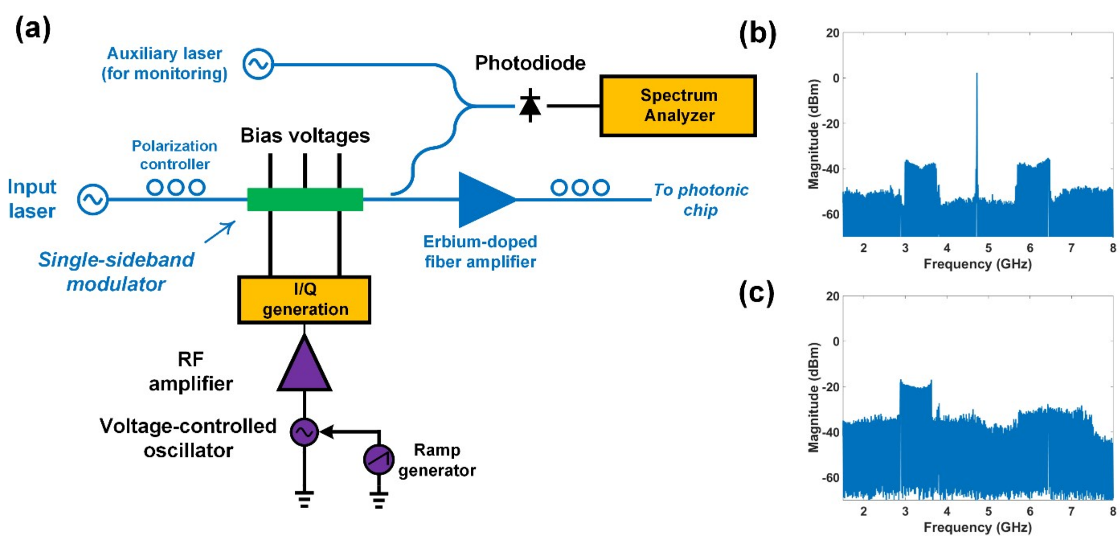

Figure 3.7 – Chirp generation. (a) Block diagram of the laser frequency chirp generation system. (b) Spectrum of the optical signal with zero modulator bias and, (c) with single-sideband operation biasing condition, where the optical carrier and the undesired sideband are significantly suppressed. The frequency spectrum of the laser is down-converted using an auxiliary laser.

Figure 3.7(a) shows the block diagram of the chirp generation system, where the output of a HP-8168F tunable laser is connected to the JDSU 10020484 single-sideband (SSB) modulator after polarization adjustment. The frequency of a Minicircuits ZX95-2500W voltage-controlled oscillator (VCO) is linearly chirped by applying a saw tooth waveform (generated by a Keithley 3390 waveform generator) to its control voltage. The VCO output drives the SSB modulator, chirping the frequency of the tunable laser. The SSB modulator output is amplified to about 30 mW and coupled into the chip. The beat-note between a secondary tunable laser and the SSB modulator output is used to monitor the performance of the SSB modulator. Figures 3.7(b) and 3.7(c) show the SSB modulator output spectra with zero biasing and with single-sideband operation biasing, respectively. Under the single-sideband operation condition, the undesired sideband and the optical carrier are significantly suppressed. The frequency of the optical signal is linearly chirped by about 800 MHz over 5 μs.

3.3 Nanophotonic chip characterization

As mentioned before, prior to imaging demonstration, the chip should be characterized to ensure its proper operation. In order to do so, the optical power distribution using the 1-D array shown in Fig. 3.4(a) is measured. Then, using a wired and a wireless measurement setup, the performance of the chip regarding properly delaying the received signals, both in through cables and wireless, is investigated. In his section, the optical power distribution and path loss is discussed to figure out how much optical power can be expected at each PD. Then, the electronic read-out circuits are shown. Finally, the results of these characterizations are presented.

3.3.1 Optical power distribution using the 1-D array and the optical path loss of the system

In the reported nanophotonic near-field imager, it is necessary for the output of each of the four ring modulators to be equally distributed among all 121 pixels to form a uniform image. In the proposed imager, first, two 1-D delay line arrays equally distribute the light among 11 columns (see Fig. 3.5(a)), and then, the same 1-D delay line array is used in each column to equally distribute the light among 11 photodiodes. The structure of the 1-D delay line array that was previously shown in Fig. 3.4(a), is repeated in Fig. 3.8(a), where a directional coupler is placed after each delay line. To achieve equal power distribution, the required coupling ratio for each directional coupler is calculated. Note that the directional couplers as well as the delay elements have non-ideal (less than 100%) transmission coefficient. For each coupler in Fig. 3.8(a), the top number denotes the percentage of the power guided to the next delay cell and the bottom number shows the amount of power coupled to the i^{th} output (C_i represents the i^{th} coupler). These coupling ratios are realized by adjusting the coupling length and spacing for each directional coupler. Figure 3.8(b) shows the microphotograph of the 1-D delay line array which was separately implemented on the same IME silicon-on-insulator run. The characterization result is shown in Fig. 3.8(c), where less than 2 dB variation across the

11 outputs is observed. Note that this variation is taken into account during a calibration phase before any imaging measurement.

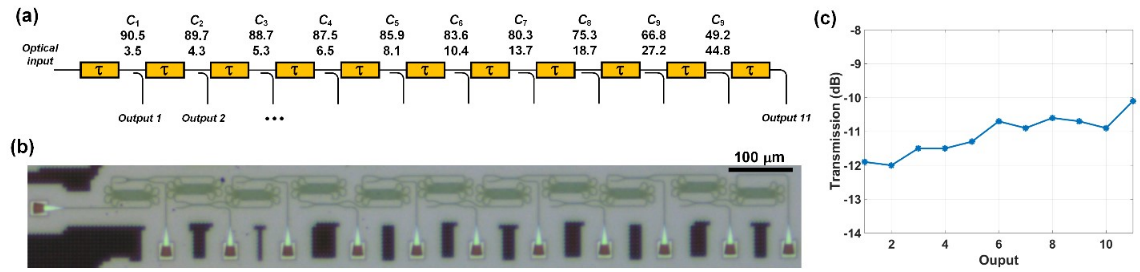

Figure 3.8 – 1-D delay line array. (a) Schematic of the delay line array with 11 outputs with the required coupling ratios that are chosen based on simulation results. (b) The microphotograph of the 1-D delay line array. (c) The measured optical power at the 11 outputs.

3.3.2 Total optical path loss

This transmission, or equivalently loss, is part of the total optical loss from the input grating coupler to any of the PDs (pixels). Figure 3.9 shows the block diagram of the photonic routing starting from the input grating coupler and ending to a photodiode. When a 15 dBm optical signal impinges on the grating coupler, each photodiode receives about -23 dBm (corresponding to a 38 dB power drop from the laser output to each photodiode). Out of this 38 dB power drop, 5 dB is due to the loss of the input on-chip grating coupler, 7 dB is due to the power distribution among the four ring modulators (6 dB due to two layers of Y-junction power splitters and 0.5 dB per Y-junction excess loss), 4 dB due to the optical insertion loss of the ring modulator, 11 dB due to power distribution among the columns (10.5 dB for distribution and 0.5 dB excess loss), and 11 dB due to power distribution among the photodetectors of each column (10.5 dB for distribution and 0.5 dB excess loss). Therefore, about 22 dB drop is due to the optical splitting from the output of a ring modulator to each photodetector.

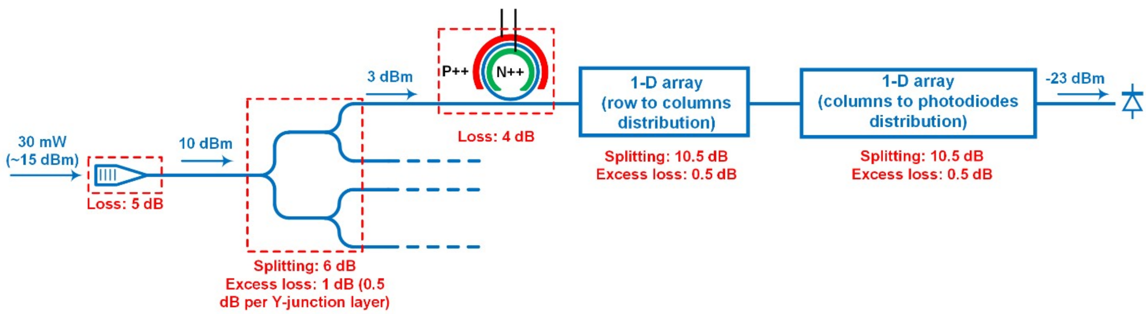

Figure 3.9 – Simplified block diagram illustrating the total optical loss from input grating coupler to each photodiode.

3.3.3 Data read-out and calibration

The implemented imager consists of 121 pixels as a matrix of 11x11 photodiodes as shown in Fig. 3.10(a). The current of these photodiodes can be read using a matrix read-out scheme. The anodes of the photodiodes in each row are connected to a row-select line and the cathodes of the photodiodes in each column are connected to a column-select line. By applying a voltage to a column-select line (while keeping the rest of the column-select lines open), the reverse biased current of each of the 11 photodiodes on that column flows though the corresponding row-select line, is converted to a voltage using a resistor (R_L), and power detected. By selecting the columns, one at a time, all 121 photo-currents can be read in 11 steps.

Since pixels are read one column at a time, in principle, 11 power detectors are required to detect the power of the pixels. However, the 11 parallel adjacent lines are highly susceptible to cross-talk and electromagnetic interference, which may result in a poor signal-to-interference ratio making the pixel read-out challenging. To alleviate this issue, a differential power detection scheme is used. Figure 3.10(b) illustrates the differential power detection circuit (three photodiodes are shown for simplicity), where 10 differential power detectors are used for 11 output channels to detect the relative power between the adjacent photodiodes. To form the image, these relative power measurements are used to estimate the power of each channel during the post-processing phase.

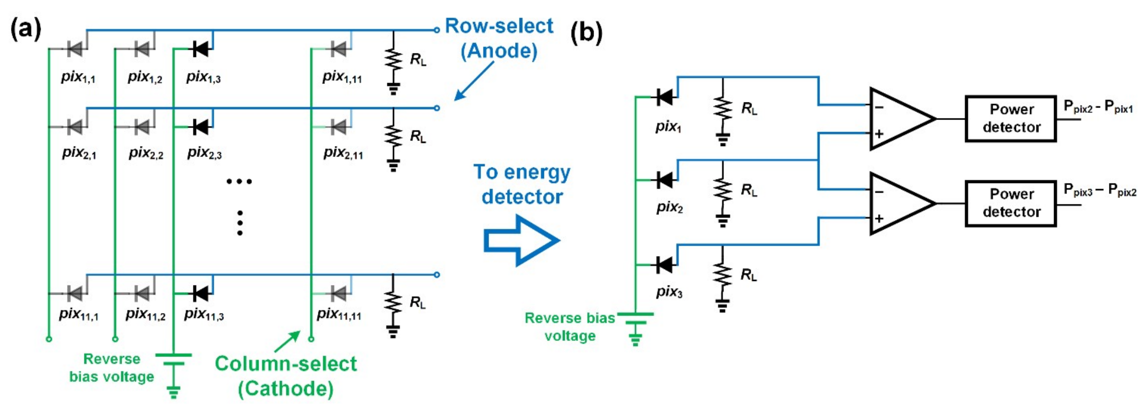

Figure 3.10 – Data read-out circuitry. (a) Matrix of photodiodes as imager pixels. (b) Differential energy detection circuit.

The calibration process that is explained next is used in all of the characterizations and imaging demonstration that are presented in the next sections. There are three main sources of error in the pixel read-out process that may affect the quality of the image: the cross-talk between the traces of the printed-circuit-board (PCB), the non-uniformity of the optical signal distribution, and the mismatch between the power detectors. The effect of these non-ideal factors is reduced through the calibration process. When both the input laser and the pulse generator are switched off, the power detectors should have a uniform response. However, in practice, the output voltage of the power detectors are not the same. To address this non-uniformity between the power detectors, first the output of the power detectors are measured while the laser and the pulse generator are off. The image in this case, $I_{light:off\ /\ pulse:off}$, represents the mismatch between the outputs of the power detectors and is referred to as $I_{non\text{-}uniform\_P\_detect}$. To measure the cross-talk between the PCB traces driving the ring modulators and those at the input of the power detectors, the power detector outputs are measured when the laser is off but the pulse generator is on. The result of this measurement, $I_{light:off\ /\ pulse:on}$, represents both the PCB cross-talk and the mismatch between the power detectors. In this case, the image representing the effect of the electrical PCB cross-talk can be calculated as

$$I_{cross-talk} = I_{light:off\,/\,pulse:on} - I_{light:off\,/\,pulse:off}\,. \tag{3.16}$$

Ideally, when the input laser is on, all pixels should receive the same amount of optical power. However, in practice, the input optical power may not be equally distributed among all pixels. The image formed for the case that the laser is on but the pulse generator is off, $I_{light:on\ /\ pulse:off}$, represents the effect of both non-uniform optical power distribution and the mismatch between the power detectors. In this case, the image representing the effect of the non-uniform optical power distribution can be calculated as

$$I_{non-uniformdist} = I_{light:on/\,pulse:off} - I_{light:off\,/\,pulse:off}\,. \tag{3.17}$$

For the final measurement, both the laser and the pulse generator are turned on. In this case, the formed image, $I_{light:on\,/\,pulse:on}$, represents the near-field image of the target object as well as the effect of non-uniform optical power distribution, the cross-talk between PCB traces, and the mismatch between the power detectors, that is,

$$I_{light:on/\,pulse:on} = I_{UWB\_image} + I_{non-uniformdist} + I_{cross-talk} + I_{non-uniform\_P\_detect}\,. \tag{3.18}$$

Therefore, using Eqns. (3.16), (3.17), and (3.18), the near-field image of the target object can be calculated as

$$I_{UWB\_image} = I_{light:on/\,pulse:on} - I_{light:on/\,pulse:off} - I_{light:off\,/\,pulse:on} + I_{light:off\,/\,pulse:off}\,. \tag{3.19}$$

Note that for each measurement in the characterization and imaging setups, the three calibration measurements are performed once and the three calibration images are stored and used for image formation.

3.3.4 Wired Characterization

The ultimate purpose of designing this system is to perform near-field microwave imaging. However, before getting there, the chip should be characterized to experimentally validate the concept of optically delayed electrical pulses used in the proposed solution to coherently combine the pulses at each pixel (by sweeping the frequency of the laser).

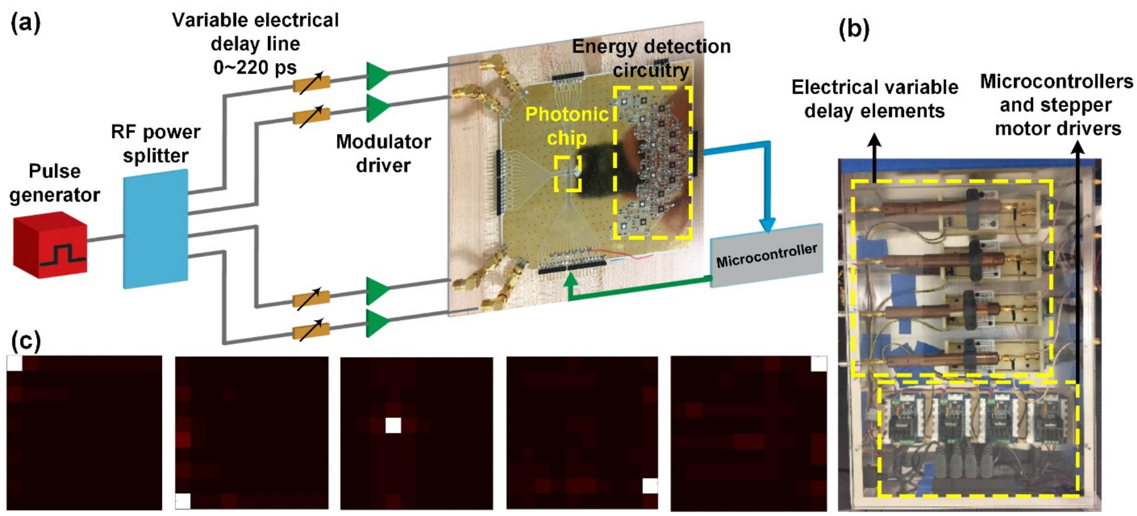

Figure 3.11 – (a) Wired measurement setup for characterization of the imager chip. (b) The 4-channel digitally controlled electrical variable delay line. (c) Wired measurement results showing a bright pixel at different locations for different electrical delay settings emulating different angles of incidence.

In demonstration of near-field imaging, the input signal to the chip is wirelessly received by using UWB antennas. Therefore, to ensure the proper performance of the chip itself, it is desired to first, apply the input signals using cables rather than antennas. Figure 3.10(a) shows the measurement setup for wired characterization of the nanophotonic imager chip. The output of an Avtech AVE2-C-5000 UWB pulse source generating 200 ps wide monocycles (with a frequency spectrum spread from 0.5 GHz to 5 GHz) is split into four branches using a RF power splitter. A 4-channel digitally controlled electrical variable delay line is used to independently adjust the delay of each channel between 0 to 220 ps with a resolution of 0.06 ps. Figure 3.10(b) shows the implemented 4-channel variable delay line system that can be mechanically adjusted using stepper motors. This system provides a per-channel delay with an insertion loss of less than 2 dB across the bandwidth of interest, emulating an UWB signal impinging with different incidence angles.

An array of power detectors are used to differentially read and detect the power of the pixels forming an 11x11 image after processing as explained in Section 3.3.1. Figure 3.10(c) shows the formed images for five different delay settings emulating five different angles of incidence. This measurement shows that individual pixels can be illuminated within the imager output. Note that Fig. 3.10(c) shows the results after the calibration phase explained in Section 3.3.3.

3.3.5 Wireless characterization

In the wired measurements, the performance of the chip when receiving signals with different delays was studied. Now, the characterization can be performed using a wireless setup where the input pulses are received wirelessly and applied to the chip. The measurement setup used for wireless characterization of the imager is shown in Fig. 3.11(a). Here, the goal is to use a single transmitter antenna such that only one pixel of the imager "turns on". A 2x2 array of UWB Knight's helm printed circuit board (PCB) antennas [73] are used to receive the UWB pulses. The incoming signal is a monocycle pulse whose frequency spectrum covers a range of about 500 MHz to 5 GHz. Therefore, the bandwidth of these antennas should be large enough to preserve the shape of the pulse. The antenna dimensions are optimized for operation in the 500 MHz to 5GHz range. Figure 3.11(b) shows the fabricated antenna implemented on a FR4 printed circuit board.

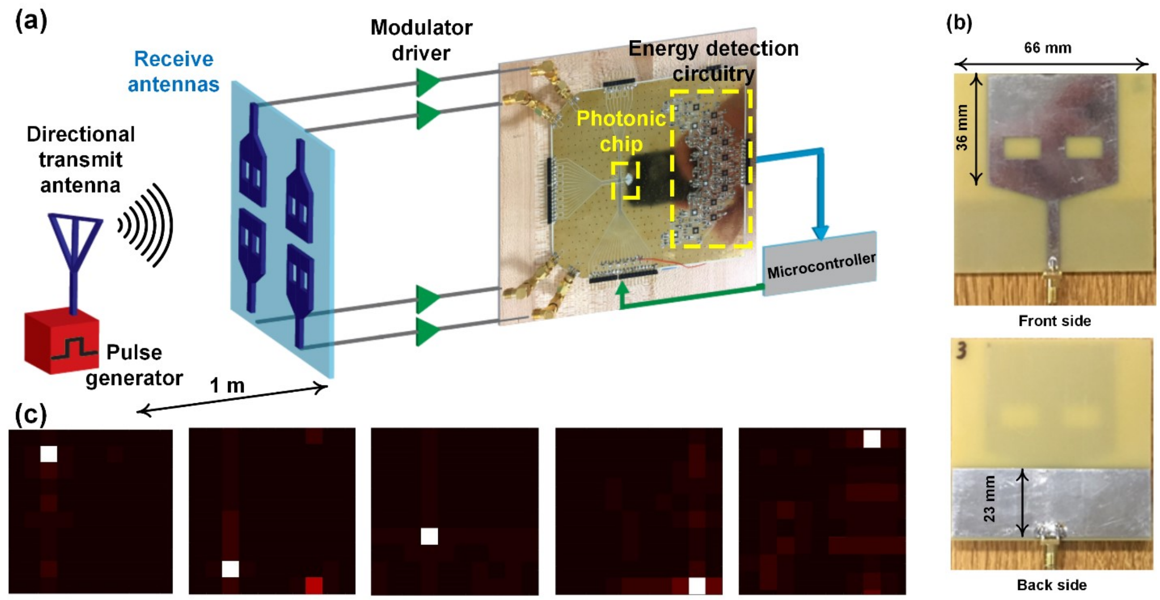

Figure 3.12 – (a) Wireless measurement setup. (b) Wireless measurement results for five different angles of incidence, where a pixel for each case is illuminated.

The UWB pulse generator drives a wideband antenna transmitting pulses towards the imager. The impinging signals are received using a 2x2 antenna array (with 7 cm spacing), amplified, and fed to the input of the imager chip. To minimize the undesired reflections and the effect of the electromagnetic interference, the measurement setup is placed inside a shielded anechoic chamber. The distance between the transmit antenna and the receive antenna array is set to about 1 mA.

Figure 3.11(c) shows the images formed for five different angles of incidence. These results show that in depending on the angle of incidence, a corresponding pixel turns on. The same experiment has been done using two transmit antennas to illuminate two pixels.

These results are required to show that when an object is to be imaged, the system is actually capable of resolving signals coming from different parts of the object. Note that Fig. 3.10(c) shows the results after the calibration phase explained in Section 3.3.3.

3.4 Imaging demonstration

The nanophotonic imager chip was used to demonstrate microwave near-field imaging. Figure 3.13(a) shows the near-field imaging setup. In this figure, the target object which is made of aluminum tapes, is illuminated using an UWB monocycle pulse train with a pulse repetition rate of 1 MHz. The reflected UWB pulses from the target object placed at a distance of about 0.5 m are received by the 2x2 antenna array of the imager. The antennas are the same as Fig. 3.12(b). The antenna signals are amplified and connected to the ring modulators on chip. After processing the signals using the on-chip true-time delay network followed by post processing, the corresponding 11x11 near-field image of the target object is formed. To demonstrate the near-field imaging performance, a 24 cm x 24 cm metallic square, a metallic surface with a 24 cm x 24 cm square hole at its center, and the UPenn logo with a metallic surface were used as the target objects. Note that the dimensions of the target objects and their distance to the imager are chosen to ensure that the entire object is within the imager field-of-view. The transmit antenna, the target object, and the receive antenna array are placed inside a shielded anechoic chamber. Figure 3.13(b) shows the 11x11 UWB near-field images of the target objects. The read-out circuitry and the calibration process are the same as what was explained in Section 3.3.3.

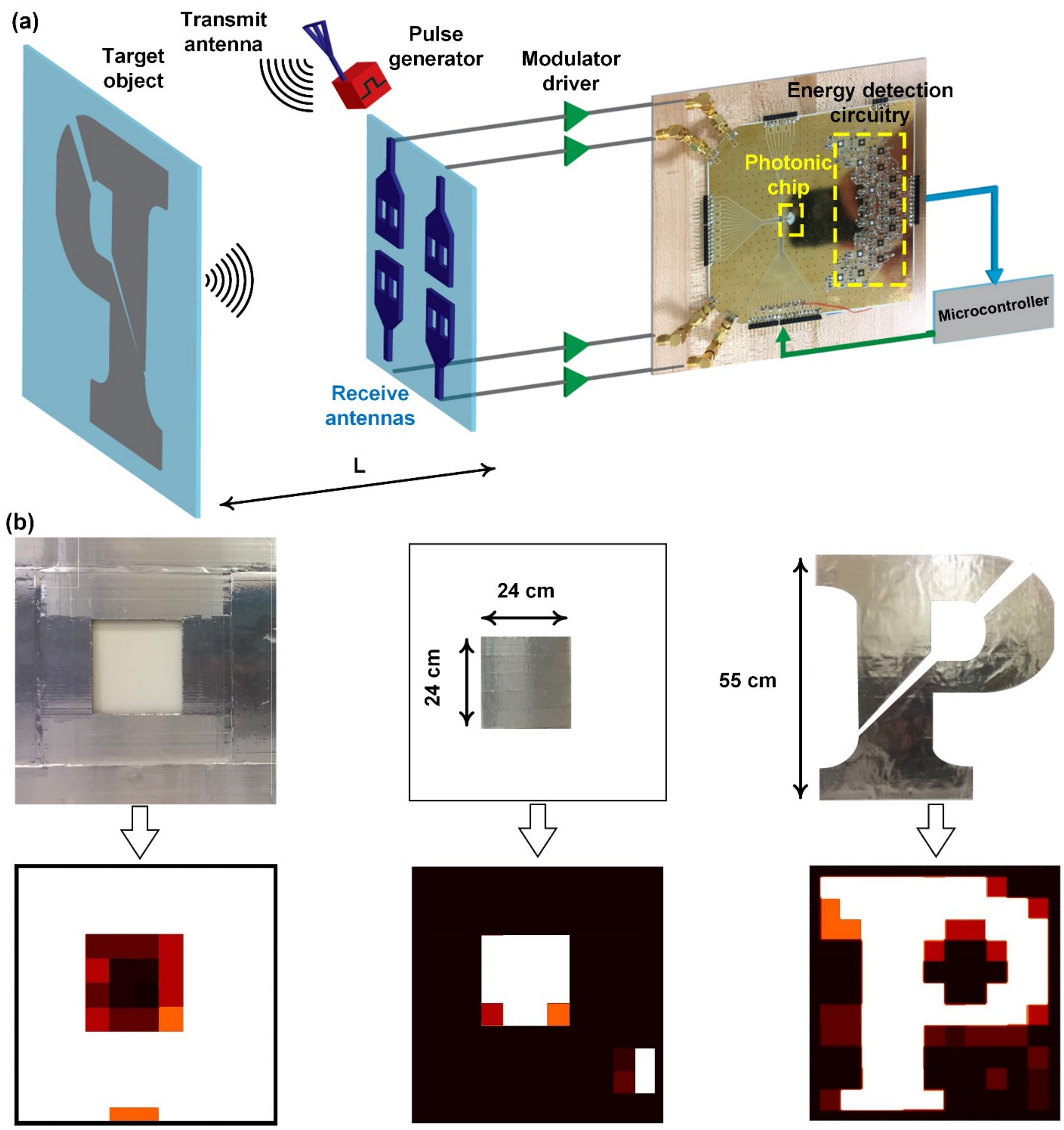

Figure 3.13 – (a) Near-field imaging results. (a) Imaging measurement setup. (b) Three target objects and their near-field images formed using the implemented nanophotonic imager are shown.

3.5 Imager noise performance and linearity

There are a few important parameters for any receiver that should be measured to figure out the incoming signal characteristics required for the system to work properly. Among those, noise figure, linearity (in terms of IIP3) and dynamic range, and sensitivity are the most common ones. In this section, the calculations of these parameters are presented.

3.5.1 Noise figure of the system

Figure 3.14 shows the simplified block diagram of the RF front-end of the imager system that is used for noise figure calculations. Based on this figure and using the Friis equation [74], the noise factor, *F*, for a single received UWB pulse can be calculated as

$$F \approx F_1 + \frac{F_2 - 1}{G_1} + \frac{F_3 - 1}{G_1 G_2}, \tag{3.20}$$

where $F_1, F_2, G_1,$ and G_2 are the noise factors of the first and second amplifiers and the gain of the first and second amplifiers, respectively, and F_3 is the noise factor of the electro-optic system (with electrical voltage to the ring modulator as the input and the electrical current of the photodiode as the output). Note that, as an important advantage of UWB pulse receivers, the system noise factor can be improved significantly by integrating (averaging) many pulses within the integration time (also referred to as exposure time) [75]. In this case, since the received pulses are correlated while the noise is uncorrelated, the SNR improves by a factor of N, where N is the number of received pulses averaged within the integration time. As a result, Eq. (3.20) is re-written as

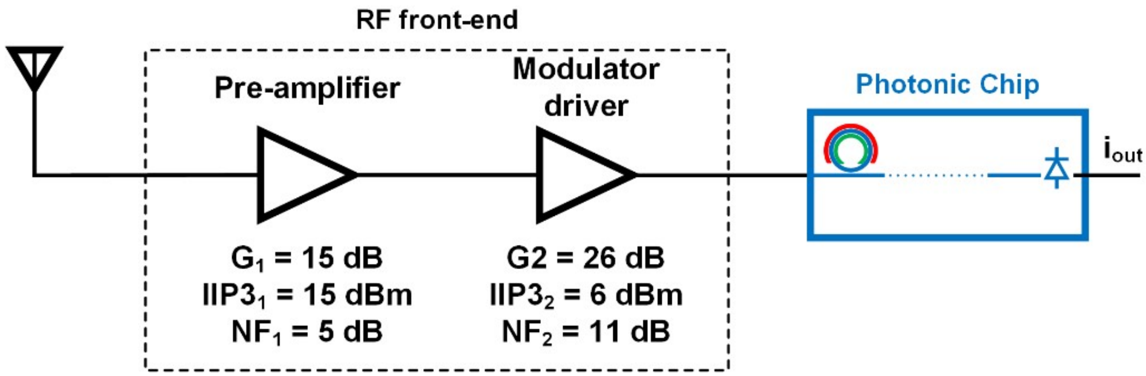

Figure 3.14 – Schematic of the RF front-end of the UWB imager.

$$F \approx \frac{1}{N}\left(F_1 + \frac{F_2 - 1}{G_1} + \frac{F_3 - 1}{G_1 G_2}\right). \tag{3.20}$$

The noise factor of the electro-optic system is written as

$$F_3 \approx 1 + \frac{1}{|G_3|^2}\left(\frac{\overline{i_{PD,shot}^2}}{\overline{V_{R_s}^2}}\right), \tag{3.21}$$

where G_3 is the trans-conductance gain from the photocurrent output to the input voltage of the ring modulator (this gain is much smaller than unity), $\overline{i_{PD,shot}^2} = 2qi_{out,DC}$ is the power spectral density of the photodiode shot noise, and $\overline{V_{R_s}^2}$ is the power spectral density of reference voltage noise at the modulator input (for $R_s = 50\Omega$ and no complex conjugate matching). For the implemented imager system, when the optical power at the input of a ring modulator is set to 3 dBm and the modulator is driven with a 7V (peak-to-peak) input UWB pulse, a 2.5 μA pulse is detected at the output of each photodiode. Therefore, for measured $G_3 = \frac{2.5\times10^{-6}}{7}\frac{A}{V}$ and measured $i_{out,DC} \approx 10\mu A$ at room temperature can be calculated. For the imaging measurements, the pulse repetition rate is set to 1 MHz and the integration time is set to 1 ms, which results in N=1000. Therefore, using the parameters shown in Fig. 3.14 and Eq. (3.20) and (3.21**), the total noise figure of the system can be calculated as *3.8 dB***. Note that without factor of 1000 averaging, the noise figure of the system is about 33.8 dB.

3.5.2 Dynamic range and sensitivity

Here the spurious-free dynamic range (SFDR) and the sensitivity of the imager are studied. SFDR is a measure of the main signal to the spurious signals that eventually can be used to find the sensitivity of the system, *i.e*. the smallest detectable input signal to the system. To calculate the SFDR, first, the system IIP3 should be calculated, which can be written as

$$\frac{1}{IIP3} \approx \frac{1}{IIP3_1} + \frac{G_1}{IIP3_2} + \frac{G_1 G_2}{IIP3_3}, \tag{3.22}$$

where $IIP3_1, IIP3_2$, and $IP3_3$ are the 3rd-order input intercept point of the first and second amplifiers, and the 3rd-order input intercept point of the ring modulator, respectively. Using the method discussed in [76], the $IP3_3$ for our ring modulator is calculated as 38 dBm. In this case, the total system ***IIP3* ≈ -10 dBm** is calculated.

The SFDR can be calculated as [74]

$$SFDR = \frac{2\left(IIP3 + 174dBm - NF - 10\log BW\right)}{3} - SNR_{\min} + 10\log\left(N\right), \tag{3.23}$$

Where $SNR_{\min}$ is the minimum desirable SNR for image detection, BW is the bandwidth of the system (5 GHz in this case), and $10\log\left(N\right)$ represent the SNR improvement due to the averaging. In this case, for a $SNR_{\min}$ of 10 dB and N = 1000, the ***SFDR of 64.8 dB*** is calculated.

Moreover, the sensitivity can be calculated as [74]

$$P_{sen} = -174dBm + NF + 10\log BW + SNR_{\min} - 10\log\left(N\right). \tag{3.24}$$

Based on this equation, the imager has a sensitivity of about -93 dBm can be estimated.

3.6 Summary and Future works

In this section, the demonstration of the first nanophotonic near-field imager chip was presented, where compared to the state-of-the-art all-electrical designs, the on-chip photonic delay lines are more than 44 times smaller, achieve significantly lower propagation loss, and are immune to the electromagnetic interference, making the proposed nanophotonic imager scalable to an imager with a large number of pixels. This work is an example of optical processing of electrical signals that results in more efficient (area and energy) systems. The chip was completely characterized prior to performing imaging using wired and wireless setups. Imaging of multiple objects was performed. Table 3.1 summarizes the specifications of the implemented near-field imager.

Table 3.1 – Implemented nanophotonic near-field imager performance summary

Number of pixels	**11x11**
Delay resolution	**9.8 ps**
Spatial resolution	**4.8°**
Field of view	**±27°**
Delay element dimensions	**40 μm x 90 μm**
Photonic chip dimensions	**2.2 mm x 2.1 mm**
Fabrication process	**IME 180nm SOI**

In future, the pulse width of the UWB signal can be reduced by increasing the signal spectral bandwidth enabling near-field imaging of smaller objects at a higher resolution. The high bandwidth of the ring modulators and SiGe photodiodes enable the implemented nanophotonic imager chip to be used for near-field imaging in mm-wave regime without any modifications.

The implemented nanophotonic near-field imager can be scaled to an imager with a very large number of pixels using the tiling scheme, where multiple imagers with smaller pixel counts can be placed next to each other to form an imager with a large pixel count. To increase the number of pixels of the integrated nanophotonic near-field imager, the number of the delay elements in the 1-D array of delay lines in Fig. 3.8(a) can be increased.

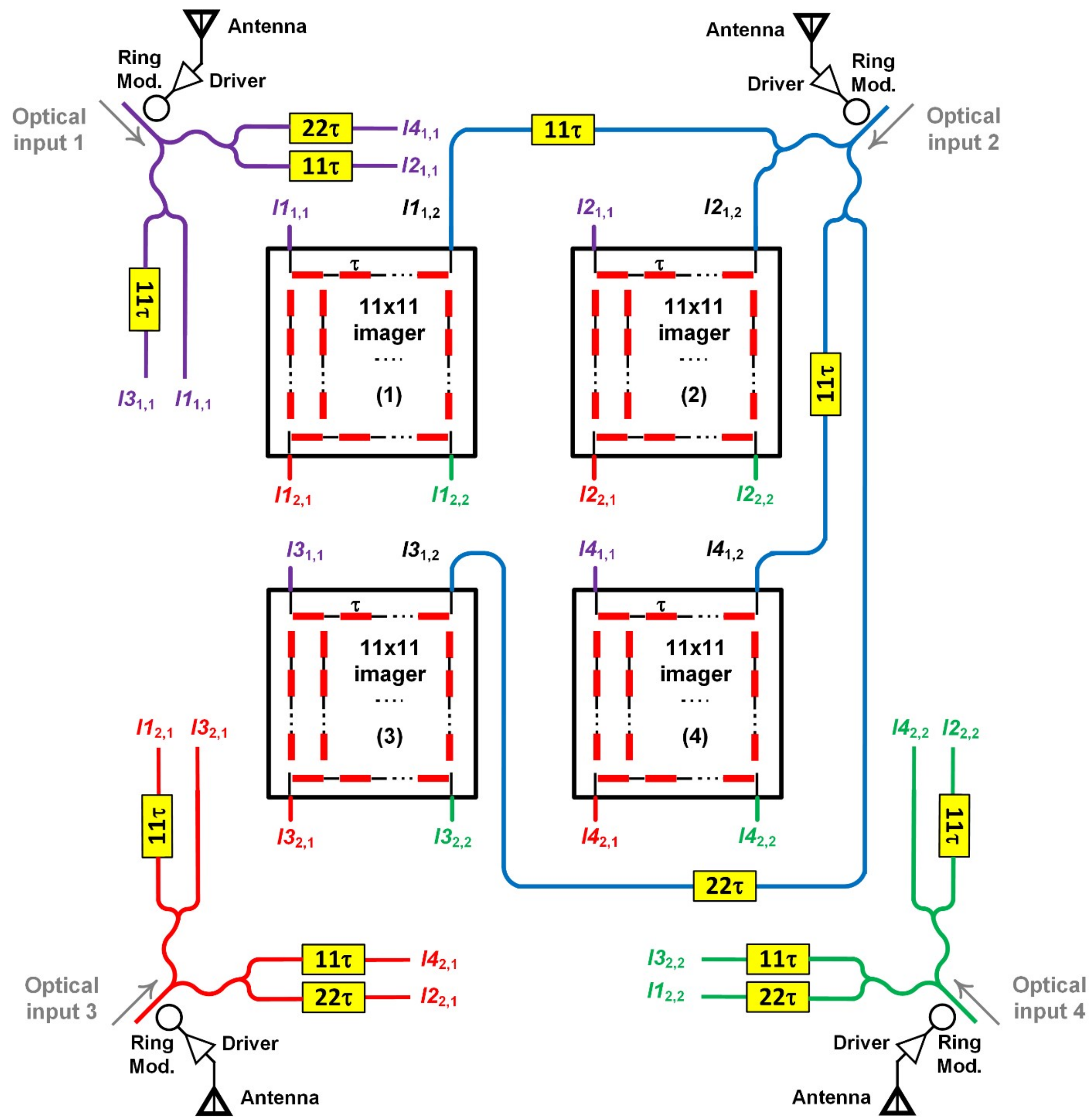

Figure 3.15 – Scaling the number of pixels by tiling.

In this case, the directional couplers (with varying coupling length and gap), placed between the delay lines, need to be designed to ensure equal power at the output of the directional couplers. For a given minimum feature size of a photonic process, the design of the directional couplers for a delay line array with large number of elements may be challenging since the required coupling length/gap difference between two consecutive directional couplers (to ensure equal output power) may become smaller than the minimum feature size. Alternatively, a practical approach for scaling to a large number of pixels is the tiling scheme, where multiple imagers with smaller pixel counts can be placed next to each other to create an imager with a large number of pixels. Figure 3.15 illustrates an example of this idea, where four identical 11x11 imagers are placed next to each other to form a 22x22 imager. In this case, the UWB signal received by each antenna is used to modulate the input light using ring modulators. The modulator outputs are guided to all four 11x11 imagers. The modulated light is routed to the closest 11x11 imager with no extra delay. However, to route the same signal to other imagers, extra delays are added to account for the total delay of the closer imagers.

Moreover, the electrical bandwidth of the chip is mainly limited by the photodiode and the ring modulator (about 30 GHz). This indicates that the same architecture can be used for imaging at higher frequencies. Using existing modulators with larger bandwidth, the proposed imager can be used for microwave imaging at frequencies of tens of GHz with some minor modifications of the read-out circuit bandwidth. This is an important advantage compared to the electrical solutions where the large loss of the delay cells as well as the power consumption of repeating amplifiers at high frequencies make their design very challenging (as discussed in Section 3.1.1).

CHAPTER 4

Optical beam steering: Towards half-wavelength element spacing optical phased arrays

A phased array is composed of multiple transmitting or receiving antennas (elements), in a 1-D or 2-D form, that is capable of sending or receiving signal from a certain direction. This is achieved by accurately controlling the relative phase between the elements. This is desired in many applications since it eliminates the need for any mechanical movement to steer the beam. Figure 4.1 shows a 1-D phase array in which the signal source is connected to eight phase shifters followed by eight antennas. If the relative phases between the antennas are set properly, their radiated signals will coherently interfere along a specific direction. In this figure, the signal in each path experiences a certain amount of phase shift, *i.e.* $\Delta\phi$, relative to the path above it, resulting in transmitting signal in the direction shown in Fig. 4.1.

Two important design criteria that are typically considered in designing the phased arrays are the array aperture size and the element to element spacing. The former affects the width of the far-field beam and the latter the amount of the power radiated in the radiation lobes other than the main lobe (i.e. side-lobes) as well as the steering range.

Typically, antenna arrays are analyzed using the concept of array factor [77]. It can be shown that for an N-element linear array like the one shown in Fig. 4.1, the total electric field in far-field can be written as

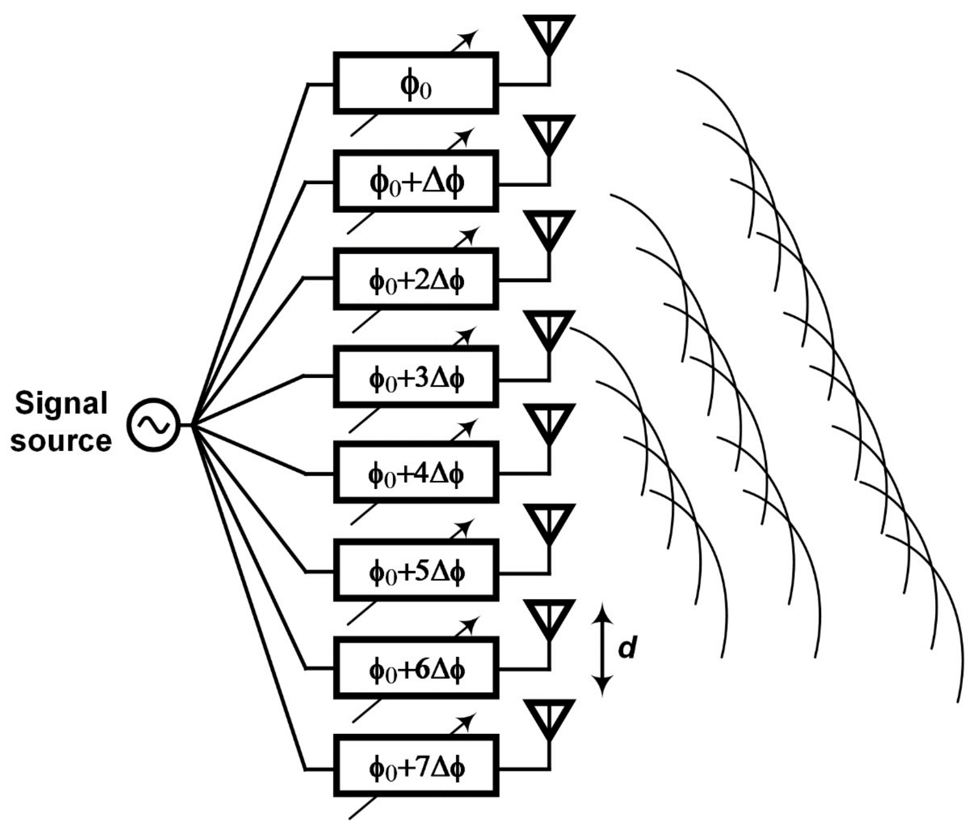

Figure 4.1 – Simplified block diagram of a 1-D phased array consisting of 8 antennas.

$$\mathbf{E}(\text{total}) = [\mathbf{E}(\text{single element at reference point})] \times [\text{array factor}] \tag{4.1}$$

Effectively, by calculating the electric field pattern of a single element placed at the reference point and multiplying it by the array factor, the far-field interference pattern of the antenna array can be calculated. The array factor (*AF*) in Eq. (4.1) can be written as [77]

$$AF = \sum_{k=1}^{N} e^{j(k-1)\frac{2\pi n}{\lambda} d \sin\theta + \Delta\phi}. \tag{4.2}$$

where $N, n, \lambda, d, \theta,$ and $\Delta\phi$ are the number of antennas (elements), index of refraction of the medium, wavelength of the signal in free space, array element spacing, spatial steering angle, and relative phase between the elements, respectively. The far-field beam intensity is proportional to the magnitude of *AF* in Eq. (4.2). Therefore, the beam pattern can be plotted for different array sizes and element spacing as shown in Fig. 4.2.

Figure 4.2(a) shows the effect of the number of elements on the beam width for the case that all elements are radiating in-phase. As the number of elements increases, the beam width decreases, resulting in the energy being focused on a specific point. In applications where spatial high-resolution is required, large number of elements are required.

Figure 4.2(b) shows beam pattern for different relative phases and element spacing (factor of wavelength) plotted in polar coordinates for an 8-element linear phased array (N=8). It shows how beam steering can be performed by setting the relative phases ($\Delta\phi$). Moreover, the graphs show the effect of element spacing on the power transmitted in the side-lobes. From these results, ideally, if the adjacent elements are placed at half-wavelength distance from each other, all of the side-lobes can be eliminated. In addition, the spatial range, or field-of-view (FOV), of the phased array can be improved by reducing the element spacing. Therefore, in order to have a high spatial resolution beam steering with maximum FOV and side-lobe suppression ratio, a phased array with large number of elements placed at half-wavelength should be designed.

Phased arrays have been implemented in different regimes. In the microwave regime, phased arrays have various applications in communications [78], radar systems [79], and wireless power transfers [80], to name a few. In these systems, microwave antennas, acting as the elements of the phased array, are designed for the frequency band of interest and placed next to each other in a 1-D or 2-D architecture. Since in RF and microwave domains the signal wavelengths are in the order of a few millimeters to tens of centimeters, achieving half-wavelength element spacing is not a challenging task.

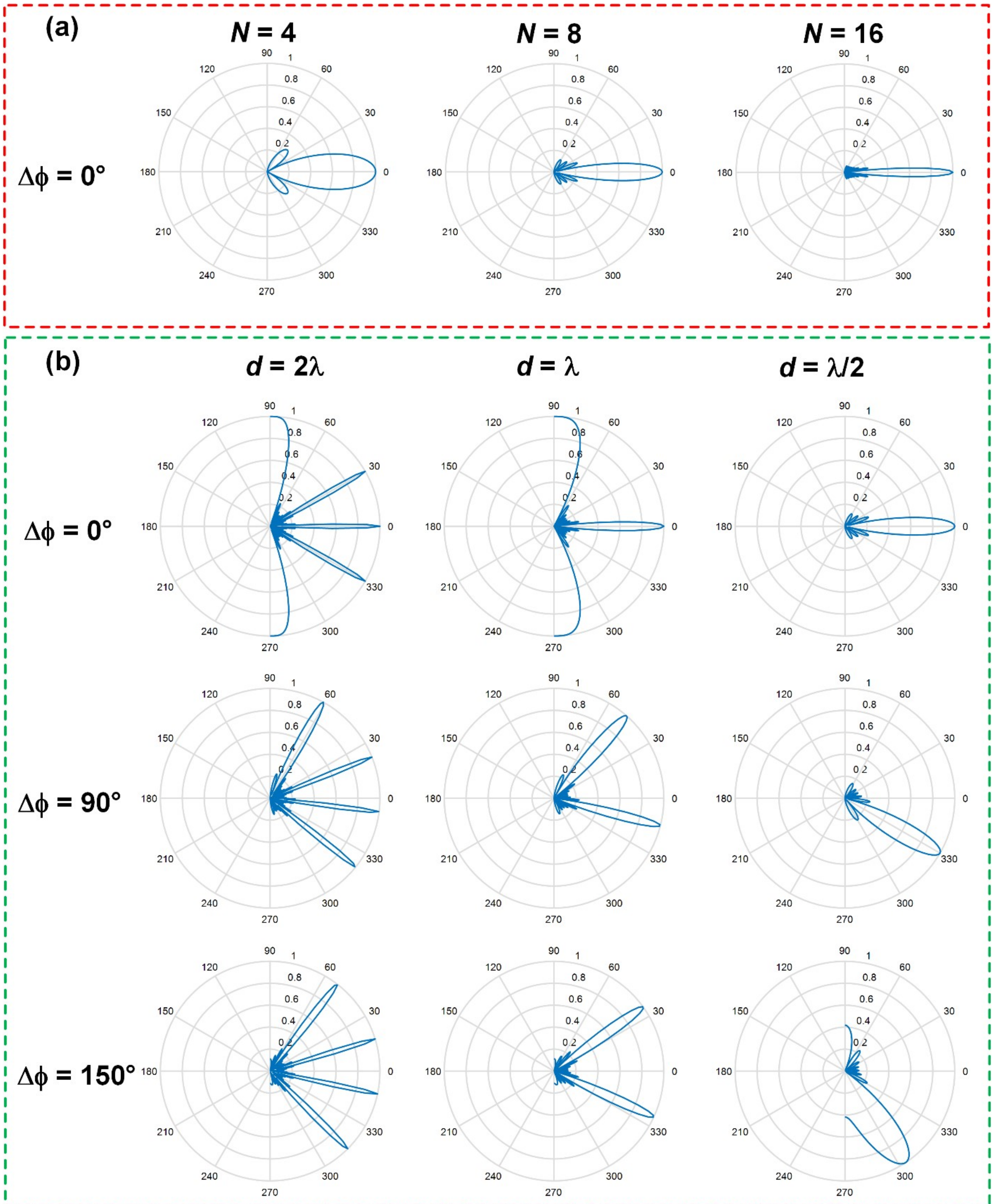

Figure 4.2 – (a) Beam width comparison for different number of array elements. (b) Beam steering by changing the relative phases for different element spacings.

In optical regime, optical phased arrays (OPA) have many applications such as in optical communications [81], LiDAR systems [82-84], projection systems [85], and 3-D imaging [86]. In such systems, the far-field beam is formed and steered by controlling the relative phases between optical elements within the array aperture. To form a narrow beam with a large side-lobe suppression ratio, which is steerable over a large field-of-view, a large number of closely placed elements (ideally with element spacing approaching half of the wavelength) within a large aperture is required. However, in contrast with the microwave phased arrays, this is a very challenging task. Especially, achieving half-wavelength element spacing is extremely difficult since the wavelength in the infrared regime (commonly used in the above mentioned applications) is about 1 μm, resulting in sum-micron element spacing.

Benefiting from integrated photonic platforms, a number of OPAs have been demonstrated [82-95]. In the conventional implementation of a 2-D NxN element OPA, N^2 phase shifters are used to perform per-element optical phase adjustment [82-85,87,88]. This results in a large power consumption in a conventional 2-D OPA with per-element phase shifters and makes the optical and electrical routing within the array aperture rather challenging. The typical size of the optical elements of few microns and the complex photonic routing have made realization of ultra-compact OPAs an open problem.

In 2-D OPAs with grating based elements (e.g. grating couplers), this challenge can be to some extent addressed by steering the beam in one dimension through adjusting the relative phases between the elements, while using wavelength tuning for beam-steering in the other dimension [92-95]. Despite excellent beam-steering results, this method requires a highly tunable laser (over a large wavelength range) and typically achieves a smaller steering range through wavelength tuning compared to the relative phases adjustment between the OPA elements.

In this chapter, we present a novel solution to address the previous challenges in designing ultra-compact OPAs. In the proposed scheme, the N^2 phase shifters in an N×N OPA are reduced to only 2N phase shifters to properly set the phase of the rows and columns and therefore, to set the relative phase between adjacent elements. To demonstrate this idea, an 8×8 OPA chip was implemented on a silicon photonic process and 2-D beam steering has been shown. This design significantly reduces the routing complexity as well as power consumption of the OPA and enables more compact OPAs. Then, a novel implementation architecture is proposed that benefits from a fabrication process with two photonic routing layers. Using this process together with the reduced complexity offered by the use of only 2N phase shifters and also designing compact elements, a new 8×8 OPA chip was implemented that features 3 μm element spacing which is 3 times smaller than the state-of-the-art.

The rest of the chapter is organized as follows. Section 4.1 presents the idea of reducing the number of phase shifters, the theory of operation of the proposed architecture including using 2N phase shifters and designing compact waveguide grating elements, and the 8×8 OPA as a proof of concept. Section 4.2 is dedicated to the second step of implementing an ultra-compact OPA using a process that offers two-layer photonic routing. Finally, Section 4.3 summarizes this chapter and presents some of the possible future works.

4.1 Reducing the number of phase shifters

This section presents the idea of an NxN OPA with 2N phase shifters. The theory behind the proposed architecture discussed and an 8x8 OPA is designed and implemented as a proof of concept.

4.1.1 Theory of operation

In an OPA, the beam forming and steering is performed by controlling the relative phases between the elements. Figure 4.3(a) shows the structure of the proposed NxN OPA, where N nanophotonic waveguides serving as rows cross N nanophotonic waveguides serving as columns. Consider the case that the electric field of optical wave entering the m^{th} row is written as $E_m = a_m e^{j\phi_m}$, and the electric field of optical wave entering the n^{th} column is written as $E_n = b_n e^{j\theta_n}$ where a_m, b_n, ϕ_m, and θ_n are the amplitude of the optical field in the m^{th} row, the amplitude of the optical field in the n^{th} column, the phase of the optical signal in the m^{th} row, and the phase of the optical signal in the n^{th} column, respectively. Note that the term $e^{j\omega_0 t}$, representing the optical frequency of the signal, is dropped for simplicity. Before the crossing point of the m^{th} row and the n^{th} column, two directional couplers with varying coupling ratio followed by a Y-junction are used to combine a fraction of the light from the m^{th} row with a fraction of the light from the n^{th} column. The Y-junction output is connected to a grating coupler, GC_{mn}, acting as the OPA element. The length of each directional coupler as well as the etch level in the coupling region is adjusted to ensure all grating couplers receive the same power. The electric field at the input of GC_{mn} is written as

$$E_{mn} = \frac{1}{\sqrt{N}} \sqrt{\left(a_m^2 + b_n^2 + 2a_m b_n \cos(\phi_m - \theta_n)\right)} \exp\left[j \tan^{-1}\left(\frac{a_m \sin\phi_m + b_n \sin\theta_n}{a_m \cos\phi_m + b_n \cos\theta_n} \right) \right]. \tag{4.3}$$

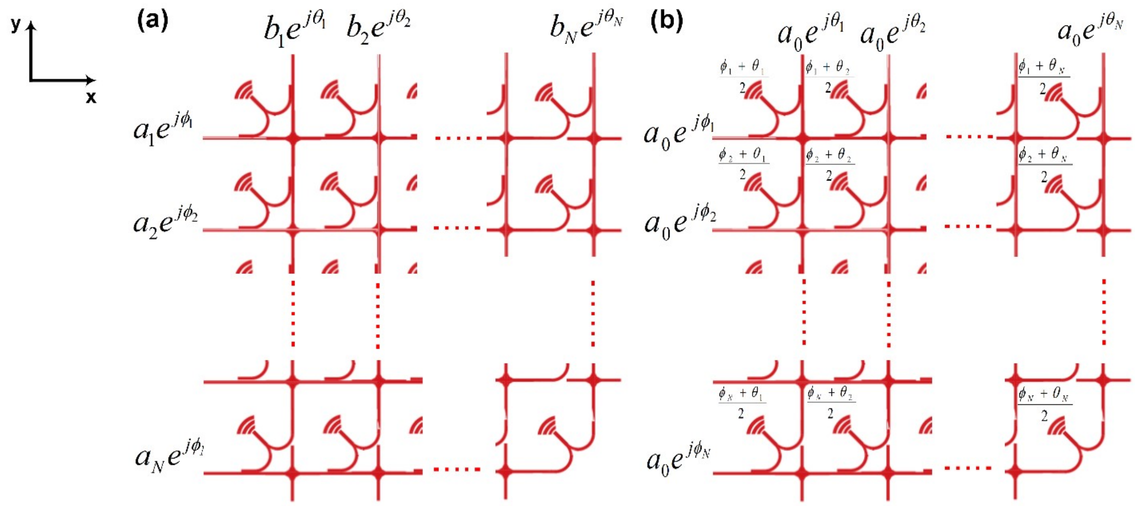

Figure 4.3 – Conceptual schematic of the proposed NxN OPA, where optical signals traveling in the row and column waveguides have (a) different phases and amplitudes and (b) different phases but the same amplitude.

In this case, the relative phase between GC_{mn} and $GC_{\mathrm{(m+1)n}}$ can be written as

$$\Delta\phi_{m+1,m,n} = \tan^{-1}\left(\frac{a_{m+1} \sin\phi_{m+1} + b_n \sin\theta_n}{a_{m+1} \cos\phi_{m+1} + b_n \cos\theta_n} \right) - \tan^{-1}\left(\frac{a_m \sin\phi_m + b_n \sin\theta_n}{a_m \cos\phi_m + b_n \cos\theta_n} \right). \tag{4.4}$$

Similarly, the relative phase between GC_{mn} and $GC_{\mathrm{m(n+1)}}$ can be written as

$$\Delta\theta_{m,n+1,n} = \tan^{-1}\left(\frac{a_m \sin\phi_m + b_{n+1} \sin\theta_{n+1}}{a_m \cos\phi_m + b_{n+1} \cos\theta_{n+1}} \right) - \tan^{-1}\left(\frac{a_m \sin\phi_m + b_n \sin\theta_n}{a_m \cos\phi_m + b_n \cos\theta_n} \right). \tag{4.5}$$

Equations (4.4) and (4.5) indicate that the relative phase between adjacent elements can be set by adjusting the amplitude and phase of the optical waves in row and column waveguides outside the aperture. Note that the phase of the individual element cannot be independently set. However, the relative phase between the adjacent elements in the X and Y directions (in Figs. 4.3(a) and 4.3(b)) can be set to any value between 0 and 2π radians, enabling formation of a beam that can be steered in X and Y directions independently. For the case that $a_m = b_n = a_0$ (Fig. 4.3(b)), Eq. (4.3) can be simplified as

$$E_{mn} = \frac{2}{\sqrt{N}} a_0 \left| \cos\left(\frac{\phi_m - \theta_n}{2} \right) \right| e^{j\left(\frac{\phi_m + \theta_n}{2}\right)} \tag{4.6}$$

In this case, the relative phase between the adjacent elements in rows and columns can be written as

$$\Delta\phi_{m+1,m,n} = \frac{\phi_{m+1} - \phi_m}{2}. \tag{4.7}$$

$$\Delta\theta_{m,n+1,n} = \frac{\theta_{n+1} - \theta_n}{2}. \tag{4.8}$$

In order to perform 2-D beam-steering, the relative phase between all adjacent elements in rows and also all adjacent elements in columns are set to the same values

$$\Delta\phi_{m+1,m,n} = \Delta\phi. \tag{4.9}$$

$$\Delta\theta_{m,n+1,n} = \Delta\theta. \tag{4.10}$$

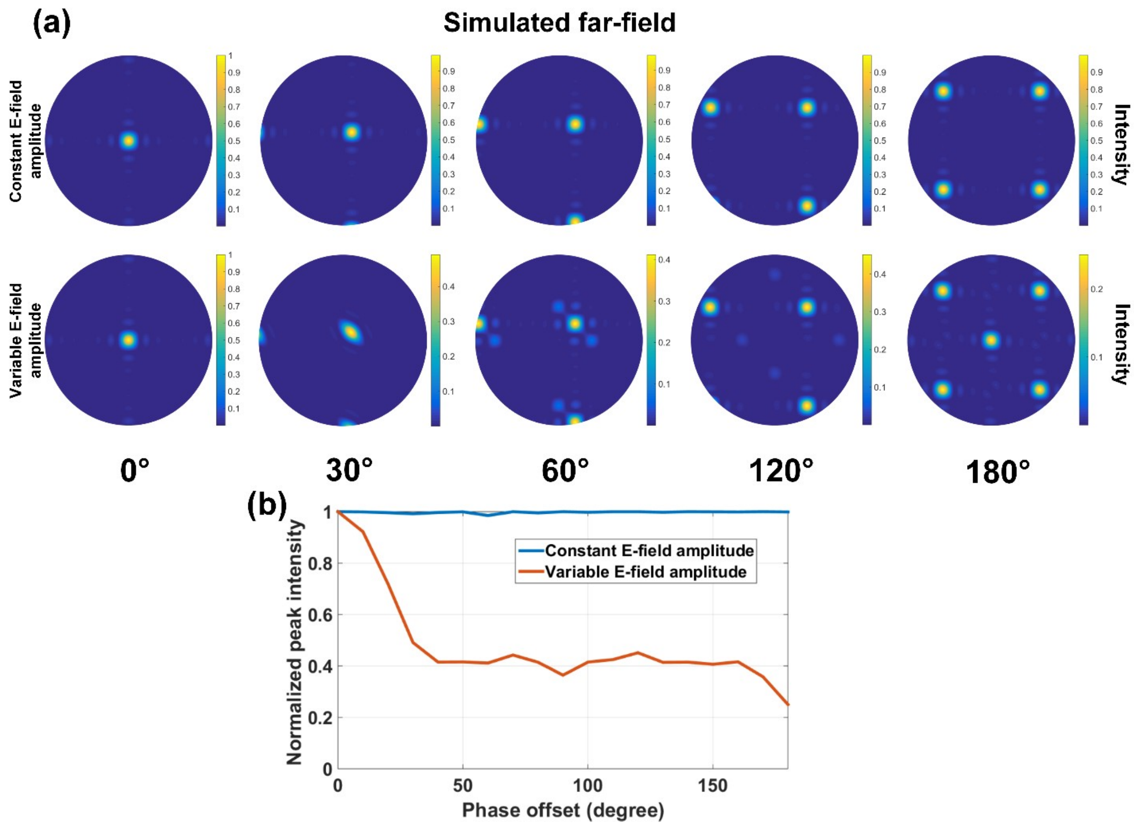

Figure 4.4 – (a) The far-field interference pattern of an 8x8 OPA with 64 per-element phase control (top row) and that of an 8x8 OPA with identical element structure and spacing but implemented based on the proposed architecture (bottom row). The diagonal beam-steering (with same relative phase between the elements in rows and columns) is performed. (b) The peak intensity of the main lobe in the far-field pattern for the conventional and proposed 8x8 OPAs.

Therefore, 2N phase shifters can be used to perform 2-D beam-steering for an NxN OPA, which significantly reduces the power consumption for an OPA with a large number of elements, while eliminating the electrical routing within the aperture. Furthermore, moving the phase shifters outside of the aperture enables smaller element spacing for a 2-D phase array.

In Eq. (4.6), the amplitude of the electric field at GC_{mn} is proportional to the term $\left|\cos\left((\phi_m - \theta_n)/2\right)\right|$. Therefore, the light emission intensity from grating couplers may be lower than the conventional 2-D OPAs, where per-element phase shifters (with low phase dependent insertion loss) are used.

To study the performance of the proposed 2-D OPA and also investigate the effect of the aforementioned phase dependent amplitude variation on the beam forming and steering, the Fraunhofer far-field approximation [96] is used to calculate the far-field interference pattern of an 8x8 OPA implemented based on the proposed architecture (with 16 off-aperture phase shifters), which is compared with that of a conventional 8x8 OPA with 64 per-element phase shifters. Similar to Eq. (4.2) and using Eq. (4.3), the array factor in this case can be written as [96]

$$AF = \sum_{l=1}^{N-1}\sum_{k=1}^{N-1}\sqrt{\left(a_m^2 + b_n^2 + 2a_m b_n \cos(\phi_m - \theta_n)\right)}e^{j(l-1)\sin(\theta)\left[\frac{2\pi n}{\lambda}d\cos\phi + \Delta\phi_x\right]}e^{j(k-1)\sin(\theta)\left[\frac{2\pi n}{\lambda}d\sin\phi + \Delta\phi_y\right]}. \quad (4.11)$$

where $\theta, \phi, \Delta\phi_x$, and $\Delta\phi_y$ are the polar (elevation) angle, the azimuth angle, relative phase difference in rows, and the relative phase difference in columns, respectively. Figure 4.4(a) compares the far-field interference pattern of the proposed scheme and the conventional per-element architecture for the case of diagonal beam-steering. The two OPAs have identical element structure with the same element spacing of 11 μm. The diagonal beam-steering is performed by setting the same relative phase of 0°, 30°, 60°, 120°, and 180° between the adjacent elements in both rows and columns. The normalized main lobe power for different steering angles for these two 8x8 OPAs is compared in Fig. 4.4(b). As predicted by Eq. (4.6), the intensity of the main lobe for the proposed OPA is generally lower than that of the conventional OPA. Note that in Fig. 4.4(a), for a relative phase of 180° between the adjacent elements in the proposed OPA, the intensity of every other element is zero (caused by the cosine term in Eq. (4.6)), effectively doubling the OPA element spacing, which results in a factor of 2 smaller lobe-spacing.

The side-lobe suppression ratio was calculated using the simulated far-field pattern in Fig. 4.4(a). In the conventional OPA with per-element phase control, the side-lobe suppression ratio of about 13 dB is calculated, which is reduced to about 9 dB for the proposed OPA with off-aperture phase adjustment due to the phase dependent amplitude effect described by Eq. (4.6). Note that the proposed architecture here can be used to form and steering a single beam and unlike 2D OPAs with per-element phase shifters, is not capable of simultaneous multi-beam forming. This is due to the fact that setting the phase of individual elements is not possible using this architecture and only the relative phases with linear relationship can be set.

4.1.2 System architecture

In order to demonstrate the idea of reducing the number of phase shifters, an 8x8 OPA is designed and implemented. Figures 4.5(a) and 4.5(b) show the structure of the implemented OPA transmitter.

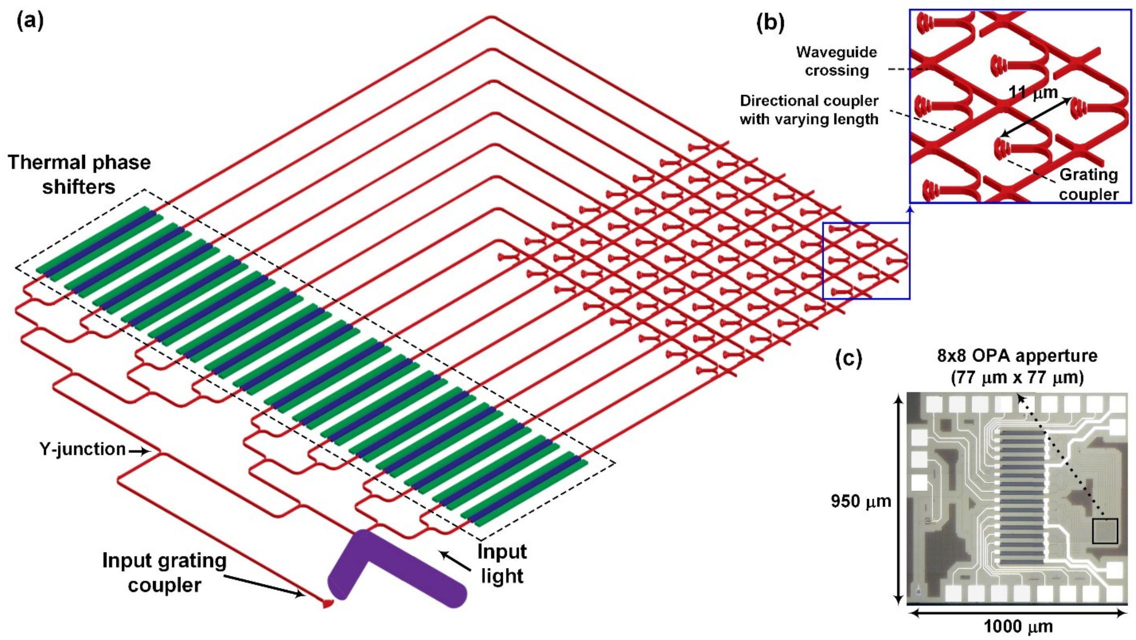

Figure 4.5 – (a) The structure of the implemented 8x8 OPA with 16 phase shifters placed outside of the array aperture. (b) The structures of the grating couplers (as OPA elements) and directional couplers with varying lengths. (c) The microphotograph of the implemented 8x8 OPA chip fabricated in the IME 180 nm SOI process.

The input light is coupled into the chip using an on-chip grating coupler and is guided to a network of Y-junction splitters. The splitter network uniformly splits the coupled light into 16 branches. The phase of optical wave in the nanophotonic waveguide in each branch is adjusted through a thermal phase shifter. After phase adjustment, 8 nanophotonic waveguides serving as rows and 8 nanophotonic waveguides serving as columns are used to guide the optical waves to an array of 8x8 grating couplers serving as the OPA elements. Each grating coupler is placed near the crossing point of a row and a column waveguide and is fed by two directional couplers followed by a Y-junction combiner used to combine a fraction of the light from the corresponding row and column waveguides. The directional couplers have varying lengths to ensure that all grating couplers receive the same optical power. The spacing between the grating couplers within the array aperture is 11 μm and they are placed symmetrically with respect to the row and column waveguides as shown in Fig 4.5(b). The photonic components including the grating coupler, the directional couplers, and the waveguide crossings are carefully designed to make the element spacing as small as possible. The microphotograph of the photonic chip is shown in Fig 4.5(c). The chip has an area of 1000 μm x 950 μm, while the emitter aperture area is 77 μm x 77 μm. The chip is fabricated in the IME 180 nm silicon-on-insulator (SOI) photonic process.

4.1.3 Photonic devices

There are various photonic devices that should be specifically designed in IME 180 nm SOI process to achieve a compact OPA. These components are presented in this section. Figures 4.6 shows the structure of the 200 μm long thermal phase shifter. The phase shifter consists of a TiN metal heater on top of a silicon waveguide and two deep trenches on the sides. Since the phase shifters are thermal, thermal cross-talk can act as noise as biasing one phase shifters can affect others. Therefore, the deep trenches help with more thermal isolation between the phase shifters to enhance the thermal efficiency and reduce thermal cross-talk. The phase shifter has a measured resistance of 350 Ω and I_π of 4.5 mA. Hence, the phase shifters can change the optical phase by more than 2π radians (by injecting 9 mA). In fact, the breakdown current of the thermal phase shifters has been measured to be about 42 mA (corresponding to about 9π radians optical phase shift).

Therefore, any phase mismatch between the waveguides routing the light to the rows (or columns) can be corrected in the calibration phase which will be explained in next section.

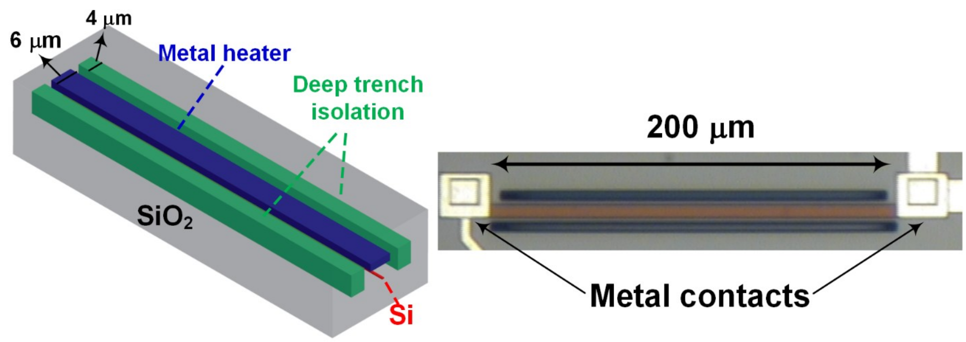

Figure 4.6 – The structure and microphotograph of the thermal phase shifter.

Figure 4.7(b) shows the structure of a grating coupler (serving as the OPA element) as well as the simulated far-field beam pattern. The design of the grating coupler serving as the OPA element follows the one presented in [97], however, the device dimensions and the number of gratings are modified to optimize the coupling efficiency for a compact footprint. The simulated efficiency of the grating coupler is about 30% at 1500 nm.

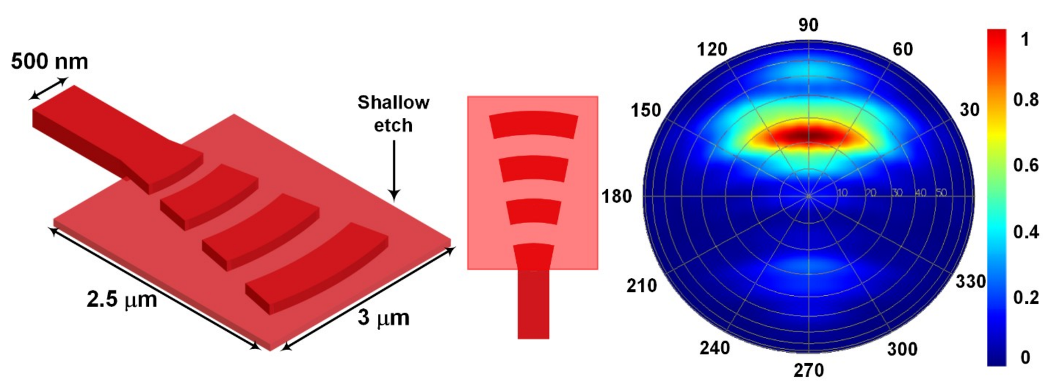

Figure 4.7 – The structure and simulated far-field beam pattern of the designed grating coupler.

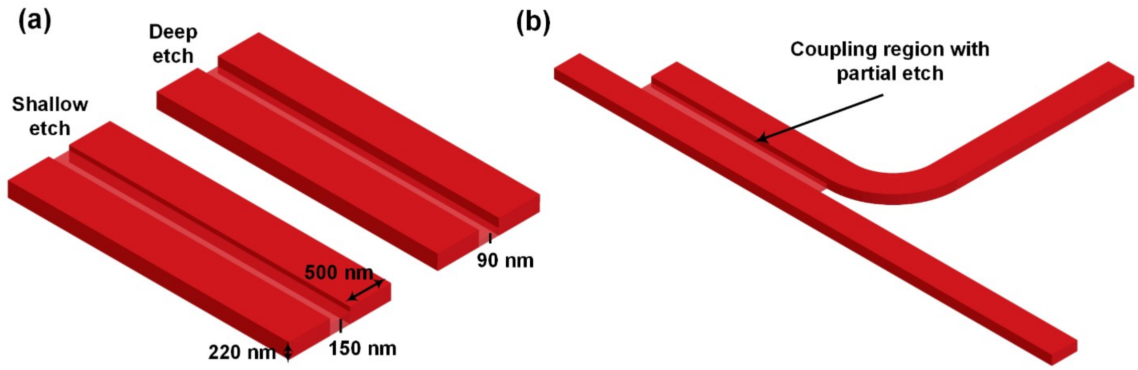

(c)

Coupler	1	2	3	4	5	6	7
Etch	D	D	D	D	D	D	S
Length	1.1μm	1.3μm	1.4μm	1.7μm	2.4μm	3.2μm	2.2μm
Ratio	81/5	80/7	79/8	77/12	75/14	64/24	46/43

D: Deep
S: Shallow

Figure 4.8 – (a) Different levels of Si etch. (b) The structure of the directional coupler with partially etched coupling region. (c) Finite-Difference Time-Domain (FDTD) simulation results for the directional couplers with varying length and different silicon etch levels within the coupling region.

The IME 180 nm SOI process offers three silicon etch levels as shown in Fig. 4.8(a) that are used in the design of the compact directional couplers, grating couplers, and the compact waveguide crossings. Figure 4.8(b) shows the structure of the directional couplers with varying lengths are used in order to equally distribute the optical power in each row and column. To make the element spacing as small as possible, the coupling lengths should be minimized, which is achieved by partially etching the gap in the coupling region to increase the coupling coefficient for a given length. Considering the transmission and the coupling coefficients of the directional couplers, as well as the loss of the waveguide crossings, the required coupling lengths and the etch depth for the 7 directional couplers in each row/column are simulated, which are shown in Fig. 4.8(c).

Note that the 500 nm wide 220 nm thick single-mode nanophotonic waveguides have a measured loss of under 2 dB/cm.

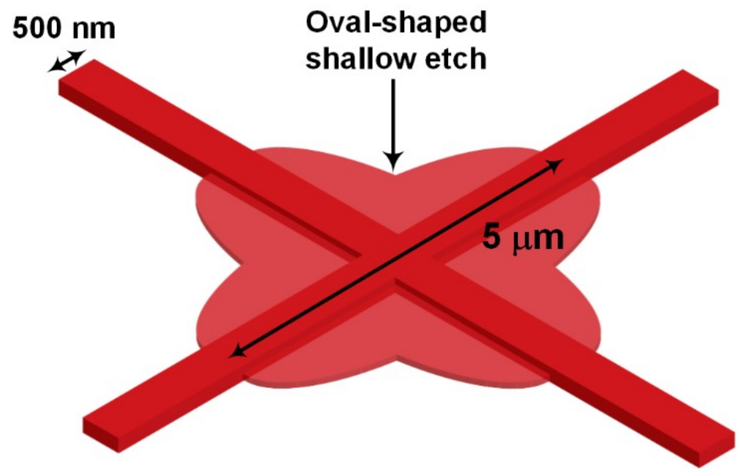

Figure 4.9 – The structure of the designed compact waveguide crossing.

To further reduce the element spacing, a compact waveguide crossing structure is designed. The crossing uses oval-shaped partial Si etch to achieve small size and low loss simultaneously. It has a simulated insertion loss of under 0.3 dB with an isolation of more than 30 dB which are decent results given the total length of 5 μm.

Figure 4.10 summarizes the structure of a single element along with the corresponding row and column waveguides and the feed network. Note that in order to achieve symmetric routing, the grating couplers are placed at a 45 degree angle with respect to the column waveguides as shown in Fig 4.5. The Y-junction that is used for combining the row and column signals is similar to the design in [98]. It has a measured excess loss of about 0.5 dB.

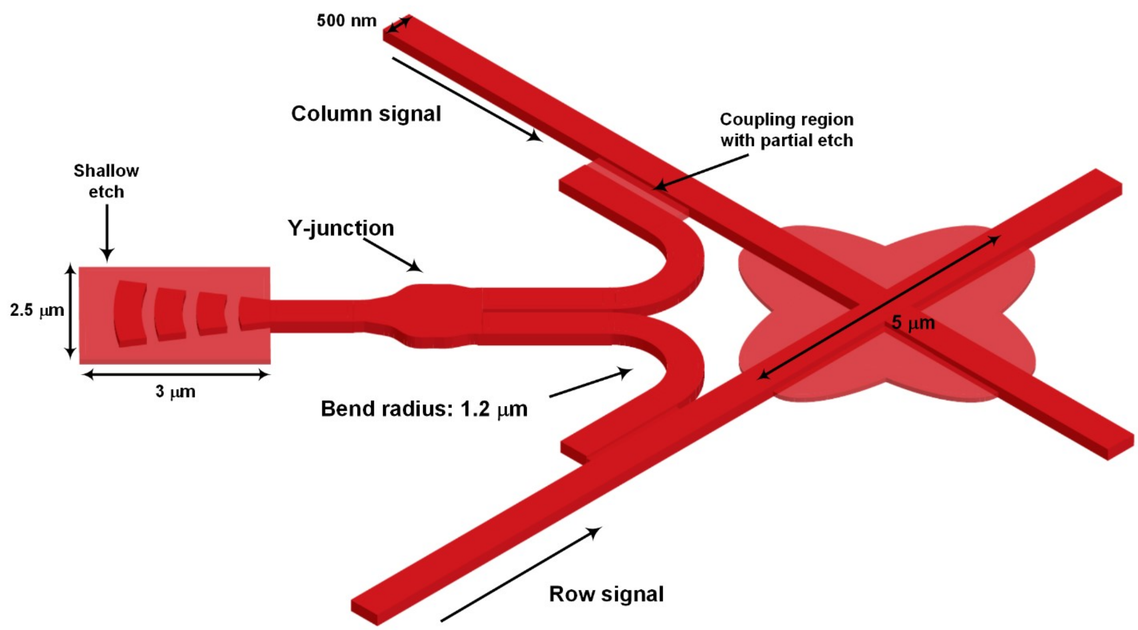

Figure 4.10 – The structures of the nanophotonic waveguides, the waveguide crossing, directional couplers with varying length, the Y-junction, and the grating coupler serving as the OPA element.

4.1.4 The effect of layout mismatches

Due to fabrication process variations, the phase of optical signals in different waveguides guiding the light to the rows and columns of the aperture are unknown. However, we are using thermal phase shifters, which can change the optical phase by more than 2π radians (by injecting 9 mA). Therefore, any phase mismatch between the waveguides routing the light to the rows (or columns) can be corrected in the calibration phase. The calibration process is explained in the next section on the measurement results.

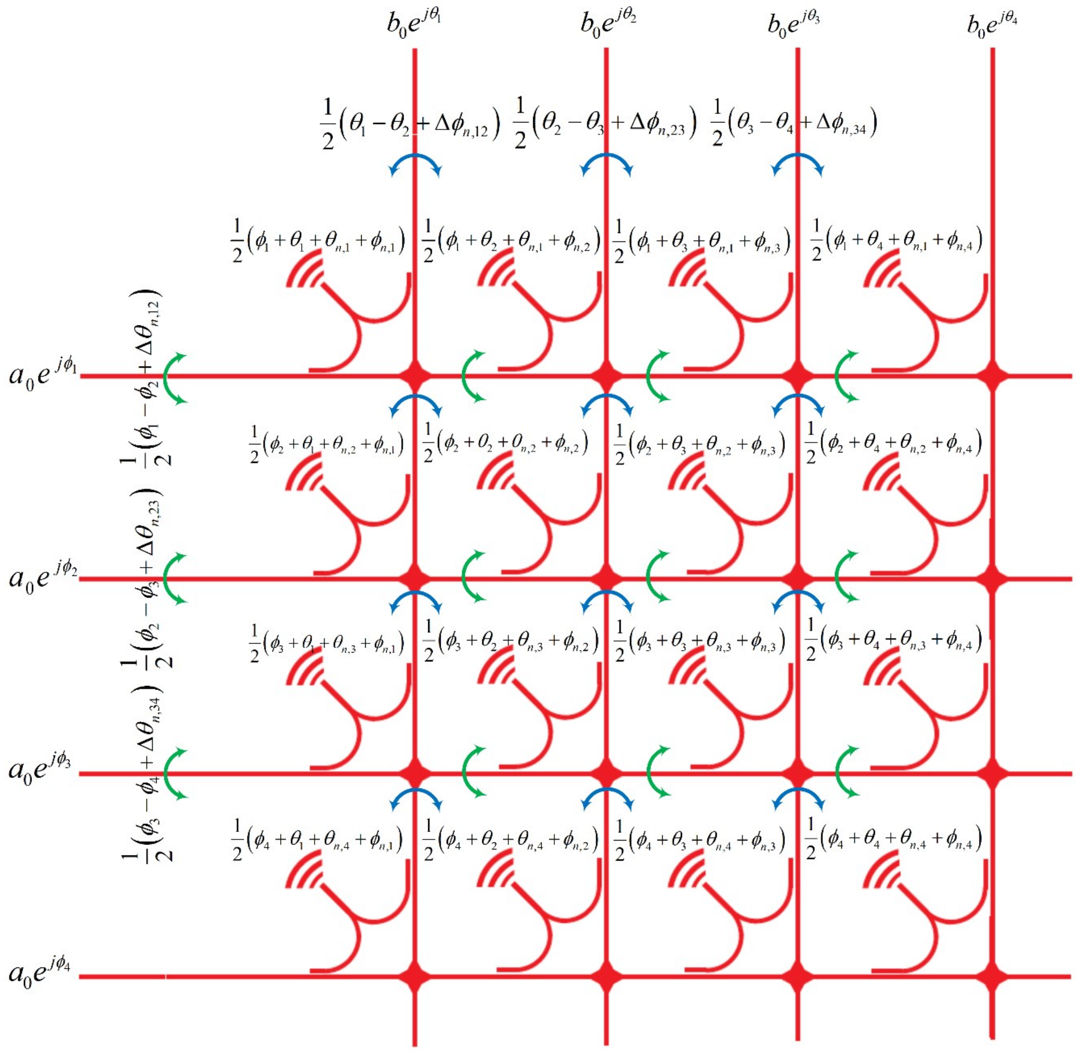

$$
\begin{cases}
\Delta\phi_{n,ij} = \phi_{n,i} - \phi_{n,j} \\
\Delta\theta_{n,ij} = \theta_{n,i} - \theta_{n,j}
\end{cases}
$$

Figure 4.11 – The effect of phase mismatch.

In addition, note that for advanced foundry processes, while the level of mismatch between the designed and fabricated devices may be large, there is a rather high degree of matching among the closely placed on-chip identical structures. For example, in [83], using a 65nm process for implementation of a large scale optical phased array of 64x64 emitters, relatively good beam-forming results (with no active adjustment) have been achieved. Similarly, our proposed architecture uses a similar approach to distribute the light between the emitting elements of the rows and columns within the aperture. Note that the aperture is quite small and the identical structures are placed closely and hence the mismatch between the devices within the aperture should be very small.

Nevertheless, to elaborate on this, Fig. 4.11 shows the effect of phase mismatch where for simplicity an array of 4x4 emitters (along with the corresponding row and column waveguides) is shown. Here, we assume that the unknown phase between the adjacent elements in the i^{th} row has two components: $\theta_{n,i}$ and $\phi n,i$, where $\theta_{n,i}$ is the same for all elements on the i^{th} row, since identical directional couplers are used to couple the light into the emitters from all columns, while $\phi_{n,i}$ may be different for each element on the i^{th} row since directional couplers with varying lengths are used to couple the light from the i_{th} row waveguide to the emitters of the i^{th} row. Similarly, for the j^{th} column, $\phi_{n,j}$ is the same for all elements while $\theta_{n,i}$ may be different for different emitters on the j^{th} column. Under this assumption, the relative phase between adjacent elements within the aperture is calculated, which is shown in Fig. 4.11. For a desired relative phase of $\Delta\theta$ and $\Delta\phi$ in the X and Y directions, we have

$$\Delta\theta = \frac{1}{2}\left(\theta_1 - \theta_2 + \Delta\phi_{n,12}\right) = \frac{1}{2}\left(\theta_2 - \theta_3 + \Delta\phi_{n,23}\right) = \frac{1}{2}\left(\theta_3 - \theta_4 + \Delta\phi_{n,34}\right). \tag{4.12}$$

$$\Delta\phi = \frac{1}{2}\left(\phi_1 - \phi_2 + \Delta\theta_{n,12}\right) = \frac{1}{2}\left(\phi_2 - \phi_3 + \Delta\theta_{n,23}\right) = \frac{1}{2}\left(\phi_3 - \phi_4 + \Delta\theta_{n,34}\right). \tag{4.13}$$

Therefore, the phase of the rows and columns should be set such that

$$\begin{cases} \theta_1 = const. \\ \theta_2 = \theta_1 - 2\Delta\theta + \Delta\phi_{n,12}. \\ \theta_3 = \theta_2 - 2\Delta\theta + \Delta\phi_{n,23}. \\ \theta_4 = \theta_3 - 2\Delta\theta + \Delta\phi_{n,34}. \end{cases} \tag{4.14}$$

$$\begin{cases} \phi_1 = const. \\ \phi_2 = \phi_1 - 2\Delta\phi + \Delta\theta_{n,12}. \\ \phi_3 = \phi_2 - 2\Delta\phi + \Delta\theta_{n,23}. \\ \phi_4 = \phi_3 - 2\Delta\phi + \Delta\theta_{n,34}. \end{cases} \tag{4.15}$$

Note that $\Delta\theta_{n,ij}$ and $\Delta\phi_{n,ij}$ are unknown but constant as there is a negligible thermal gradient across the closely packed on-chip devices. These equations show that for a desired $\Delta\theta$ and $\Delta\phi$, θ_i and ϕ_i can be found using a gradient descent optimization process as in [85], where the far-field interference pattern is compared with the simulation result for the case that both row and column signals have zero phase offset. Then, by adjusting the currents of the thermal phase shifters around the corresponding calibration point, the 2-D beam-forming is performed.

4.1.5 Characterization and 2-D beam steering results

Characterization of the OPA chip includes monitoring the grating lobes of the far-field interference pattern, 2-D beam steering, total system path loss, and the power radiated in the main lobe. The measurement setup for characterizing the proposed OPA is shown in Fig. 4.12(a), where a laser emitting 1 mW at 1502 nm is coupled into the chip input grating coupler using a single-mode optical fiber after passing through a polarization controller. Two digitally controlled 8-channel thermal phase modulator drivers were used to control the row and column phase shifters, each with 8-bit output voltage resolution. A FJW FIND-R-Scope 85700A infrared camera with adjustable optics were used to monitor the far-field interference pattern of the OPA.

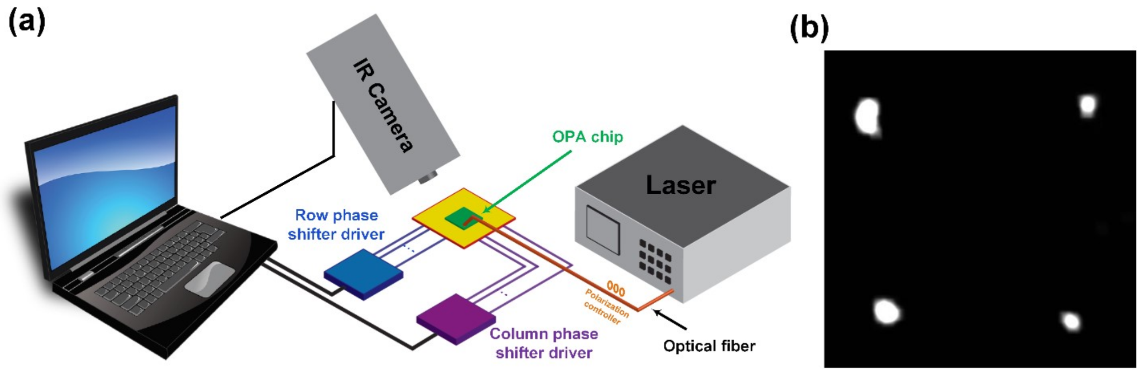

Figure 4.12 – (a) Measurement setup used to characterize the OPA chip. (b) Measured far-field interference pattern showing four grating lobes.

In order to demonstrate 2-D beam-steering, the thermal phase shifters are used to control the phase of the optical signals in each row and column. To account for the different waveguide routing lengths and process variations, the OPA was first calibrated (using the procedure in [85]), where the far-field interference pattern is compared with the simulation result for the case that both row and column signals have zero phase offset. Then, by adjusting the currents of the thermal phase shifters around the corresponding calibration point, the 2-D beam-forming was performed. Figure 4.12(b) shows four grating lobes of the far-field interference pattern of the OPA.

Figure 4.13 shows the 2-D beam-steering results in which only one grating lobe is shown. By controlling the phase of the thermal phase modulators in the rows and columns, beam-steering range of about 7° is demonstrated, which is in agreement with the simulation results in Fig. 4.4(a).

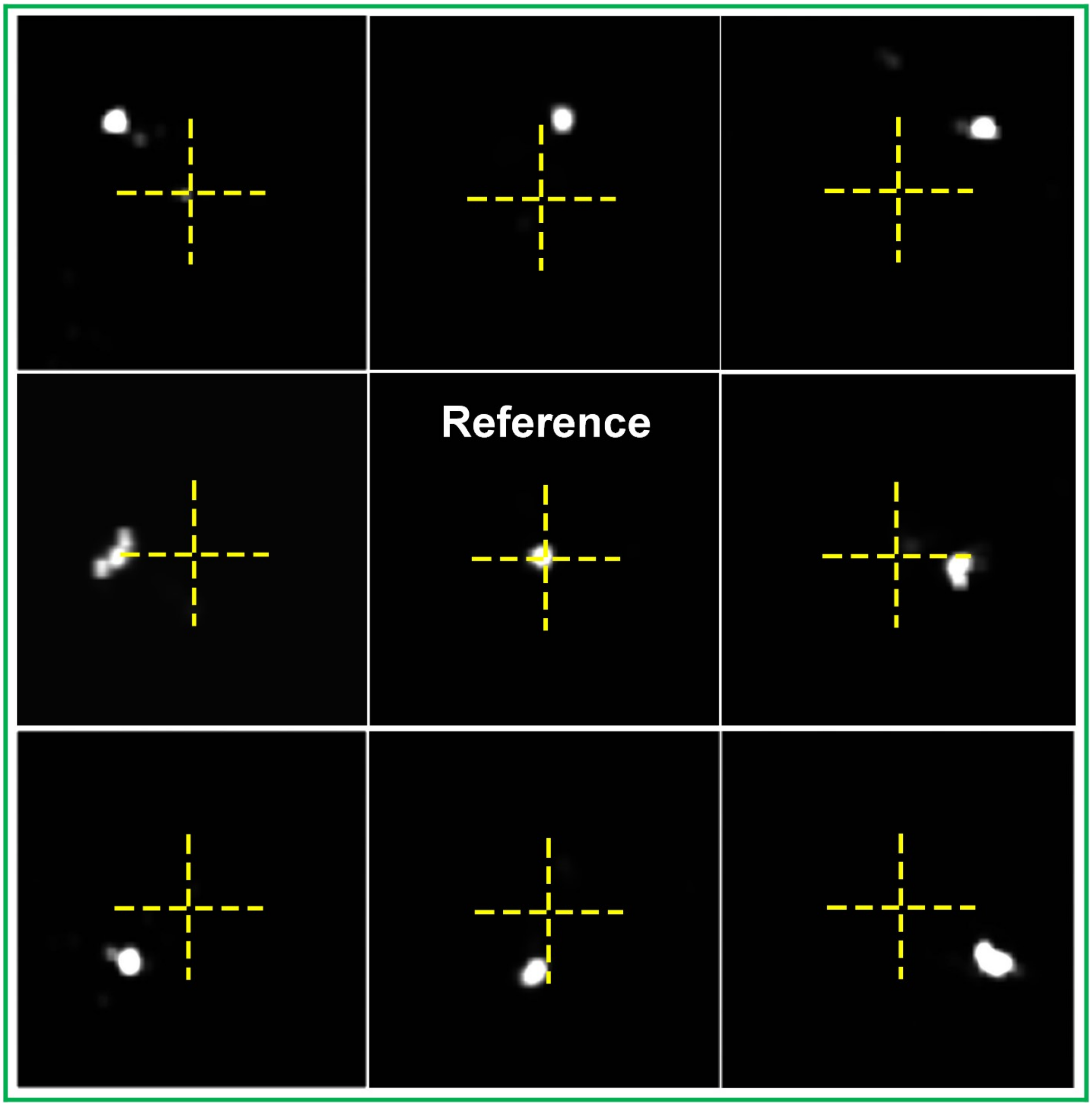

Figure 4.13 – Demonstration of the 2-D far-field beam-steering. The reference spot is at the center and the pictures around it show the movement of the beam.

Another experiment that was carried out was measuring two consecutive resolvable spots. The result is shown in Fig. 4.14(a) shows two consecutive resolvable spots as the main lobe is steered diagonally. The corresponding beam profiles are shown in the bottom section of Fig. 4.14(b).

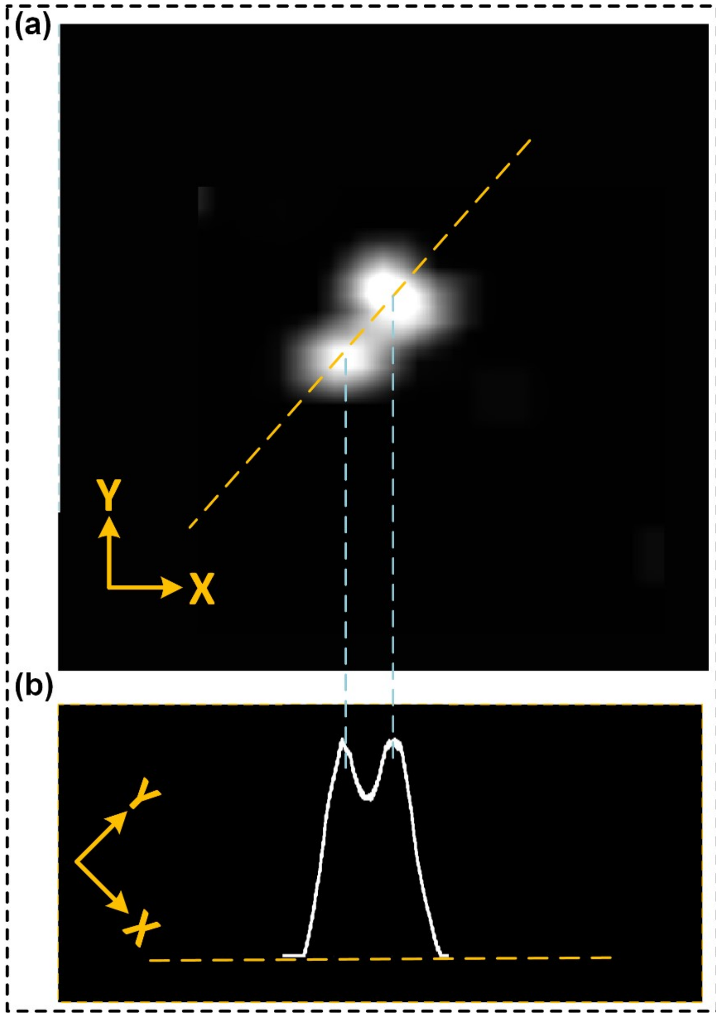

Figure 4.14 – (a) Two consecutive resolvable spots while diagonal beam-steering is performed. (b) The beam profiles.

Assuming that a 0 dBm optical power is coupled into the input grating coupler, the estimated output power for each emitting grating coupler is about -38 dBm. Out of this 38 dB power drop, 21 dB is due to the power distribution among the emitters (64 emitters and each emitter is driven by two inputs; one from the corresponding row and one from the corresponding column), 10 dB is due to the loss of the input and output grating couplers (4.5 dB measured loss of the input grating coupler and 5.5 dB simulated loss of the emitting grating coupler), 2 dB excess loss of the Y-junction splitter network (0.5 dB measured excess loss per Y-junction), 3.5 dB loss of the Y-junction combiner before each emitter (since its two input are not necessarily in-phase), and 1.5 dB simulated loss of routing, bends, and waveguide crossings.

Table 4.1 – 8x8 OPA (IME) performance summary

Number of elements	**64 (8x8)**
Element spacing	**11 μm**
Element dimensions	**2.5 μm x 3 μm**
Number of phase shifters	**16**
Beam steering range	**7°**
Process	**IME 180 nm SOI**

Finally, a measurement was performed to find the power of the main lobe. In this measurement, first, the chip is replaced with a collimator with narrow output beam-width, where a known low-power collimated laser beam is used to illuminate the IR camera with the same angle of incidence and from the same distance. Under the condition that the camera pixels are not saturated, a relationship between the camera output image and the beam power is established (i.e. given the pixel luminance range of 0 to 255, the total power can be estimated by integrating the image profile). Then, the collimator is replaced with the chip and image of a single spot is acquired and used to estimate the power in the main lobe. The result shows that when the optical power coupled into the chip is set to -2 dBm (close to the number that was used to demonstrate beam-steering), the power in the main lobe is about -45 dBm. Note that no lens is used in both measurements.

4.2 OPA with compact elements

In Section 4.2, it was demonstrated that for linear 2-D beam steering, the number of phase shifters can be cut by a factor of N/2 for an N×N OPA. As shown before, this approach significantly reduces the electrical and optical routing complexity and power consumption. The lower routing complexity is especially important in designing OPAs with very compact element spacing as this and also the size of the elements are the main limit of the side-lobe suppression. The proposed architecture significantly relaxes the first limitation. Therefore, to further reduce the element spacing, smaller elements are required. However, as shown in Fig. 4.5(b) and Fig. 4.9, most of the space between the elements is consumed by the photonic devices for combining the row and column signals in route to the grating coupler. The challenge is that further reduction of the element spacing requires reducing the size of theses photonic routing devices. This is very challenging since the optical loss significantly increases upon further reduction in size. For instance, the directional couplers need about 5 μm length, half of the element spacing. Therefore, another approach is required to further reduce the element spacing and/or other mechanisms for coupling and power combining.

Since combining row and column signals and the necessary photonic routing is the main limiting factor, an alternative is to perform the power combination vertically. Using photonic fabrication processes that offer two layers of photonic routing. Therefore, the architecture previously shown in Fig. 4.5 can be modified to the one shown in Fig. 4.15. This figure shows a conceptual schematic of this idea where the input light is coupled to a grating coupler and is split in to two signals: one routed to the rows through a layer transition (photonic via) and the other routed to the columns. The rows are implemented using the bottom routing layer (orange) and the columns are realized in the top layer (purple). These layers are at a small vertical distance from each other (sub-wavelength), the signals of the rows and columns are combined vertically.

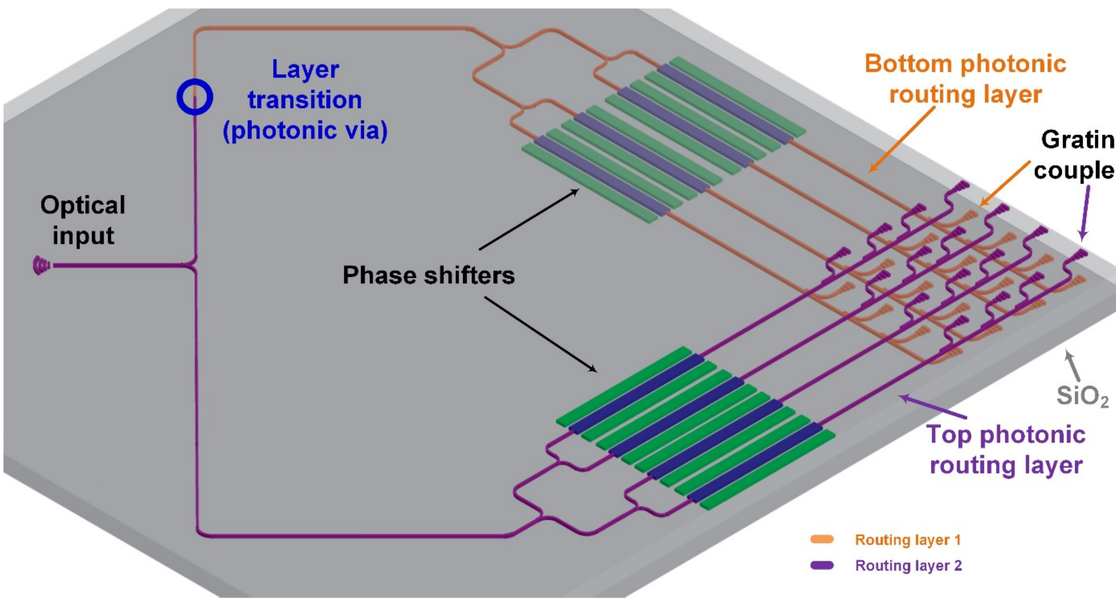

Figure 4.15 – Conceptual schematic of a 4x4 OPA that uses two photonic routing layers to realize vertical power combining reducing the element spacing within the aperture.

Note that by eliminating the photonic devices for signal combining, the elements can be placed closer to each other. In this case, the size of the individual elements can be the limiting factor in achieving a very compact OPA aperture. This issue can be addressed by placing series grating structures (as the emitting elements) on the same waveguide as shown in Fig. 4.16. The grating structures can be made by fully or partially etching the waveguide [99]. By changing the number of gratings and/or their width, the amount of optical power coupled in/out can be adjusted. Therefore, multiple OPA elements can be implemented using series grating structures that are very closely packed. Especially since this structure eliminates the need for directional couplers for light distribution, compact OPA apertures can be realized. By superimposing the gratings made in each photonic layer, their outputs can be combined vertically to implement a 2-D OPA. The details of the design of the waveguide gratings as well as the 2-D OPA is presented in the following sections.

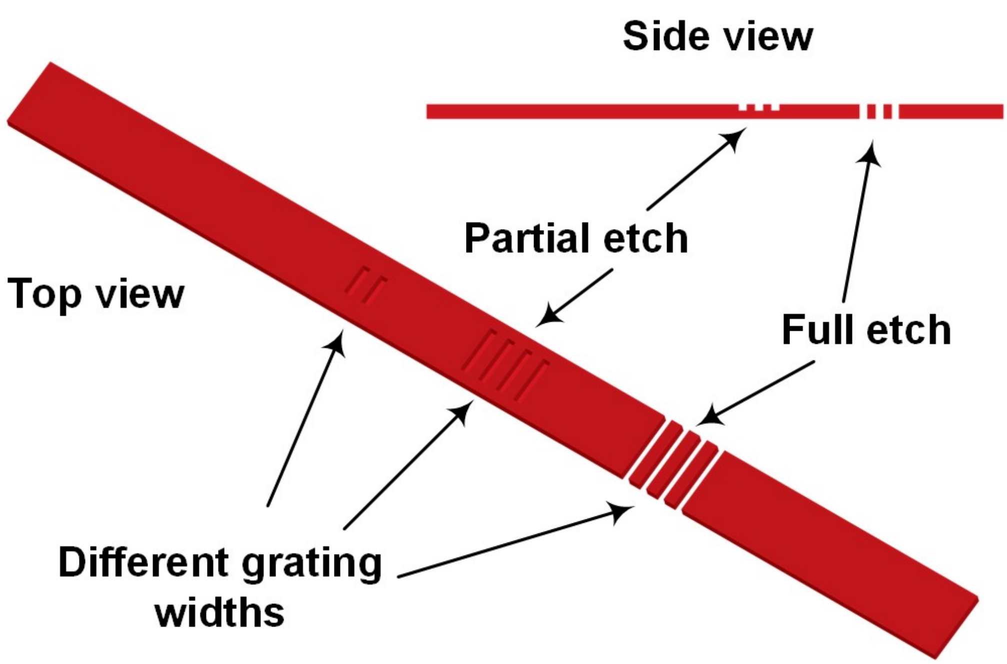

Figure 4.16 – Waveguide gratings as the elements of an OPA.

4.2.1 System architecture

As previously mentioned, the proposed approach to further reduce the element spacing benefits from the availability of two layers of photonic devices and implementation of series grating structures on the same waveguide as the emitting elements of the OPA. Figure 4.17(a) shows the schematic of the designed OPA in TowerJazz 180 nm silicon photonic process. The process features silicon (Si) and silicon nitride (SiN) as the two photonic device layer. Since silicon has a higher index of refraction compared to nitride ($n_{Si} \approx 3.5, n_{Nitride} \approx 2$), it offers better light confinement allowing for more compact photonic components such as straight waveguides and waveguide bends to be implemented. In fact, in the TowerJazz process the minimum Si waveguide width, minimum SiN waveguide width, minimum Si waveguide bend radius, and minimum SiN waveguide bend radius are 450 nm, 800 nm, 2 μm, and 20 μm, respectively. Thus, it is more area efficient to do the photonic routings using the Si layer as much as possible.

The input light is coupled to the chip by bringing an optical fiber close to the input grating coupler implemented in Si layer. The light is split into 16 branches using 4 layers of Y-junctions in the same layer resulting in 8 row signals and 8 column signals. Each signal passes through a thermal phase shifter to properly set the optical phase. Since the process does not offer any deep trench isolation, the thermal isolation between phase shifters is enhanced by alternating the location of them in consecutive optical paths. After phase adjustment, the signals are routed towards two sets of waveguides with emitting elements; one in Si layer (columns, shown in red) and one in SiN (rows, shown in purple).

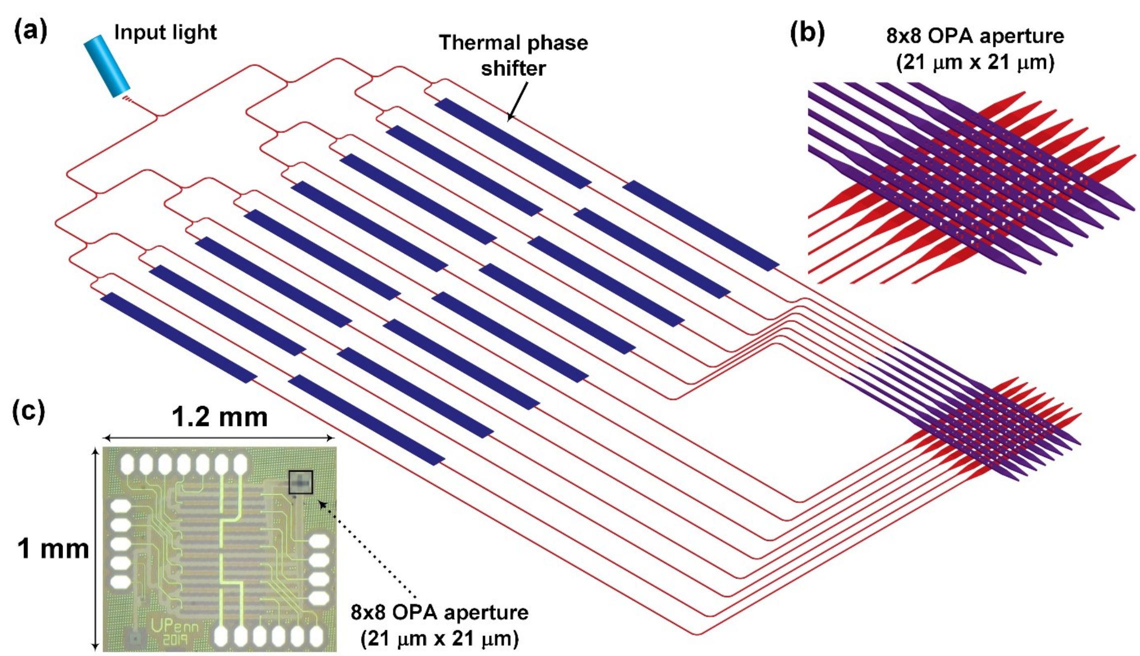

Figure 4.17 – (a) The schematic of the implemented OPA chip in TowerJazz process that used two levels of photonic routing. (b) The zoomed-in view of the OPA aperture. (c) The chip microphotograph.

The optical signals of the rows are transferred to SiN layer using photonic layer transitions (photonic vias) implemented using long waveguide tapers that operate based on vertical evanescent coupling between two tapers, one in Si and one in SiN layer. This results in full transfer of light from one layer to the other.

The phase modulated optical waves are guided to the array aperture which consists of two sets of 8x8 arrays of grating structures, one in Si layer and the other in SiN as shown in Fig. 4.17(b). Note that the gratings are placed at 45° angle with respect to the axis of the waveguides to align the radiation direction of the two layers that are placed on top of each other. The details of the grating design is resented in the next section. The OPA has an element spacing of 3 μm corresponding to an aperture size of 21 μm. The microphotograph of the chip with an area of 1000 μm x 1200 μm is shown in Fig 4.17(c).

Figure 4.18 shows the simulated beam steering result for the proposed OPA where 2-D steering can be seen. The simulation is done using Lumerical FDTD tool. The graphs show the far-field interference pattern.

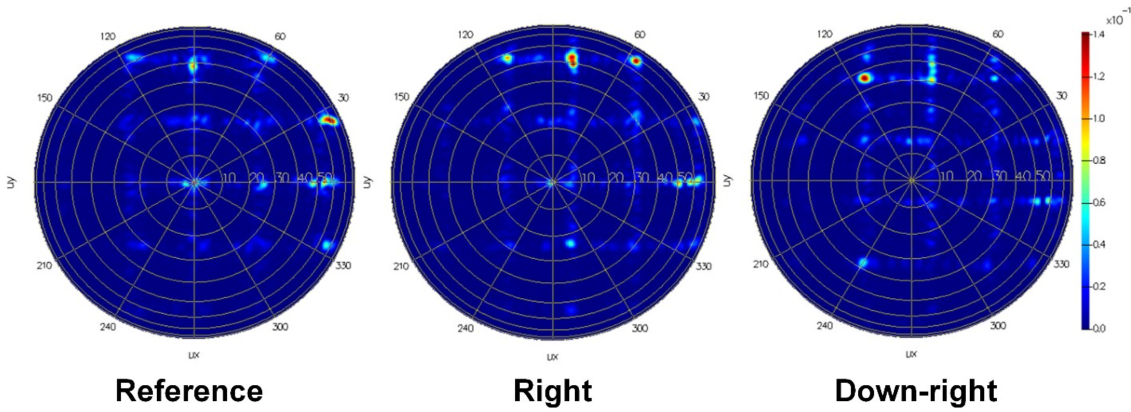

Figure 4.18 – Simulated beam steering results of the proposed two layer OPA.

4.2.2 Photonic devices

Similar to the previous chip, there are photonic devices specifically designed for this more compact OPA implemented on the TowerJazz 180 nm SOI process. Figure 4.19(a) shows the structure of the thermal phase modulator. It is 200 μm long and consists of a TiN resistor on top of the Si waveguide. Since there is no deep trench available in the process, the thermal modulators are placed far from each other to enhance thermal isolation. The phase shifter has a measured resistance of 230 Ω and I_π of 6 mA which is larger than the previous version due to lack of deep trench isolation. Figure 4.19(b) shows the microphotograph of the thermal phase shifter.

As mentioned in the previous section, the design of the compact OPA is based on the two layers of photonic devices Figure 4.19(c) shows the photonic layer transition (photonic via) used to transfer light from one layer to the other. It consists of two waveguide tapers; on in Si and the other on in SiN. Based on the 80 nm vertical spacing of these layers, it takes about 50 μm of coupling length for the light to fully transit between layers and the simulated loss of the via is less than 0.9 dB.

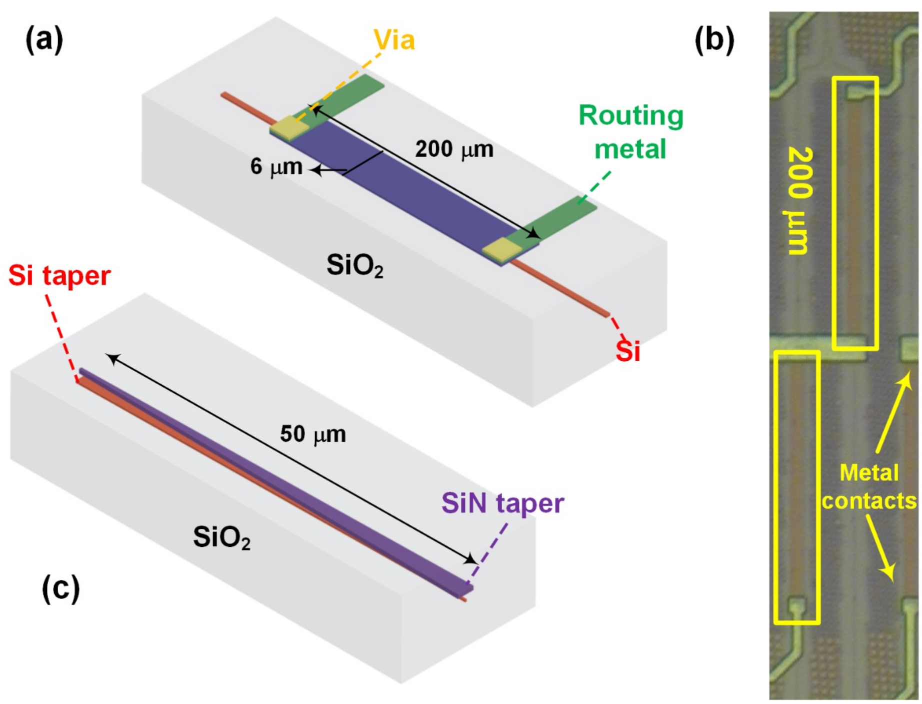

Figure 4.19 – (a) The structure of the thermal phase shifter and (b) its microphotograph. (c) The structure of the photonic via.

The design of the OPA aperture is done in two layers. The rows are implemented in SiN and the columns in Si. However, the design strategies for the grating structures in both layers are similar. There are two main considerations in designing the grating structures:

1- Aligning the radiation angles of the Si and SiN gratings around the wavelength of interest.

2- Uniform distribution of light among the gratings in a row/column.

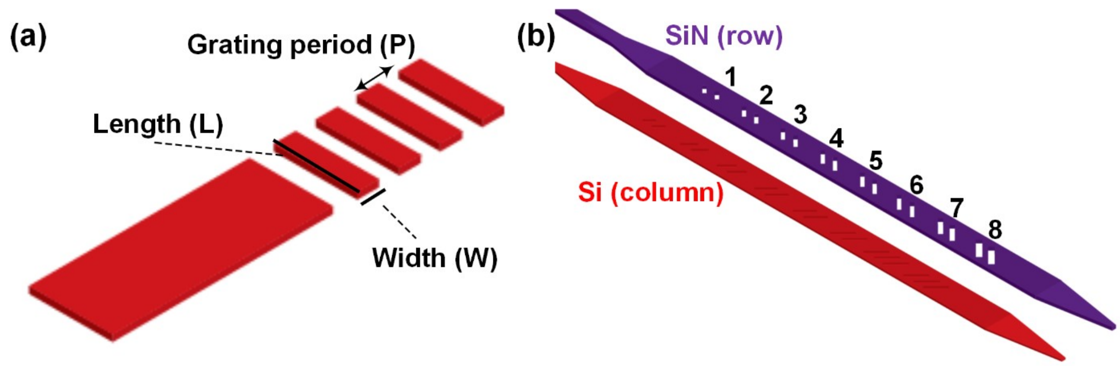

(c)

GC	1	2	3	4	5	6	7	8
Si: Length/width (μm)	0.8/0.2	1/0.2	0.8/0.2	1.2/0.2	1.1/0.25	1.5/0.25	1.5/0.2*	1.7/0.25*
SiN: Length/width (μm)	0.7/0.2	1/0.2	1.2/0.2	1.3/0.2	1.5/0.2	1.8/0.2	1.8/0.35	2/0.55

* 3 teeth

Figure 4.20 – (a) The structure and dimensions of a waveguide grating. (b) The waveguide gratings designed for the 8x8 OPA with 3 mm element spacing and (c) the corresponding grating lengths and widths.

The main design parameters of a grating structure are the grating length, width, and period as shown in Fig 4.20(a). To achieve the first goal, we need to consider the relationship between the angle of radiation of a grating structure and other design parameters (*i.e.* wavelength, index of refraction, and grating period. Equation (4.16) shows this relationship [100]

$$n_w - n_0 \sin(\theta) = \frac{\lambda}{\Lambda}. \tag{4.16}$$

where $n_w, n_0, \theta, \lambda,$ and Λ are the index of refraction of the waveguide, the index of refraction of the medium (in this case SiO_2), the radiation angle, the wavelength of the light, and the period of the grating, respectively. For the two layers, the wavelength (λ) and the index of refraction of the SiO_2 (n_0) is the same. Therefore, for each material given the associated index of refraction (n_w), the radiation angle depends on the grating period (Λ). Thus, based on the Lumerical FDTD simulation results, the grating periods of 1.2 μm and 0.7 μm are chosen for SiN and Si layers, respectively. Note that beam alignment is done for a specific wavelength. This means that unlike the previous implementation, this OPA is considered to be narrow-band.

Figure 4.20(b) shows the row and column waveguide gratings acting as the elements of the phased array. Note that for the SiN gratings full etch and for the Si gratings half-etch is used. The same structure is used for all rows/columns. As mentioned previously, the 45 degree angle is for beam alignment between the vertically stacked Si and SiN layers. The individual dimensions of all elements are shown in Fig. 4.20(c). The grating lengths and widths are designed such that the output optical power of all elements are about the same value. For the same reason, the last two gratings in Si layer use three teeth instead of two to balance the optical power. Passivation etching is used in the aperture area to reduce loss. The simulated optical power variations is about 1.5 dB across the whole aperture with an average optical emission efficiency of 1.5% per grating coupler.

4.2.3 Characterization and 2-D beam steering results (main lobe power, total loss)

Characterization of the second OPA chip is similar to the first one and includes monitoring of the grating lobes of the far-field interference pattern, 2-D beam steering, total system path loss, and the power radiated in the main lobe.

The measurement setup for characterizing the OPA is shown in Fig. 4.21. A laser emitting 0.5 mW at 1470 nm is coupled into the chip input grating coupler using a single-mode optical fiber after passing through a polarization controller. This wavelength is chosen since the two layers emit with similar angles according to Eq. (4.16). Two digitally controlled 8-channel thermal phase modulator drivers were used to control the row and column phase shifters, each with 8-bit output voltage resolution. A FJW FIND-R-Scope 85700A infrared camera with adjustable optics were used to monitor the far-field interference pattern of the OPA.

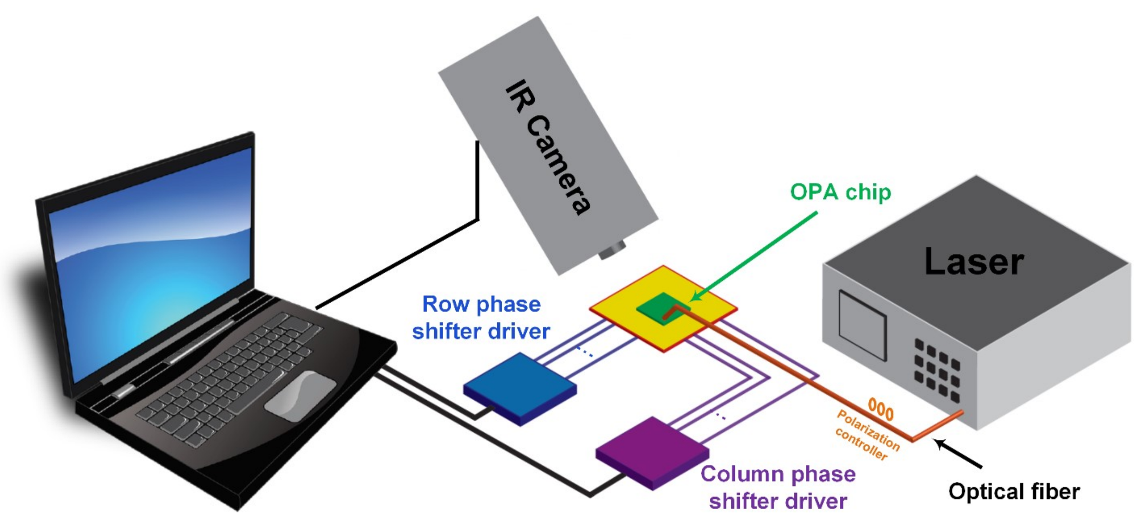

Figure 4.21 – The measurement setup for OPA characterization that includes a tunable laser source, two digitally controlled phase shifter drivers, and an IR camera.

For 2-D beam-steering demonstration, the thermal phase shifters are used to control the phase of the optical signals in each row and column. The first step is to find the proper wavelength that the row and column beams are aligned. This is done by monitoring the far-field interference pattern. The beams are aligned once only one spot is seen while that spot is being moved by adjusting the phase shifter currents. Once again, to account for the different waveguide routing lengths and process variations, the OPA was first calibrated, where the far-field interference pattern is compared with the simulation result for the case that both row and column signals have zero phase offset. Then, by adjusting the currents of the thermal phase shifters around the corresponding calibration point, the 2-D beam-forming was performed.

Figure 4.22 shows the 2-D beam-steering results in which only one grating lobe is shown. By controlling the phase of the thermal phase modulators in the rows and columns, beam-steering range of about 23° is demonstrated. To estimate the power in the main lobe, the digital output of the IR camera is recorded and compared to when the number when another source with a known power illuminates the camera. Using this method, the power in the main lobe is measured to be about -46 dBm.

Table 4.2 summarizes the specifications of the OPA chip.

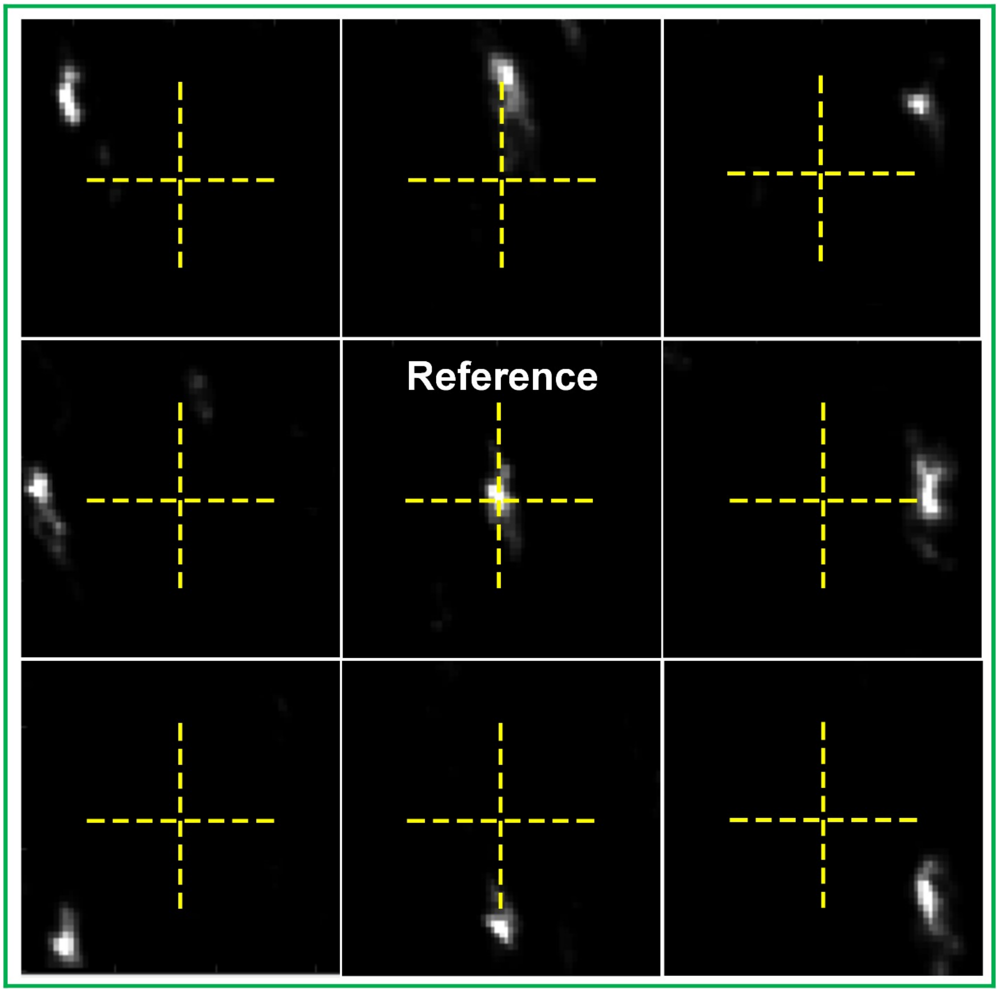

Figure 4.22 – 2-D beam steering results using the OPA with 3 μm element spacing.

Table 4.2 – 8x8 OPA (TowerJazz) performance summary

Number of elements	**64 (8x8)**
Element spacing	**3 μm**
Element dimensions (average)	**1.5 μm x 2 μm**
Number of phase shifters	**16**
Beam steering range	**23°**
Alignment bandwidth	**~ 4 nm**
Process	**TowerJazz 180 nm SiPh**

4.3 Summary and future works

Ultra-compact OPAs, ideally with half-wavelength element spacing, have been studied through different approaches due to their various applications in communications, LiDAR and autonomous vehicles, imaging and projection systems. Such systems enable 2-D beam steering with large steering range as well as large side-lobe suppression ratio. The main challenges in implementing such OPAs are the size of the elements as well as the area required for complex photonic and electrical routings. Increasing the number of elements of the OPA only exacerbates the situation and increases the power consumption of the OPA. Therefore, to move towards half-wavelength element spacing both the routing complexity and the element size should be reduced. To address the former, a novel NxN OPA scheme was proposed that uses only 2N phase shifters instead of the conventional way that needs N^2 phase shifters to perform 2-D beam steering with linear phase relationship between the two directions. This approach significantly reduces the power consumption as well as the electrical and photonic routing complexities and eliminates the metallic-induced optical loss within the aperture by moving the phase shifters outside the aperture. As a proof of concept, an 8x8 OPA with 16 phase shifters was implemented in IME 180 nm SOI process. The 64-element OPA has an aperture size of 77 μm x 77 μm (element spacing of 11 μm) and achieves a steering range of 7°. The element spacing is mainly limited by the photonic devices required for row and column signal combination, despite the effort to minimize their sizes.

To further reduce the element spacing, we benefited from the TowerJazz 180 nm SOI process that offers two layers of photonic devices in Si and SiN where one layer is used for beam steering along the X axis and the other for steering along the Y axis. Waveguide gratings were used in both layers as the emitting the elements of the OPA to realize very compact elements. The optical beams of the two layers that are a fraction of the wavelength far from each other are combined vertically at a certain wavelength range. Similar to the first chip, another 8x8 OPA was implemented has an aperture size of 21 μm x 21 μm (element spacing of 3 μm) and achieves a steering range of 23°. Although the element spacing is still larger than half-wavelength, it is the smallest element spacing in 2D OPAs ever demonstrated to date.

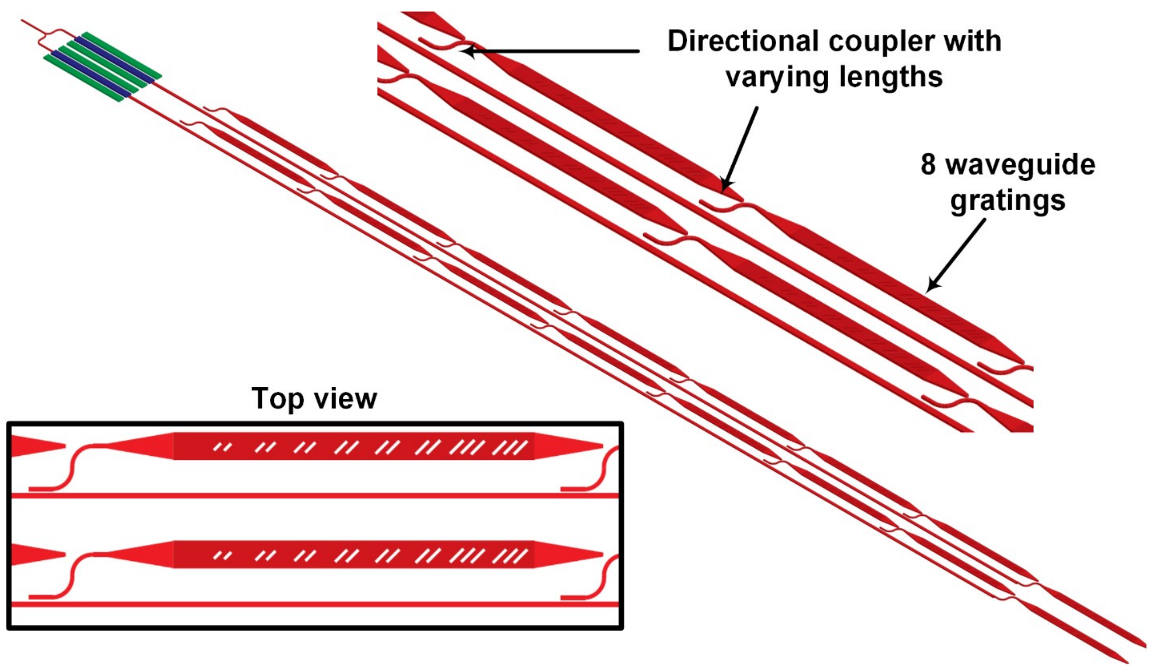

Figure 4.23 – Scaling the number of elements by using waveguide gratings and directional couplers with varying length together.

An immediate future work based on the proposed OPAs is to scale the OPA to larger number of elements. An important motivation is the phase shifter reduction factor which is N/2. For the implemented chips this factor is 4. However, as the number of elements increases, this factor will be more significant. For instance, for a 128x128 OPA, the proposed approach requires 64 times less number of phase shifters that results in a much smaller power consumption as well as significantly more relaxed photonic routing. Therefore, it is desired to increase the number of elements.

The challenge in increasing the number of elements in both chips, is the uniform light distribution. In the first chip, more number of elements requires directional couplers with very uneven ratios and close values. This makes the design process variation dependent although OPAs with 4096 elements have been demonstrated using the same approach [83]. In the second chip, the light distribution is done by designing the aspect ratio of the gratings and because of the finite fabrication tolerance, it is challenging to fabricate gratings with very small aspect ratio differences.

One potential approach could be through combining the two approaches for each of the two layers. As shown in Fig. 4.23, 64 element 1-D array of elements can be implemented using eight sets of grating waveguides, each having eight gratings similar to the ones used in the second chip. Seven directional couplers with varying lengths are used to distribute the light among the grating sets. This is also similar to the approach in the first chip. A 64x64 element array in Si layer can be made by putting the 1-D arrays next to each other. The same strategy can be used for the second layer to realize an OPA for 2-D beam steering.

CHAPTER 5

Conclusion

5.1 Summary

Electronic-photonic integrated systems are becoming more and more popular mainly due to the fact that they have the advantages of both platforms: sophisticated, low-power, high-speed electronics to implement complex signal processing as well as control, together with miniaturized optical components and systems to benefit from the large bandwidth available at optical frequencies as well as the small propagation loss in optical regime. Therefore, these unique capabilities, make electronic-photonic systems very promising candidates for a variety of applications. In this thesis, I presented three integrated electronic-photonic systems to address optical signal synthesis, optical signal processing, and optical beam steering as some of the most desirable applications.

The first system is a partially integrated OFS with many applications in communications, ranging and sensing. The OFS features an integrated EOPLL and uses an electro-optically generated frequency comb as the reference to the system. In a coarse tuning phase, the custom-fabricated widely tunable laser is frequency tuned across a wide range by adjusting its mirrors and phase section currents. As the TL is being tuned, it passes the teeth of the OFC. Therefore, by using an indexing systems and counting the number of passing teeth, it is possible to determine the location of the TL with respect to the comb. Once the TL reaches the vicinity of the comb tooth closest to the target frequency to be synthesized, the EOPLL is engaged and phase-frequency locks the TL to the comb tooth. Benefiting from the heterodyne architecture of the EOPLL, the TL can be then fine-tuned by adjusting the frequency of the local heterodyning RF oscillator. An aided acquisition system enhances the acquisition range of the EOPLL to cover the tooth spacing of the OFC. In addition to detailed block characterizations, the full systems was used to demonstrate frequency synthesis. The proposed systems is capable of performing optical frequency synthesis over 5 THz with sub-Hz fine tuning resolution, with coarse tuning speed and resolution of 0.5 THz/s and 20 MHz, respectively.

Once the optical signal is generated it can be used for a variety of applications, one of which is optical signals processing. Despite the great success and widespread use of electrical signal processing, there are issues such as the limited bandwidth and lossy interconnects that makes implementation of systems such as high data-rate links and true-time delay based antenna arrays challenging. In the optical regime, large available bandwidth as well as low propagation loss interconnects, enable systems with much better performance compared to the electrical counterparts. In the second work of this thesis, the first nanophotonic near-field microwave imager is presented that utilizes the advantages of optical signal processing to implement an imager that is smaller and lower power than the previous electrical ones. The target object is illuminated by a train of UWB microwave pulses and the reflected signals are received by a 2x2 array of UWB antennas. The received signals are amplified and connected to the on-chip ring modulators. The modulators up-convert the electrical signals into optical frequencies by modulating the light coupled into the photonic chip. The modulated signals are then processed by a network of photonic delay elements. The delay elements are more than an order of magnitude smaller and less loss than the state-of-the-art electrical ones. After optically processing the electrical signals, an 11x11 network of photodiodes convert the signals into electrical ones to form the corresponding image of the object. Full characterization of the chip is presented in chapter 3 of the thesis including wired and wireless single source characterization. Finally, using some metallic objects, near-field imaging is demonstrated using the implemented imager chip. The 121-element imager, which is integrated on a silicon chip, is capable of simultaneous processing of ultra-wideband microwave signals and achieves 4.8° spatial resolution for near-field imaging with orders of magnitude smaller size than the benchtop implementations and a fraction of the power consumption.

The last work is towards ultra-compact OPAs for 2-D optical beam steering with applications in optical communications, LiDAR, imaging and projection systems. Unlike microwave phase arrays in which because of the wavelength size, half-wavelength element spacing is achievable, in OPAs this s an open problem. The main obstacles are the large size of optical elements as well as the finite size of the required photonic routing devices. In chapter 4 of the thesis, a novel architecture is proposed that reduces the element spacing of an OPA in two steps. First, the conventional N^2 phase shifters that are used to control the relative phase between the elements is reduced by a factor of N/2, which significantly reduces the photonic and electrical routings as well as the power consumption of the OPA. An 8x8 OPA chip is implemented in IME 180 nm SOI process using the proposed architecture and 2-D beam steering is demonstrated via adjusting the relative phases using only 16 phase shifters. The chip achieves and steering range of 7°. The second step is to reduce the individual size of the elements and to eliminate the bulky photonic devices previously used for on-chip light distribution. A photonic process that offers two layers of silicon and silicon nitride for routing is used. Beam steering along the X and Y directions are achieved using two sets of NxN apertures in each routing layer. The optical signals of these layers are combined vertically since they are placed in the near-field of each other. This method combined with the reduction of the number of phase shifters, enable very compact element spacing within the OPA aperture. Another 8x8 chip is implemented in the TowerJazz 180 nm photonic process with element spacing of only 3 μm. 2-D steering of a single beam is demonstrated using this chip that achieves a steering range of about 23°.

5.2 Future research directions

For each of the three works presented in this thesis, there are possible continuations that have been introduced previously in their corresponding chapters. In this section, a summary of those is presented.

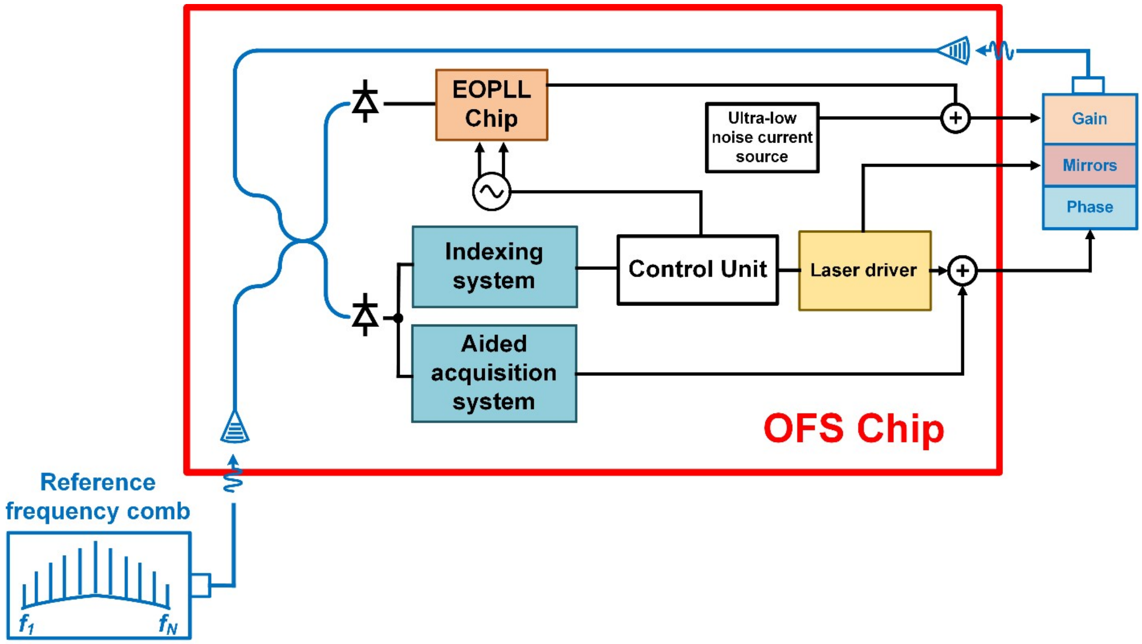

Figure 5.1 – The conceptual block diagram of a fully integrated OFS chip excluding the TL and the reference comb.

The partially integrated OFS was successfully used to demonstrate high-resolution synthesis, therefore, the immediate continuation would be integrating other blocks on the same chip. Figure 5.1 shows the conceptual block diagram of the proposed chip. The reference comb and the TL are coupled to the chip using grating couplers. Similar to the approach explained in chapter 2, the indexing systems is used for coarse tuning and the EOPLL for fine tuning of the TL. The AAS enhances the acquisition range and helps with addressing the false locking and temperature stabilization issues. The chip can be implemented in a standard CMOS SOI process. Therefore, the TL and the reference comb that require different materials for fabrication and are outside the scope of this thesis, could be integrated on a separate photonic chip and the complete OFS system will be a result of hybrid integration of the chips.

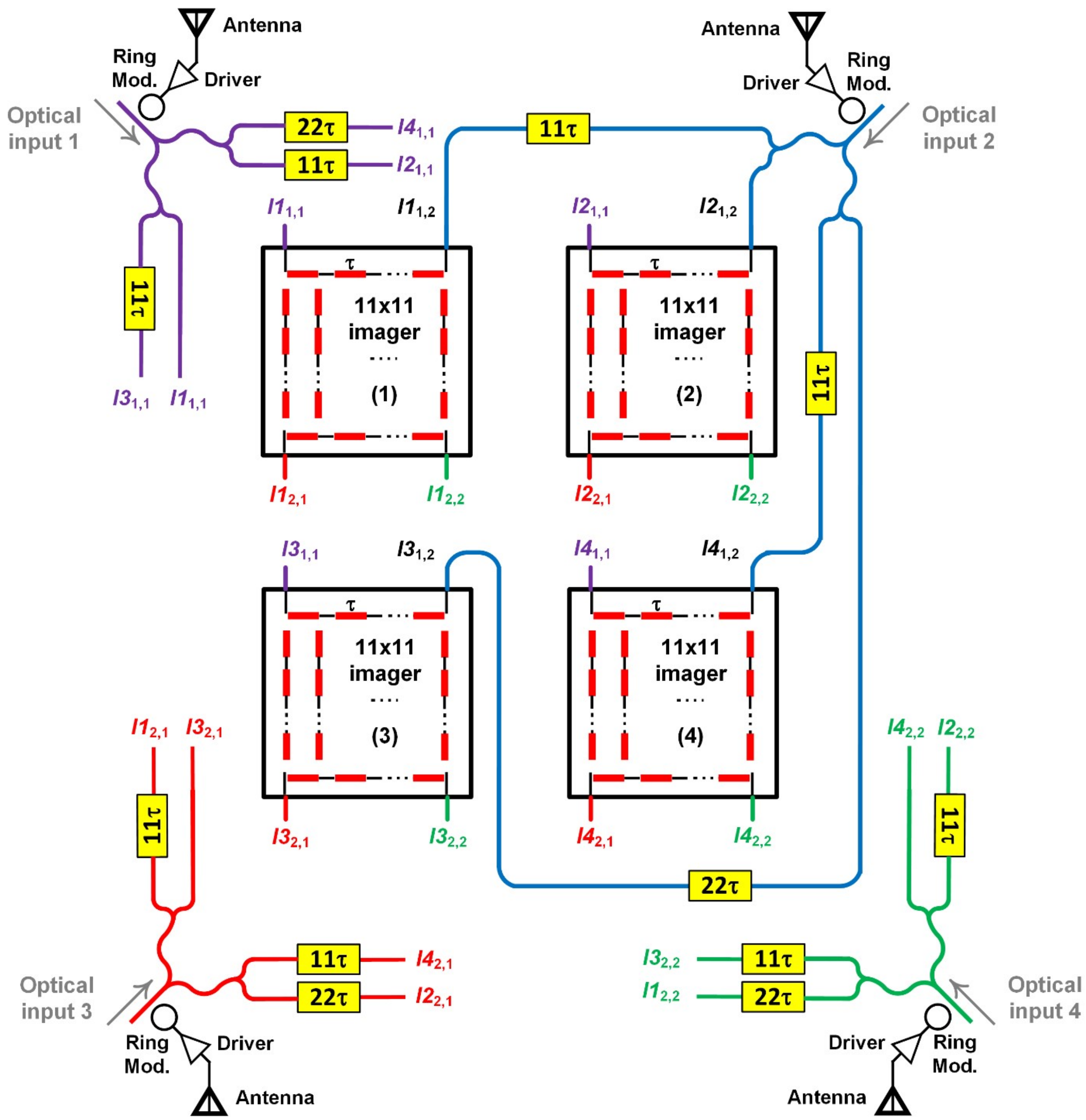

Figure 5.2 – Proposed method of scaling the number of pixel of the nanophotonic imager.

The nanophotonic imager can be used at higher microwave frequencies. Figure 3.3(d) shows that as frequency increases, the loss per electrical delay cell increases drastically, making implementation of and electrical systems even more challenging. This large loss necessitates using more repeating amplifiers on chip, which in turn increase the power consumption. Since the loss per photonic delay element in the proposed approach is almost constant versus frequency, the same architecture can easily be used at higher frequencies. The ring modulator and the photodiode both have bandwidths larger than 30 GHz that makes them capable of handling tens of GHz signals.

In addition, the number of pixels of the imager can be scaled up by tiling multiple imagers with less number of pixels. Again, since the loss per delay element is much smaller than the electrical counterparts, the power consumption penalty would be much less, too. Figure 5.2 shows the proposed scaling method. This figure shows how a 484-pixel imager can be constructed using four 121-pixel sections. It should be noted that the overall on-chip optical loss increases that can be compensated by increasing the laser power at the input, which would still be lower than the power penalty of the electrical solution.

Finally, the novel OPA architecture introduced in chapter 4 can be scaled in terms of the number elements. Benefiting from a two-layer photonic routing process as well as the reduced number of phase shifters required for beam steering, very compact aperture was achieved. To increase the number of elements, considering the challenge of optical signal distribution, one potential solution is shown in Fig 5.3. In this figure a 4096-element OPA (8x8) is shown in which the input light is first split into 128 signals, 64 rows and 64 columns. Each row/column signal goes through a phase shifter to properly adjust the phase. Then each should be split into another 64 signals that are routed to the elements.

The light distribution is a combination of the two methods explained in chapter 4. Each row/column consists of 7 directional couplers with varying lengths to equally distribute the light among the waveguide gratings. In each of the 8 waveguide grating sections, light is split into 8 signals that are coupler out of the chip by the gratings.

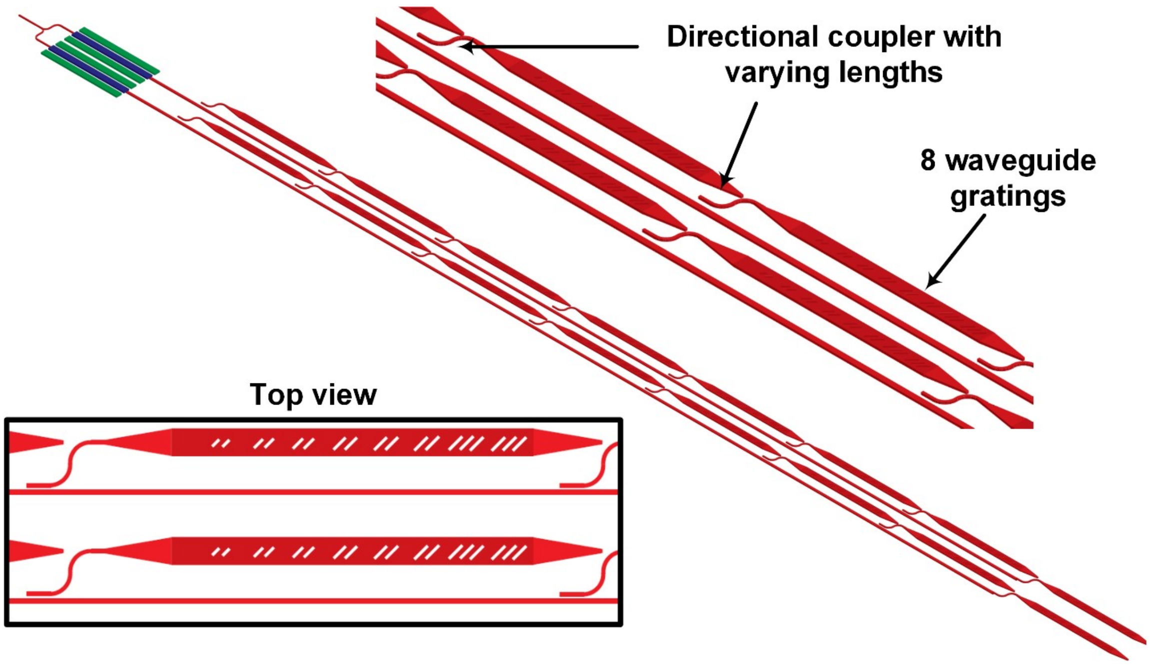

Figure 5.3 – Schematic of the proposed OPA row/column with 64 elements.

References

[1] M. Hochberg, and T. Baher-Jones, “Towards fabless silicon photonics”, *Nature Photonics* 4, 492-494 (2010).

[2] B. Jalali and S. Fathpour, "Silicon Photonics," *J. Lightwave Technol*. 24, 4600-4615 (2006).

[3] M. H. Idjadi and F. Aflatouni, "Integrated Pound-Drever-Hall laser stabilization system in silicon," *Nature Communications* 8, 1209 (2017).

[4] F. Aflatouni and H. Hashemi, "An electronically controlled optical phased array," in *IEEE International Microwave Symposium (IMS) Dig. Papers*, WEPN-6, (2012).

[5] F. Aflatouni, M. Bagheri, and H. Hashemi, "Design methodology and architectures to reduce the semiconductor laser phase noise using electrical feed-forward schemes," in *IEEE Transactions on Microwave Theory and Techniques*, 11, 3290-31683, November (2010).

[6] Z. Xuan, L. Du, and F. Aflatouni, "Frequency locking of semiconductor lasers to RF oscillators using hybrid-integrated opto-electronic oscillators with dispersive delay lines," Optics Express, 8, 10729-10737 (2019).

[7] W. Li and J. Yao, "Microwave and Terahertz Generation Based on Photonically Assisted Microwave Frequency Twelvetupling with Large Tunability," in *IEEE Photonics Journal*, 6, 954-959 (2010).

[8] B. J. Bortnik and H. R. Fetterman, "High-speed photonically assisted analog-to-digital conversion using a continuous wave multiwavelength source and phase modulation," *Optics Letters* 33, 2230-2232 (2008)

[9] H. Hashemi, T. S. Chu, and J. Roderick, "Integrated true-time-delay-based ultra-wideband array processing," *IEEE Commun. Mag.* 46, 162-172 (2008).

[10] P. Y. Deng, and J. F. Kiang, "A 5-GHz CMOS Frequency Synthesizer With an Injection-Locked Frequency Divider and Differential Switched Capacitors," in *IEEE Trans. Circuits Syst. I, Reg. Papers* 56, no. 2, pp. 320-326 (2009).

[11] X. Yi, C. C. Boon, H. Liu, J. F. Lin, and W. M. Lim, "A 57.9-to-68.3 GHz 24.6 mW Frequency Synthesizer With In-Phase Injection-Coupled QVCO in 65 nm CMOS Technology," in *IEEE J. Solid-State Circuits* 49, no. 2, pp. 347-359 (2014).

[12] P. Park, D. Park, and S. Cho, "A 2.4 GHz Fractional-N Frequency Synthesizer With High-OSR ΔΣ Modulator and Nested PLL," in *IEEE J. Solid-State Circuits* 47, no. 10, pp. 2433-2443(2012).

[13] Lionix ultra-narrow linewidth tunable laser, available at: https://photonics.lionix-international.com/narrowlinelaser/

[14] The PureSpectrum narrow linewidth laser, available at: https://www.teraxion.com/en/products/optical-sensing/narrow-linewidth-laser/

[15] Y. Yao, Y. Jiang, L. Wu, H. Yu, and Z. Bi, "A low noise optical frequency synthesizer at 700–990 nm," *Appl. Phys. Lett*. 109, 131102 (2016).

[16] Th. Udem, R. Holzwarth, and T. W. Hansch, "Optical frequency metrology," *Nature* 416, pp. 233-237 (2002).

[17] R. Holzwarth, Th. Udem, T. W. Hansch, J. C. Knight, W. J. Wadsworth, and P. St. J. Ruddell, "Optical frequency synthesizer for precision spectroscopy," *Phys. Rev. Lett.* 85, 2263 (2000).

[18] A. Yariv, “Dynamic analysis of the semiconductor laser as a current-controlled oscillator in the optical phased-locked loops: applications,” *Optics Letters* 30, 2191-2193 (2005).

[19] N. Satyan, A. Vasilyev, G. Rakuljic, J. O. White, and A. Yariv, “Phase-locking and coherent power combining of broadband linearly chirped optical waves,” *Opt. Express* 20, 25213-25227 (2012).

[20] A. G. Griffith, R. k. W. Lau, J. Cardenas, Y. Okawachi, A. Mohanty, R. Fain, Y. H. D. Lee, M. Yu, C. T. Phase, C. B. Poitras, A. L. Gaeta, and M. Lipson, “Silicon-chip mid-infrared frequency comb generation,” *Nat. Commun.* 6, 6299 (2015).

[21] Y. Okawachi, K. Saha, J. S. Levy, Y. Henry Wen, M. Lipson, and A. L. Gaeta, "Octave-spanning frequency comb generation in a silicon nitride chip," *Optics Letters* 36, 3398-3400 (2011).

[22] C. Vozzi, et al, "High-energy, few-optical-cycle pulses at 1.5 μm with passive carrier-envelope phase stabilization," Opt. Express 14, 10109-10116 (2006).

[23] V. Tsatourian, H. S. Margolis, G. Marra, D. T. Reid, and P. Gill, "Common-path self-referencing interferometer for carrier-envelope offset frequency stabilization with enhanced noise immunity," Opt. Lett. 35, 1209-1211 (2010).

[24] M. H. Idjadi, and F. Aflatouni, “Integrated Pound-Drever-Hall laser stabilization system in silicon”, *Nat. Commun.,* vol. 8, 1209 (2017).

[25] F. Aflatouni, B. Abiri, A. Rekhi, H. Abediasl, H. Hashemi and A. Hajimiri, "Electronic laser phase noise reduction," in *IEEE Radio Freq. Integr. Circuits Symp. (RFIC)*, Seattle, WA, pp. 265-268 (2013).

[26] H. Abediasl, and H. Hashemi, "Monolithic optical phased-array transceiver in a standard SOI CMOS process," *Opt. Express,* vol. 23, 6509-6519 (2015).

[27] F. Aflatouni, “Electronically assisted relative and absolute phase control of semiconductor lasers,” Ph.D. dissertation, Dept. Elect. Eng., Univ. Southern California, Los Angeles, CA, (2011).

[28] S. Ozharar, F. Quinlan, I. Ozdur, S. Gee and P. J. Delfyett, "Ultraflat Optical Comb Generation by Phase-Only Modulation of Continuous-Wave Light," *IEEE Photon. Technol. Lett.*, vol. 20, no. 1, pp. 36-38 (2008).

[29] F. Aflatouni, O. Momeni, and H. Hashemi, “A heterodyne phase locked loop with GHz acquisition range for coherent locking of semiconductor lasers in 0.13 μm CMOS,” in *IEEE Custom Integr. Circuits Conf. (CICC)*, pp. 463-466 (2007).

[30] R. Lang, and K. Kobayashi, "External optical feedback effects on semiconductor injection laser properties," in *IEEE J. of Quantum Electron.*, vol. 16, no. 3, pp. 347-355 (1980).

[31] S. Saito, O. Nilsson, and Y. Yamamoto, “Coherent FSK transmitter using a negative feedback stabilized semiconductor laser,” *Electron. Lett.*, 20 (17), 703-704 (1984).

[32] W. Liang, N. Satyan, F. Aflatouni, A. Yariv, A. Kewitsch, G. Rakuljic, and H. Hashemi, "Coherent beam combining with multilevel optical phase-locked loops," *J. Opt. Soc. Am. B* 24, 2930-2939 (2007).

[33] B. Argence, B. Chanteau, O. Lopez, and A, A. Klein, “Quantum cascade laser frequency stabilization at the sub-Hz level,” *Nature Photon*. 9, 456-460 (2015).

[34] S. Barbieri, P. Gellie, G. Santarelli, L. Ding, W. Maineult, C. Sirtori, R. Colombelli, H. Beere, and D. Ritchie, “Phase-locking of a 2.7-THz quantum cascade laser to a mode-locked erbium-doped fiber laser,” *Nature Photon*. 4, 636-640 (2010).

[35] L. Consolino, P. Gellie, G. Santarelli, L. Ding, W. Maineult, C. Sirtori, R. Colombelli, H. Beere, and D. Ritchie, “Phase-locking to a free-space terahertz comb for metrological-grade terahertz lasers,” *Nat. Commun*. 3, 1040 (2012).

[36] M. Lu, H. Park, E. Bloch, A. Sivananthan, A. Bhardwaj, Z. Griffith, L. A. Johansson, M. J. Rodwell, and L. A. Coldren, "Highly integrated optical heterodyne phase-locked loop with phase/frequency detection," *Opt. Express* 20, 9736-9741 (2012).

[37] M. Lu, H. C. Park, E. Bloch, L. A. Johansson, M. J. Rodwell, and L. A. Coldren, "A highly-integrated optical frequency synthesizer based on phase-locked loops," *Optical Fiber Communication Conference (OFC)*, pp. 1-3 (2014).

[38] A. Khachaturian, B. Abiri, A. Zhou, and A. Hajimiri, "Monolithic Mach-Zehnder Interferometer Modulator in an unmodified CMOS process," *IEEE Photonics Conference (IPC)*, pp. 394-395 (2015).

[39] C. Sun , M. T. Wade , Y. Lee , J. S. Orcutt , L. Alloatti , M. S. Georgas , A. S. Waterman , J. M. Shainline , R. R. Avizienis , S. Lin , B. R. Moss , R. Kumar , F. Pavanello , A. H. Atabaki , H. M. Cook , A. J. Ou , J. C. Leu , C. Yu-Hsin , K. Asanovic , R. J. Ram , M. Popovic , and V. M. Stojanovic, "Single-chip microprocessor that communicates directly using light," Nature 528, 534-538 (2015).

[40] F. M. Gardner, *Phaselock techniques* (John Wiley and Sons, 2005).

[41] R. M. Corless, G. H. Gonnet, D. E. G. Hare, D. J. Jeffrey, and D. E. Knuth, "On the Lambert W function," Advances in Computational Mathematics, 5(4):329-359, (1996).

[42] T. A. Burton. *Stability and Periodic Solutions of Ordinary and Functional Differential Equations*. (Academic Incorporation, 1985).

[43] F. Behbahani, Y. Kishigami, J. Leete, and A. A. Abidi, "CMOS mixers and polyphase filters for large image rejection," *IEEE Journal of Solid State Circuit*, 36 (6), 873-887 (2001).

[44] S. Arafin, and *et al*, "Towards chip-scale optical frequency synthesis based on optical heterodyne phase-locked loop," *Opt. Express*, vol. 25, no. 2, pp. 681-695, Jan 2017.

[45] K. Balakier, and *et al*, "Integrated Semiconductor Laser Optical Phase Lock Loops," *IEEE J. Sel. Topics in Quantum Electron.*, vol. 24, no. 1, pp. 1-12, Jan.-Feb. 2018.

[46] D. Marpaung, J. Yao, and J. Capmany, "Integrated microwave photonics," Nat. Photon. 13, 80-90 (2019).

[47] W. Zhang and J. Yao, "Silicon Photonic Integrated Optoelectronic Oscillator for Frequency-Tunable Microwave Generation," J. Lightwave Technol. 36, 4655-4663 (2018)

[48] V. C. Duarte, J. G. Prata, C. Ribeiro, R. N. Nogueira, G. Winzer, L. Zimmermann, R. Walker, S. Clements, M. Filipowicz, M. Napierała, T. Nasiłowski, J. Crabb, L. Stampoulidis, J. Anzalchi, and M. V. Drummond, "Integrated Photonic True-Time Delay Beamformer for a Ka-band Phased Array Antenna Receiver," in *Optical Fiber Communication Conference*, paper M2G.5 (2018).

[49] A. G. Yarovoy, T. G. Savelyev, P. J. Aubry, P. E. Lys, and L. P. Ligthart, "UWB array-based sensor for near-field imaging," *IEEE Trans. Microw. Theory Tech.* 55, 1288-1295 (2007).

[50] A. O. Boryssenko, C. Craeye, and D. H. Schaubert, "Ultra-wide band near-field imaging system," *IEEE Radar Conf.*, Boston, 402-407 (2007).

[51] S. Kidera, T. Sakamoto, and T. Sato, "High-resolution 3-D imaging algorithm with an envelope of modified spheres for UWB through-the-wall radars," *IEEE Tran. Antennas Propag.* 57, 3520-3529 (2009).

[52] X. Liang, J. Deng, H. Zhang, and T. A. Gulliver, "Ultra-wideband impulse radar through-wall detection of vital signs," Sci. Rep. 8, 13367 (2018).

[53] M. R. Mahfouz, C. Zhang, B. C. Merkl, M. J. Kuhn, and A. E. Fathy, "Investigation of high-Accuracy indoor 3-D positioning using UWB technology," *IEEE Trans. Microw. Theory Tech.* 56, 1316-1330 (2008).

[54] P. A. Catherwood and J. McLaughlin, "Internet of things-enabled hospital wards: ultra-wideband doctor-patient radio channels," *IEEE Antennas Propag. Mag.* 60, 10-18 (2018).

[55] H. Hashemi, T. S. Chu, and J. Roderick, "Integrated true-time-delay-based ultra-wideband array processing," *IEEE Commun. Mag.* 46, 162-172 (2008).

[56] H. Song, S. Sasada, T. Kadoya, M. Okada, K. Arihiro, X. Xiao, and T. Kikkawa, "Detectability of breast tumor by a hand-held impulse-radar detector: performance evaluation and pilot clinical study," Sci. Rep. 7, 16353 (2017).

[57] A. Rahman, M. T. Islam, M. J. Singh, S. Kibria, and Md. Akhtaruzzaman, "Electromagnetic performances analysis of an ultra-wideband and flexible material antenna in microwave breast imaging: to implement a wearable medical bra," Sci. Rep. 6, 38906 (2016).

[58] A. T. Mobashsher, A. Mahmoud, and A. M. Abbosh, "Portable weideband microwave imaging system for intracranial hemorrhage detection using improved back-projection algorithm with model of effective head permittivity," Sci. Rep. 6, 20459 (2016).

[59] Y. Lee, J. Y. Park, Y. W. Choi, H. K. Park, S. H. Cho, S. H. Cho, and Y. H. Lim, "A novel non-contact heart rate monitor using impulse-radio ultra-wideband (IR-UWB) radar technology," Sci. Rep. 8, 13053 (2018).

[60] 13. S. Brovoll, T. Berger, Y. Paichard, O. Aardal, T. S. Lande, and S. E. Hamran, "Time-lapse imaging of human heart motion with switched array UWB radar," *IEEE Trans. Biomed. Circuits Syst.* 8, 704-715 (2014).

[61] R. Chavez-Santiago and I. Balasingham, "Ultra-wideband signals in medicine," *IEEE Signal Process. Mag.* 31, 130-136 (2014).

[62] Liuqing Yang and G. B. Giannakis, "Ultra-wideband communications: an idea whose time has come," in *IEEE Signal Processing Magazine*, vol. 21, no. 6, pp. 26-54, (2004).

[63] T. S. Chu and H. Hashemi, "True-time-delay-based multi-beam arrays," *IEEE Trans. Microw. Theory Tech.* 61, 3072-3082 (2013).

[64] F. Elbahhar, A. Rivenq, M. Heddebaut, and J. M. Rouvaen, "Using UWB Gaussian pulses for inter-vehicle communications," *IEE P- Commun.* 152, 229-234 (2005).

[65] T. Kikkawa, P. K. Saha, N. Sasaki, and K. Kimoto, "Gaussian monocycle pulse transmitter using 0.18μm CMOS technology with on-chip integrated antennas for inter-chip UWB communication," *IEEE J. Solid-State Circuits*, 43, 1303-1312 (2008).

[66] T. Chu and H. Hashemi, "A CMOS UWB camera with 7×7 simultaneous active pixels," *IEEE International Solid-State Circuits Conf.* 120-600 (2008).

[67] S. Park and S. Jeon, "A 15–40 GHz CMOS true-time delay circuit for UWB multi-antenna systems," *IEEE Microw. Wireless Compon. Lett.* 23, 149-151 (2013).

[68] T. Chu, J. Roderick, and H. Hashemi, "An integrated ultra-wideband timed array receiver in 0.13 μm CMOS using a path-sharing true Time delay architecture," *IEEE J. Solid-State Circuits*, 42, 2834-2850 (2007).

[69] J. Roderick, H. Krishnaswamy, K. Newton, and H. Hashemi, “Silicon-based ultra-wideband beam-forming,” *IEEE J. Solid-State Circuits*, 41, 1726-1739 (2006).

[70] D. Colton and R. Kress, *Inverse Acoustic and Electromagnetic Scattering Theory* Ch. 2 (Springer, New York, 2013).

[71] B. Pile and G. Taylor, “Small-signal analysis of microring resonator modulators,” Opt. Express 22, 14913-14928 (2014).

[72] Z. Xuan, Y. Ma, Y. Liu, R. Ding, Y. Li, N. Ophir, A. E. Lim, G. Q. Lo, P. Magill, K. Bergman, T. B. Jones, and M. Hochberg, “Silicon microring modulator for 40 Gb/s NRZ-OOK metro networks in O-band,” Opt. Express 22, 28284-28291 (2014).

[73] Z. N. Low, J. H. Cheong, and C. L. Law, “Low-cost PCB antenna for UWB applications,” *IEEE Antennas Wireless Propag. Lett.* 4, 237-239 (2005).

[74] B. Razavi, *RF Microelectronics* (Prentice Hall, 2012).

[75] T. S. Chu, Silicon-based broadband short-range radar architectures and implementations, (Doctoral dissertation) pp. 29-30 (2010).

[76] A. Jain, N. Hosseinadeh, X. Wu, H. K. Tsang, R. Helkey, J. E. Bowers, and J. F. Buckwalter, A High Spur-Free Dynamic Range Silicon DC Kerr Ring Modulator for RF Applications, IEEE *J. Lightw. Technol.*, 37, 3261-3272 (2019).

[77] D. A. Balanis, *Antenna Theory, Analysis and Design* (John Wiley and Sons, 1997).

[78] A. Natarajan, A. Komijani, X. Guan, A. Babakhani and A. Hajimiri, "A 77-GHz Phased-Array Transceiver With On-Chip Antennas in Silicon: Transmitter and Local LO-Path Phase Shifting," in *IEEE Journal of Solid-State Circuits* 41, no. 12, pp. 2807-2819 (2006).

[79] C. T. Rodenbeck *et al*., "Ultra-wideband low-cost phased-array radars," in *IEEE Transactions on Microwave Theory and Techniques* 53, no. 12, pp. 3697-3703 (2005).

[80] S. Khang, D. Lee, I. Hwang, T. Yeo and J. Yu, "Microwave Power Transfer With Optimal Number of Rectenna Arrays for Midrange Applications," in *IEEE Antennas and Wireless Propagation Letters* 17, no. 1, pp. 155-159, (2018).

[81] S. J. Spector, B. F. Lane, M. R. Watts, L. D. Benney, J. G. Delva, A. E. Hare, A. F. Kelsey, J. M. Mlynarczyk, E. S. Hosseini, C. V. Poulton, and J. P. Laine, "Broadband Imaging and Wireless Communication with an Optical Phased Array," in *Conference on Lasers and Electro-Optics*, OSA Technical Digest (online) (Optical Society of America, 2018), paper SM3I.7

[82] W. Xie, T. Komljenovic, J. Huang, M. Tran, M. Davenport, A. Torres, P. Pintus, and J. Bowers, "Heterogeneous silicon photonics sensing for autonomous cars [Invited]," *Opt. Express* 27, 3642-3663 (2019).

[83] J. Sun, E. Timordugan, A. Yaacobi, E. Shah Hosseini, and M. R. Watts, "Large-scale nanophotonic phased array", *Nature* 493, 195-199 (2013).

[84] C. V. Poulton, *M. J. Byrd, P. Russo*, E. Timordugan, M. Khandaker, D. Vermeulen, and M. R. Watts, "Long-Range LiDAR and Free-Space Data Communication With High-Performance Optical Phased Arrays," in *IEEE Journal of Selected Topics in Quantum Electronics*, 25, 1-8 (2019).

[85] F. Aflatouni, B. Abiri, A. Rekhi, and A. Hajimiri, "Nanophotonic projection system," *Opt. Express* 23, 21012-21022 (2015).

[86] F. Aflatouni, B. Abiri, A. Rekhi, and A. Hajimiri, "Nanophotonic coherent imager," *Opt. Express* 23, 5117-5125 (2015).

[87] B. Abiri, F. Aflatouni, A. Rekhi, and A. Hajimiri, "Electronic Two-Dimensional Beam Steering for Integrated Optical Phased Arrays," in *Optical Fiber*

Communication Conference, OSA Technical Digest (online) (Optical Society of America, 2014), paper M2K.7.

[88] R. Fatemi, B. Abiri, and A. Hajimiri, "An 8×8 Heterodyne Lens-less OPA Camera," in *Conference on Lasers and Electro-Optics*, OSA Technical Digest (online) (Optical Society of America, 2017), paper JW2A.9.

[89] S. Chung, H. Abediasl, and H. Hashemi, "15.4 A 1024-element scalable optical phased array in 0.18µm SOI CMOS," *2017 IEEE International Solid-State Circuits Conference (ISSCC)*, San Francisco.

[90] C. V. Poulton, P. Russo, E. Timurdogan, M. Whitson, M. J. Byrd, E. Hosseini, B. Moss, Z. Su, D. Vermeulen, and M. R. Watts, "High-Performance Integrated Optical Phased Arrays for Chip-Scale Beam Steering and LiDAR," in *Conference on Lasers and Electro-Optics*, OSA Technical Digest (online) (Optical Society of America, 2018), paper ATu3R.2.

[91] K. Van Acoleyen, H. Rogier, and R. Baets, "Two-dimensional optical phased array antenna on silicon-on-insulator," *Opt. Express* 18, 13655-13660 (2010).

[92] J. K. Doylend, M. J. R. Heck, J. T. Bovington, J. D. Peters, L. A. Coldren, and J. E. Bowers, "Two-dimensional free-space beam steering with an optical phased array on silicon-on-insulator," *Opt. Express* 19, 21595-21604 (2011).

[93] D. N. Hutchison, J. Sun, J. K. Doylend, R. Kumar, J. Heck, W. Kim, C. T. Phare, A. Feshali, and H. Rong, "High-resolution aliasing-free optical beam steering," *Optica* 3, 887-890 (2016).

[94] J. C. Hulme, J. K. Doylend, M. J. R. Heck, J. D. Peters, M. L. Davenport, J. T. Bovington, L. A. Coldren, and J. E. Bowers, "Fully integrated hybrid silicon two dimensional beam scanner," *Opt. Express* 23, 5861-5874 (2015).

[95] T. Komljenovic, R. Helkey, L. Coldren, and J. Bowers "Sparse aperiodic arrays for optical beam forming and LIDAR," *Opt. Express* 25, 2511-2528 (2017).

[96] J. Goodman, *Introduction to Fourier Optics* (McGraw-Hill, 1996).

[97] A. Mekis, S. Gloeckner, G. Masini, A. Narasimha, T. Pinguet, S. Sahni, and P. D. Dobbelaere, "A Grating-Coupler-Enabled CMOS Photonics Platform," *IEEE Journal of Selected Topics in Quantum Electronics,* 17, 597-608 (2011).

[98] Y. Zhang, S. Yang, A. E. Lim, G. Q. Lo, C. Galland, T. Baeher-Jones, and M. Hochberg, "A compact and low loss Y-junction for submicron silicon waveguide," Opt. Express 21, 1310-1316 (2013).

[99] M. H. Lee, J. Y. Jo, D. W. Kim, Y. Kim, and K. H. Kim, "Comparative Study of Uniform and Nonuniform Grating Couplers for Optimized Fiber Coupling to Silicon Waveguides," *J. Opt. Soc. Korea* 20, 291-299 (2016).

[100] C. R. Doerr, L. Chen, Y. Chen and L. L. Buhl, "Wide Bandwidth Silicon Nitride Grating Coupler," in *IEEE Photonics Technology Letters*, vol. 22, no. 19, pp. 1461-1463, Oct.1, 2010.